DTIC FILE COPY

AD-A220 106

In Partial Fulfillment of the

Requirements for the Degree of

Master of Science in Electrical Engineering

Faron Britt Snodgrass, B.S., B.S.E.E.

DISTRIBUTION STATEMENT A

Approved for public release;
Distribution Unlimited

DTIC
ELECTE
APR 05 1990
S E D

DEPARTMENT OF THE AIR FORCE
AIR UNIVERSITY
AIR FORCE INSTITUTE OF TECHNOLOGY

Wright-Patterson Air Force Base, Ohio

90 04 05 127

AFIT/GE/ENG/90M-5

Accession For
NTIS GRA&I
DTIC TAB
Unannounced
Justification
By
Distribution/
Availability Codes
Dist | Avail and/or Special
A-1

Continued Development and Analysis of a New Extended Kalman Filter for the Completely Integrated Reference Instrumentation System (CIRIS)

THESIS

Presented to the Faculty of the School of Engineering

of the Air Force Institute of Technology

Air University

In Partial Fulfillment of the

Requirements for the Degree of

Master of Science in Electrical Engineering

Faron Britt Snodgrass, B.S., B.S.E.E.

Captain, USAF

March, 1990

Approved for public release; distribution unlimited

Preface

The thesis is the second in a series AFIT thesis research efforts to develop a new post–processing Kalman filter for the Completely Integrated Reference Instrumentation System (CIRIS). The ultimate goal is the "Advanced CIRIS Filter," designed around the current CIRIS II LN–39 INS, which processes both standard and differential mode Global Positioning System (GPS) measurements in addition to the current ground–based transponder measurements. The new Kalman filter is required to increase the position and velocity estimation accuracy of CIRIS so that CIRIS will remain a more accurate estimator relative to other types of navigation systems. This research is sponsored by the Central Inertial Guidance Test Facility (CIGTF), 6585th Test Group, Holloman AFB, New Mexico.

The new CIRIS Kalman filter developed in this and previous research is built upon the *Multimode Simulation for Optimal Filter Evaluation* (MSOFE) software developed by the Avionics Laboratory at Wright–Patterson AFB, Ohio. Although MSOFE was conceived and implemented as a simulation tool, its thoughtfully designed structure makes it readily adaptable for use with real measurements. It seems to be a consensus among the AFIT students who have used MSOFE that it is a difficult tool to master. I agree, but having become a journeyman MSOFE user myself, I see that the long learning curve is rooted in the difficult concepts of Kalman filter theory. MSOFE itself is very flexible and obviously well engineered. In an academic setting, MSOFE is exactly the type of tool needed in a "Kalman filter laboratory" to make the concept of a Kalman filter come to life. Hopefully, this thesis shows that MSOFE can also be put to good use outside of research laboratories and academic institutions.

At the onset of my particular research I had hoped to pick up at the point where my predecessor, Capt Joseph Solomon, had left off, and to concentrate on developing GPS error models and extending the filter structure to incorporate real GPS measurements. However, the idea of "serial" research, especially in a graduate–school setting, is often over–optimistic. I had to acquire and assimilate a great deal of totally new (to me) knowledge before I could comprehend what Capt Solomon had accomplished and what remained to be done. This need to "get up to speed," combined with the late availability of real GPS

data and my personal interest in the discipline of software engineering, led me to focus my efforts on small refinements to the error model on which the filter is based, an almost complete rewrite of the filter software, and additional analysis of the filter's performance using regular CIRIS (non-GPS) data sets. I hope that my forthcoming assignment to CIGTF will permit me to continue the development of the Advanced CIRIS Filter in parallel with follow-on research at AFIT.

I am indebted to several individuals for their assistance during my stay at AFIT. My thesis advisor, Lt Col Zdzislaw (Stan) Lewantowicz, guided me through this effort with much patience and good advice. If any individual can be said to have a natural aptitude for the mathematics of error model development, it is Col Lewantowicz. I was privileged to learn the theory of stochastic estimation from Dr. Peter Maybeck. Dr. Maybeck's ability as an instructor and the depth of his knowledge both exceed, in stochastics terminology, the $+3\sigma$ threshold. At the Avionics Lab, Mr. Stanton Musick, the prime force behind MSOFE, and his assistant, Mr. Robert Urbanic, provided exceptional assistance during the time I was learning to use MSOFE. At CIGTF, Mr. Gordon Simkin and Mr. Francisco Ramerez answered my many questions and provided me with CIRIS data. I also wish to thank Capt Joseph Solomon, Dr. Robert Ewing, and Mr. Don Smith. Last, because his name starts with a "Z," but first in my book, is Mr. Daniel Zambon, director of AFIT's Signal Information Processing Lab. Mr. Zambon is genuinely dedicated to providing reliable computer resources in support of student research efforts. He patiently assisted me on many occasions and for this I am extremely appreciative.

I also wish to acknowledge the lifelong support of my parents, Charles Edward Snodgrass and Shirley Ann Snodgrass. Their love and encouragement is priceless.

Faron Britt Snodgrass

Table of Contents

	Page
Preface	ii
Table of Contents	iv
List of Figures	vii
List of Tables	xi
Abstract	xii
I. Introduction	1-1
1.1 Background	1-2
1.2 Research Objectives	1-3
1.3 Research Approach	1-4
1.4 Thesis Overview	1-5
II. Theory	2-1
2.1 Reference Frames	2-1
2.2 Coordinate Transformations	2-4
2.3 Kalman Filter Theory	2-7
2.4 Time Correlated Errors and Residual Characteristics	2-10
2.5 Extended Kalman Filter and Error State Concepts	2-12
2.6 Simulation Software	2-15
2.7 Summary	2-16
III. 70-State Filter Description	3-1
3.1 Notation	3-1
3.2 Error State Vector	3-3

Page

3.2.1 INS Primary Error State Subvector 3-4

3.2.2 Baro–Altimeter Error State Subvector 3-8

3.2.3 Transponder Error State Subvector 3-8

3.3 Error State Stochastic Differential Equation 3-11

3.4 Measurement Models 3-11

3.4.1 Range Measurement 3-12

3.4.2 Range–Rate Measurement 3-14

3.4.3 Barometric Altitude Measurement 3-16

3.5 Summary 3-17

IV. 70–State Filter Evaluation: Ground Test Data 4-1

4.1 Data Collection Procedure 4-1

4.2 70–State Filter Performance 4-3

4.3 Summary 4-38

V. 70–State Filter Evaluation: Flight Test Data 5-1

5.1 Data Collection Procedure 5-1

5.2 70–State Filter Performance 5-1

5.3 CIRIS II Filter Performance 5-3

5.4 Summary 5-31

VI. Proposed Fixed–Interval Smoother 6-1

6.1 Fixed–Interval Smoothing 6-1

6.2 Application to the Advanced CIRIS Filter 6-3

6.3 Summary 6-5

VII. Conclusions and Recommendations 7-1

7.1 Conclusions 7-1

7.2 Recommendations 7-4

Page

7.2.1 Software Development 7-4

7.2.2 Data Problems 7-4

7.2.3 Future Research 7-6

A. Initial Covariance Values and Filter Matrix Definitions A-1

B. Recorded Data for Track Run E B-1

C. Recorded Trajectory Data, Yuma Flight C-1

Bibliography BIB-1

Vita VITA-1

List of Figures

Figure		Page
2.1.	WGS 84 Ellipsoidal Model	2-2
2.2.	Coordinate Frame Relationships	2-3
2.3.	Body to Navigation Frame Transformation	2-6
2.4.	First–Order Markov Characteristics	2-13
2.5.	Example of a "White" Residual Sequence	2-13
3.1.	LN–39 INS Vertical Channel Error Model	3-7
3.2.	Relative Positions of Transponder, Antenna, and INS	3-10
4.1.	Equipment Configuration for the CIRIS/RSV Tests	4-2
4.2.	Transponder Locations Relative to the Test Track	4-4
4.3.	Anomalous Range Measurement Oscillation, Transponder 211	4-5
4.4.	Oscillating Range Measurement Residuals, Transponder 211	4-6
4.5.	Latitude Difference, Track Run E	4-11
4.6.	Longitude Difference, Track Run E	4-12
4.7.	Altitude Difference, Track Run E	4-13
4.8.	North Velocity Difference, Track Run E	4-14
4.9.	West Velocity Difference, Track Run E	4-15
4.10.	Vertical Velocity Difference, Track Run E	4-16
4.11.	Baro–Altitude Residuals, Track Run E	4-17
4.12.	Transponder 005 Range Residuals, Track Run E	4-18
4.13.	Transponder 005 Range–Rate Residuals, Track Run E	4-19
4.14.	Transponder 102 Range Residuals, Track Run E	4-20
4.15.	Transponder 102 Range–Rate Residuals, Track Run E	4-21
4.16.	Transponder 181 Range Residuals, Track Run E	4-22

Figure Page

4.17. Transponder 181 Range–Rate Residuals, Track Run E 4-23

4.18. Transponder 212 Range Residuals, Track Run E 4-24

4.19. Transponder 212 Range–Rate Residuals, Track Run E 4-25

4.20. Transponder 216 Range Residuals, Track Run E 4-26

4.21. Transponder 216 Range–Rate Residuals, Track Run E 4-27

4.22. Estimated Position Error, Trans 005, Track Run E 4-28

4.23. Estimated Position Std Dev, Trans 005, Track Run E 4-29

4.24. Estimated Position Error, Trans 102, Track Run E 4-30

4.25. Estimated Position Std Dev, Trans 102, Track Run E 4-31

4.26. Estimated Position Error, Trans 181, Track Run E 4-32

4.27. Estimated Position Std Dev, Trans 181, Track Run E 4-33

4.28. Estimated Position Error, Trans 212, Track Run E 4-34

4.29. Estimated Position Std Dev, Trans 212, Track Run E 4-35

4.30. Estimated Position Error, Trans 216, Track Run E 4-36

4.31. Estimated Position Std Dev, Trans 216, Track Run E 4-37

5.1. C–141 Aircraft Trajectory over Yuma Test Range 5-5

5.2. Latitude Difference, Yuma Flight, Adv. CIRIS 5-6

5.3. Longitude Difference, Yuma Flight, Adv. CIRIS 5-7

5.4. Altitude Difference, Yuma Flight, Adv. CIRIS 5-8

5.5. North Velocity Difference, Yuma Flight, Adv. CIRIS 5-9

5.6. West Velocity Difference, Yuma Flight, Adv. CIRIS 5-10

5.7. Up Velocity Difference, Yuma Flight, Adv. CIRIS 5-11

5.8. Baro–Altitude Meas. Residuals, Yuma Flight, Adv. CIRIS 5-12

5.9. Trans. 160 Range Meas. Residuals, Yuma Flight, Adv. CIRIS 5-13

5.10. Trans. 163 Range Meas. Residuals, Yuma Flight, Adv. CIRIS 5-14

5.11. Trans. 226 Range Meas. Residuals, Yuma Flight, Adv. CIRIS 5-15

5.12. Trans. 160 Range–Rate Meas. Residuals, Yuma Flight, Adv. CIRIS . . 5-16

Figure | Page

5.13. Trans. 163 Range–Rate Meas. Residuals, Yuma Flight, Adv. CIRIS . . 5-17

5.14. Trans. 226 Range–Rate Meas. Residuals, Yuma Flight, Adv. CIRIS . . 5-18

5.15. Latitude Difference, Yuma Flight, CIRIS II 5-19

5.16. Longitude Difference, Yuma Flight, CIRIS II 5-20

5.17. Altitude Difference, Yuma Flight, CIRIS II 5-21

5.18. North Velocity Difference, Yuma Flight, CIRIS II 5-22

5.19. West Velocity Difference, Yuma Flight, CIRIS II 5-23

5.20. Up Velocity Difference, Yuma Flight, CIRIS II 5-24

5.21. Transponder 160 Range Measurement Residuals, CIRIS II 5-25

5.22. Transponder 163 Range Measurement Residuals, CIRIS II 5-26

5.23. Transponder 226 Range Meas. Residuals, CIRIS II 5-27

5.24. Transponder 160 Range–Rate Meas. Residuals, CIRIS II 5-28

5.25. Transponder 163 Range–Rate Meas. Residuals, CIRIS II 5-29

5.26. Transponder 226 Range–Rate Meas. Residuals, CIRIS II 5-30

B.1. TDAS Position, Track Run E B-2

B.2. TDAS Velocity, Track Run E B-3

B.3. INS Indicated Position, Track Run E B-4

B.4. INS Indicated Velocity, Track Run E B-5

B.5. INS Indicated Acceleration and Wander Angle, Track Run E B-6

B.6. Baro–altimeter Altitude and Altitude Rate, Track Run E B-7

B.7. Transponder 005 Range and Range–Rate, Track Run E B-8

B.8. Transponder 102 Range and Range–Rate, Track Run E B-9

B.9. Transponder 181 Range and Range–Rate, Track Run E B-10

B.10. Transponder 211 Range and Range–Rate, Track Run E B-11

B.11. Transponder 212 Range and Range–Rate, Track Run E B-12

B.12. Transponder 216 Range and Range–Rate, Track Run E B-13

C.1. Laser Ranging System Indicated Position, Yuma Flight C-2

Figure | Page

C.2. Laser Ranging System Indicated Velocity, Yuma Flight C-3

C.3. LN–39 INS Indicated Position, Yuma Flight C-4

C.4. LN–39 INS Indicated Velocity, Yuma Flight C-5

C.5. INS Indicated Acceleration and Wander Angle, Yuma Flight C-6

C.6. LN–39 INS Indicated Aircraft Attitude, Yuma Flight C-7

List of Tables

Table	Page
2.1. WGS 84 Parameters	2-2
4.1. INS Position Offsets	4-2
4.2. Transponder Locations for the CIRIS/RSV Tests	4-3
A.1. Non–Zero Elements of $\mathbf{P}_0$	A-2
A.2. Non–Zero Elements of $\mathbf{P}_0$, Continued	A-3
A.3. Non–Zero Elements of $\mathbf{P}_0$, Continued	A-4
A.4. Non–Zero Elements of $\mathbf{P}_0$, Continued	A-5
A.5. Non–Zero Elements of $\mathbf{P}_0$, Continued	A-6
A.6. Non–Zero Elements of $\mathbf{P}_0$, Continued	A-7
A.7. Non–Zero Elements of $\mathbf{F}$	A-8
A.8. Non–Zero Elements of $\mathbf{F}$, Continued	A-9
A.9. Non–Zero Elements of $\mathbf{F}$, Continued	A-10
A.10. Non–Zero Elements of $\mathbf{Q}$	A-11
A.11. Non–Zero Elements of $\mathbf{H}_r$	A-12
A.12. Non–Zero Elements of $\mathbf{H}_{\dot{r}}$	A-13
A.13. Non–Zero Elements of $\mathbf{H}_{h_b}$	A-14
A.14. Non–Zero Elements of $\mathbf{R}$	A-15

AFIT/GE/ENG/90M-5

Abstract

The Completely Integrated Reference Instrumentation System (CIRIS) is operated by the Central Inertial Guidance Test Facility (CIGTF), at Holloman AFB, New Mexico. CIRIS functions as a reference navigation system used for evaluating the accuracy of other types of navigations systems. As a reference standard, the root-mean-square errors in CIRIS estimates of aircraft trajectory variables must be maintained an order of magnitude smaller than the corresponding errors of the navigation system under test. The primary hardware components of CIRIS are a reference inertial navigation system (INS), a baro-altimeter, an array of ground-based transponders, a transponder interrogator, and data recording equipment. The transponder equipment provides transponder-to-aircraft range and range-rate measurements during test flights. The primary software component of CIRIS is a Kalman filter program which processes the recorded measurements and estimates the true position and velocity of the aircraft throughout the test flight.

The estimation accuracy of CIRIS must be increased so that CIRIS can serve as a benchmark for measuring the accuracy of Global Positioning System (GPS) aided inertial navigation systems. This thesis documents the continuation of research to develop completely new Kalman filter software for CIRIS. A 70-state filter, based on the Multimode Simulation for Optimal Filter Evaluation (MSOFE) program, developed in previous research is the starting point. This 70-state filter models error dynamics associated with the CIRIS Litton LN-39 INS, baro-altimeter, and transponder equipment. In this thesis, the model for atmospheric effects on transponder range measurements is refined and the filter is modified to process barometric altitude measurements in addition to the transponder measurements. The performance of the resulting filter is evaluated using real CIRIS data recorded during a slow speed ground test and an aircraft flight test. The filter position and velocity estimates are compared to independent measurements of the same quantities. The structure for a companion fixed-interval smoother program is proposed and discussed, but not implemented. Future research is expected to extend the filter to process differential mode GPS measurements.

Continued Development and Analysis of a New Extended Kalman Filter for the Completely Integrated Reference Instrumentation System (CIRIS)

I. Introduction

This thesis describes the continuing development and analysis of an extended Kalman filter for the Advanced Completely Integrated Reference Instrumentation System (CIRIS). The major goals of this thesis effort are filter software development, filter model validation via performance evaluation, and description of a "smoothing" algorithm that makes maximum use of the filter calculations.

CIRIS is a system for evaluating the accuracy of aided or unaided inertial navigation systems (INS). It is operated by the Central Inertial Guidance Test Facility (CIGTF), 6585th Test Group, Air Force Systems Command, Holloman AFB, New Mexico. Its primary hardware components are a Litton LN–39 INS, an array of ground based transponders, and a transponder interrogator [2,11]. The transponders are located at precisely surveyed points throughout the continental United States. For a CIRIS test flight, the INS being evaluated (test article) is placed in an aircraft alongside the LN–39 INS and the transponder interrogator. During the flight of the aircraft, the interrogator requests and receives range and velocity information from selected transponders. The transponders are interrogated one at a time. Typically, a "window" containing eight or fewer transponders is selected and the interrogator repeatedly cycles through only these transponders. The specific transponders contained in the window may change during the flight. The range, velocity, baro–altimeter, and LN–39 INS information is currently processed by an extended Kalman filter algorithm running, in real–time, on a digital computer. The Kalman filter provides accurate estimates of the aircraft position, velocity, and attitude throughout the aircraft flight. This information is used as a reference against which the position, velocity, and attitude calculations of the test article are compared.

1.1 Background

The original CIRIS system was developed by CIGTF in the early 1970's and became operational in 1975 [4]. It uses a Litton LN–15 INS which is no longer routinely supported by Air Force maintenance depots. This original system, called CIRIS I, is still in use. A newer version of CIRIS, based on the LN–39 INS, is called CIRIS II. Both versions of CIRIS are based on a 14–state extended Kalman filter of which only 11 states are actually used. States 1–9 are the primary INS position, velocity, and attitude error states. States 10 and 11 model errors in the baro-altimeter aiding of the vertical channel. States 12–14 were originally intended to model errors in Doppler velocity aiding but are not used because initial tests indicated the Doppler aiding did not provide a significant increase in accuracy. All subsequent references to CIRIS refer to CIRIS II. The term "Advanced CIRIS" is used here to refer to the high–order (50 or more states) post–processing filters developed in this, previous, and subsequent AFIT thesis research.

The 11–state CIRIS Kalman filter runs on a Hewlett–Packard HP 1000 computer carried aboard the aircraft. The position and velocity estimates are recomputed every second. The current CIRIS I system provides latitude and longitude accurate to 13 feet (ft) 1σ, altitude accurate to 40 ft 1σ, north and west velocity accurate to 0.1 feet/second (fps) 1σ, and vertical velocity accurate to 0.4 fps 1σ [4]. The 1σ standard deviation value is for a Gaussian (normal) error distribution.

Currently, the position and velocity estimates provided by CIRIS are more accurate than those from almost any other type of navigation system. Thus CIRIS is a reference standard for evaluating the accuracies of navigation systems. However, more accurate navigation systems are becoming available due to increased manufacturing precision, new sensor technologies, more powerful navigation computers, and satellite based navigation systems. Since it is essential that the reference navigation system be at least an order of magnitude more accurate the navigation systems being evaluated, the accuracy of CIRIS must be increased.

A powerful characteristic of a properly designed Kalman filter is the ability to process measurements of some quantity from two or more independent sources and produce an

estimate of that quantity that is more accurate than the individual measurements. This characteristic depends on the accuracy of the mathematical models of the physical system as the basis for proper Kalman filter design.

Three ways of increasing CIRIS accuracy are apparent. The first approach is to expand the number of states in the CIRIS Kalman filter to model additional time–correlated error sources in the existing LN–39 INS and transponder measurement equipment. This is the approach taken by Captain Joseph Solomon in his AFIT thesis research [13]. A second, complementary approach is to reprocess the filter estimates with a type of backward running optimal estimator known as a *smoother*. The third approach is to aid CIRIS with Global Position System (GPS) measurements. The continuation of the first approach and the initial investigation of the second approach are the primary goals of this thesis research. The third approach will be the subject of future AFIT thesis research.

1.2 Research Objectives

There are three main research objectives. The first is to improve the filter software developed by Solomon. This includes improving the source code structure and efficiency, making the filter easier to use, and adding features and capabilities.

The second objective is to evaluate, using real CIRIS data, the performance of a refined version of the 70–state filter developed by Solomon. This includes limited tuning of selected filter parameters to improve performance.

The third objective is the development of a fixed–interval *smoothing* algorithm. This type of smoother is an optimal estimator that processes previously filtered information backwards in time. This requires that certain data from the forward pass be recorded for subsequent use by the smoother. The smoothing algorithm starts with the most recent data and proceeds backward to the beginning of the interval. This characteristic prevents the use of the smoother in real–time; it must be used as a data post–processor. Since the CIGTF mission does not normally require real–time data processing, the operation of the advanced CIRIS filter and the smoother as post–processors will enhance the quality of the reference trajectory.

1.3 Research Approach

The performance of the revised 70–state filter algorithm is determined, and the error model validated, using data from a series of tests conducted at the 6585th Test Group's rocket sled test track. An instrument rack containing the CIRIS LN–39 INS and transponder interrogator was installed in a Recovery Support Vehicle (RSV). The RSV was towed along the track at speeds of 40–60 *fps* while the CIRIS data was recorded. At the same time, the RSV's position along the track was recorded by the independent track data acquisition system. Both sets of data were time–tagged using an Inter–Range Instrumentation Group (IRIG) time standard common to both data acquisition systems. The relatively slow speeds are chosen to make the data collection time interval reasonably large. Since the starting location is known precisely and the relative locations of the track position sensors are known within a millimeter [7], the track measurements are an accurate standard by which the advanced CIRIS filter performance can be evaluated. Filter model validation is achieved by analysis of measurement residual characteristics and by comparison of the filter's position and velocity estimates to those derived from the track measurements.

The accuracy of the 70–state filter estimates is also evaluated using CIRIS data from an actual aircraft flight. The reference standard for this test is the measurements of aircraft position and velocity provided by the laser tracking system at the Yuma, Arizona, test range. The average accuracy of these laser measurements is roughly twice that of CIRIS [7].The CIRIS II filter estimates are also compared to the laser measurements so that accuracy of Advanced CIRIS relative to CIRIS II may be evaluated.

The smoothing algorithm suggested by this thesis research is a discrete–time inverse covariance formulation. The algorithm was originally developed by Meditch [10] and further described by Maybeck [9]. The method makes use of the forward pass calculations of the covariance matrix and the state dynamics matrix for the backward pass calculation of a smoother gain matrix. The forward pass time–history for the dynamics matrix, the covariance matrix, and the state vector must be stored for later use during the smoothing procedure.

1.4 *Thesis Overview*

Chapter II describes the fundamental concepts used in this research. This includes coordinate frame definitions and transformations, basic Kalman filter theory, shaping filters for time–correlated noises, and measurement residual characteristics. The computer software packages used to support this research are described here.

Chapter III provides a description of the error states and structure of the 70–state model on which the Advanced CIRIS filter is based. The method of compensating for "lever arm" effects is presented in detail.

Chapter IV describes the test procedures and 70–state filter performance for CIRIS data collected during the test track runs. The existence of an anomalous periodic variation in some of the transponder range measurement data is documented here.

Chapter V describes the 70–state filter performance for CIRIS data collected during a long aircraft flight over the Yuma test range. The Advanced CIRIS filter output is compared to position and velocity measurements from the laser tracking equipment. The accuracy of Advanced CIRIS relative to CIRIS II is discussed here.

Chapter VI describes the algorithm for the proposed fixer–interval smoother program and evaluates its practicality for use with the MSOFE–based Advanced CIRIS filter. The proposed smoothing algorithm is an adaptation of a procedure originally designed for use with filters based on discrete–time dynamics models.

Chapter VII summarizes the final results of this research. Conclusions based on these results and recommendations for future research in this area are described here.

II. Theory

This chapter describes the fundamental concepts and theory on which this research is based. Because of the commonality between this research and that of Solomon, significant portions of this chapter are paraphrased from Solomon's thesis [13].

2.1 Reference Frames

In terrestial navigation applications, position is usually specified in terms of a spherical coordinate system of geodetic latitude, longitude, and altitude. Velocity is usually specified in terms of a rectangular coordinate system based on two compass directions and a vertical direction such as north, west, and up. It is often necessary to relate such geographically descriptive coordinates to an earth-centered, earth-fixed (ECEF) rectangular coordinate system, (E-frame). Several *geodetic systems* have been developed, but the most accurate is the World Geodetic System 1984 (WGS 84). This system is provided to the Department of Defense (DOD) by the Defense Mapping Agency (DMA). In the WGS 84 system, the earth is modeled as an oblate ellipsoid as illustrated in Figure 2.1. The parameters shown in Figure 2.1, the ellipse eccentricity e, and the ellipse flattening constant (ellipticity) f are defined in Table 2.1 [3]. The X_e axis is parallel to the meridian plane which includes the Bureau International de L'Heure (BIH). This is the Zero Meridian (Greenwich Meridian). The Y_e axis is rotated 90 degrees to the east along the equatorial plane. The Z_e axis is colinear with the earth's spin axis and completes the right-handed, earth-fixed, orthogonal coordinate system. The nonlinear equations [15] relating these rectangular coordinates to the geodetic latitude (L), longitude (λ), and altitude (h) are

$$R_n = \frac{A}{\sqrt{1 - e^2 \sin^2 L}} \tag{2.1}$$

$$X_e = (R_n + h) \cos L \cos \lambda \tag{2.2}$$

$$Y_e = (R_n + h) \cos L \sin \lambda \tag{2.3}$$

$$Z_e = (R_n(1 - e^2) + h) \sin L \tag{2.4}$$

where R_n is the *radius of curvature* in the prime vertical.

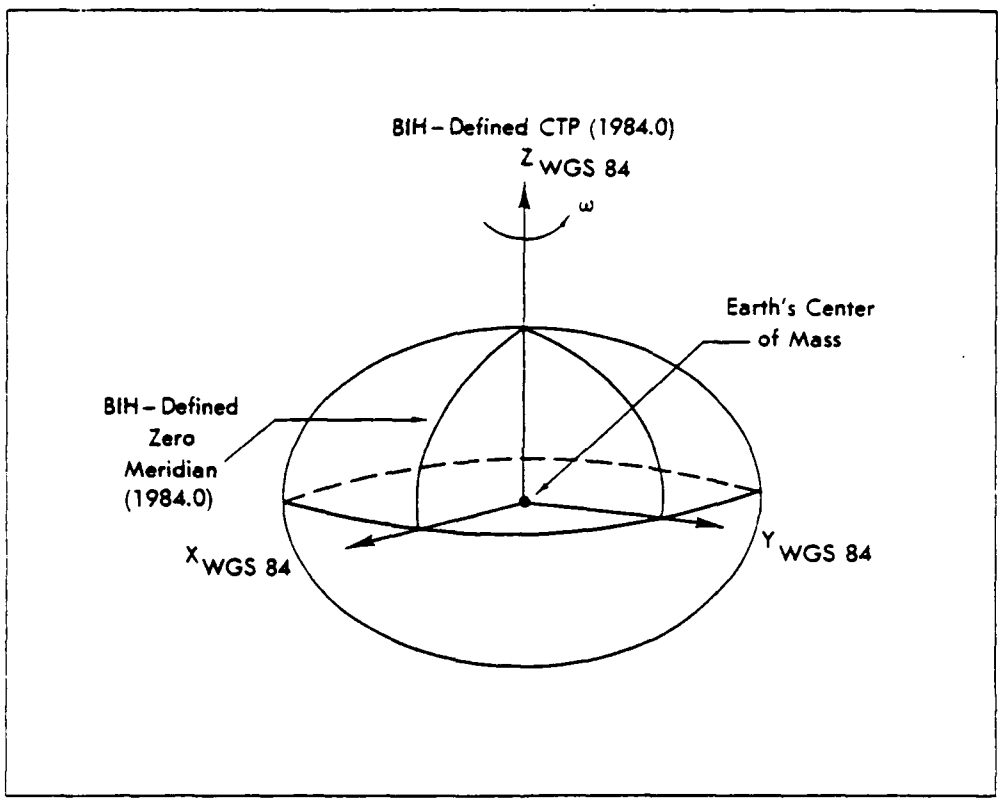

Figure 2.1. WGS 84 Ellipsoidal Model

Table 2.1. WGS 84 Parameters

Parameter	Definition	Value
X_e, Y_e, Z_e	ECEF Coordinate Frame Axes	not applicable
ω_{ie}	Angular Rate of the Earth	$7.292115 \cdot 10^{-5}\ s^{-1}$
A	Semimajor Axis (Equatorial Radius)	6378137 m
B	Semiminor Axis (Polar Radius)	6356752.3142 m
e	First Eccentricity	0.0818191908426
f	Flattening (Ellipticity)	0.00335281066474
g_0	Equatorial Acceleration of Gravity	9.7803267714 m/s^2 (32.087686258 ft/s^2)

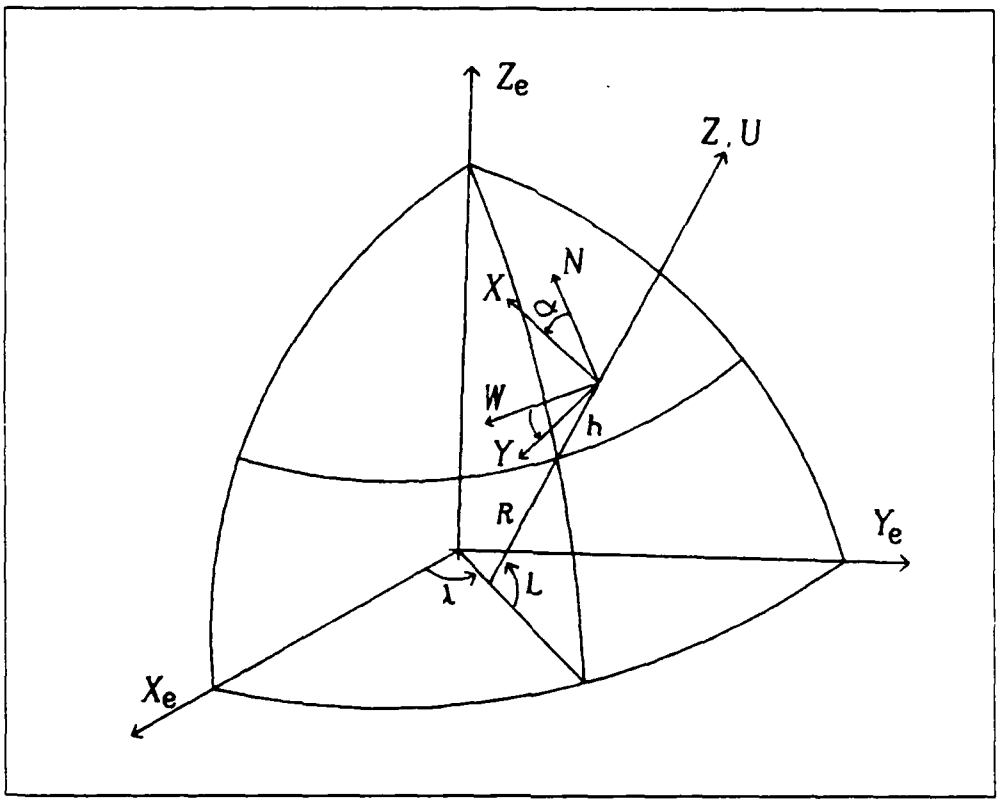

Figure 2.2. Coordinate Frame Relationships

The LN–39 INS implements a wander–azimuth, local–level platform mechanization [14]. The *true* platform frame (T–frame) is illustrated in Figure 2.2. The right–handed, orthogonal set of axes pointing north, west, and up are designated N, W, and U respectively. This frame is defined as the NWU navigation frame (N–frame). The right–handed, orthogonal T–frame axes are designated X, Y, and Z respectively; this is also referred to as the wander–azimuth frame. The wander angle *alpha* (α) is the angle between the X and N axes and between the Y and W axes created by a counter–clockwise (positive) rotation about the Z,U axis, of the T–frame with respect to the N–frame. When the wander angle is zero, the T–frame axes are parallel with the corresponding N–frame axes. In Figure 2.2, geodetic latitude, longitude, and altitude above the WGS 84 reference ellipsoid are designated by the variables L, λ, and h, respectively. These three parameters define the vehicle position in the navigation frame.

Another useful coordinate frame is the aircraft body (B–frame). This is reference frame that is "attached" to the body of the aircraft so that the orientation of the B–frame

with respect to the rigid aircraft body is constant. The origin of the B–frame is usually taken to be the center of the inertial measurement unit (IMU), a subsystem on the INS. In this thesis, the orientation of the B–frame axes is defined so that the B–frame is parallel to the NWU navigation frame when the aircraft nose is pointed north with wings level. The body frame X_b axis points out the nose of the aircraft, the Y_b axis points out the left wing, and the Z_b axis points up. This is not the usual convention for a body frame but it is more convenient in this application. The orientation of the B–frame with respect to the N–frame is defined by the three Euler angles: heading, pitch, and roll. A positive heading angle ψ is created by clockwise rotation of the body about the Z_b axis, a positive pitch angle θ is created by clockwise rotation of the body about the Y_b axis, and a positive roll angle ϕ is created by a clockwise rotation of the body about the X_b axis.

2.2 *Coordinate Transformations*

This section defines the coordinate transformation matrices needed for relating one reference frame to another. In addition to the E, N, and T frames, the LN–39 Systems Engineering Analysis Report [14] defines a platform frame (P–frame) and a computation frame (C–frame). The true frame, platform frame, and computation frame refer to the same general coordinate frame. However the platform and computation frames are slightly misaligned, by error angles, with respect to the true frame and with respect to each other. The platform frame is the wander–azimuth orthogonal frame "attached" to the INS platform such that P–frame coincides with the T–frame only when the platform is truly locally level. The computation frame is the wander–azimuth orthogonal frame that is locally level *at the latitude and longitude indicated by the INS computer.* Thus the C–frame coincides with the T–frame only if the INS indicated position is free of error. The transformations from the true frame to the platform and computation frames are defined [14] as

$$
\begin{aligned}
[\mathbf{X}]^P &= [\mathbf{I} + \boldsymbol{\phi}]\,[\mathbf{X}]^T \qquad (2.5)\\
\boldsymbol{\phi} &= \begin{bmatrix} 0 & \phi_Z & -\phi_Y \\ -\phi_Z & 0 & \phi_X \\ \phi_Y & -\phi_X & 0 \end{bmatrix}
\end{aligned}
$$

$$
\begin{aligned}
[\mathbf{X}]^C &= [\mathbf{I} + \delta\Theta]\,[\mathbf{X}]^T \qquad (2.6)\\
\delta\Theta &= \begin{bmatrix} 0 & \delta\Theta_Z & -\delta\Theta_Y \\ -\delta\Theta_Z & 0 & \delta\Theta_X \\ \delta\Theta_Y & -\delta\Theta_X & 0 \end{bmatrix}
\end{aligned}
$$

The $\delta\Theta$ and ϕvariables are skew-symmetric matrices representing small misalignment angles. This concept is used by Litton in the derivation of the INS error equations. The coordinate transformation matrices for the E, N, and P frames are now defined

$$
[\mathbf{X}]^N = C_P^N\,[\mathbf{X}]^P \qquad (2.7)
$$

$$
C_P^N = \begin{bmatrix} \cos\alpha & -\sin\alpha & 0 \\ \sin\alpha & \cos\alpha & 0 \\ 0 & 0 & 1 \end{bmatrix} \qquad (2.8)
$$

$$
[\mathbf{X}]^E = C_N^E\,[\mathbf{X}]^N \qquad (2.9)
$$

$$
C_N^E = \begin{bmatrix} -\sin L\cos\lambda & \sin\lambda & \cos L\cos\lambda \\ -\sin L\sin\lambda & -\cos\lambda & \cos L\sin\lambda \\ \cos L & 0 & \sin L \end{bmatrix} \qquad (2.10)
$$

$$
\begin{aligned}
C_P^E &= C_N^E C_P^N \qquad (2.11)\\
&= \begin{bmatrix} -\sin L\cos\lambda\cos\alpha + \sin\lambda\sin\alpha & \sin L\cos\lambda\sin\alpha + \sin\lambda\cos\alpha & \cos L\cos\lambda \\ -\sin L\sin\lambda\cos\alpha - \cos\lambda\sin\alpha & \sin L\sin\lambda\sin\alpha - \cos\lambda\cos\alpha & \cos L\sin\lambda \\ \cos L\cos\alpha & -\cos L\sin\alpha & \sin L \end{bmatrix}
\end{aligned}
$$

One more coordinate transformation matrix, C_B^N, is required to project vectors coordinatized in the B-frame onto the N-frame. That is

$$
[X]^N = C_B^N\,[X]^B \qquad (2.12)
$$

Because of the relative complexity of C_B^N, it is developed here in some detail. Consider an aircraft initially pointed north with wings level. The B-frame is then aligned with the N-frame. Any arbitrary orientation of the B-frame relative to the N-frame may be described by an ordered set of rotations about the B-frame axes. The B-frame is first rotated about Z_b by the heading angle ψ. This intermediate orientation of the B-frame

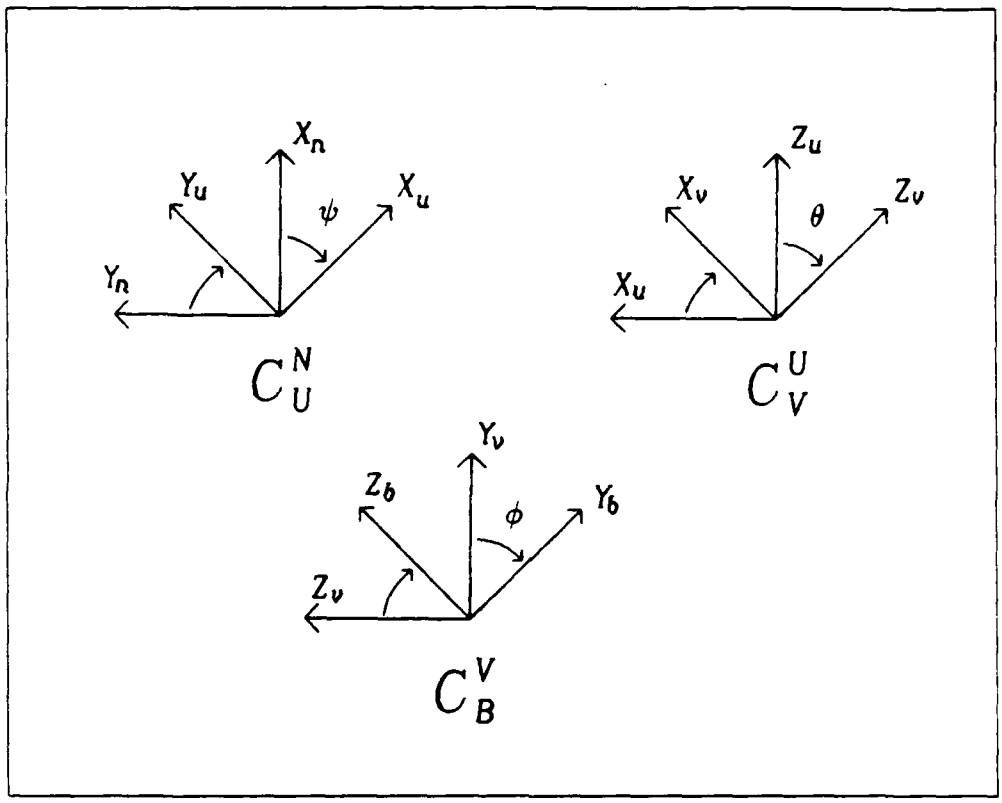

Figure 2.3. Body to Navigation Frame Transformation

defines intermediate frame U. Next, the B–frame is rotated about Y_b by the pitch angle θ. This intermediate orientation of the B–frame defines intermediate frame V. Last, the B–frame is rotated about X_b by the roll angle ϕ. This results in the new orientation of the B–frame relative to the N–frame. This sequence of rotations is shown in Figure 2.3. In terms of these three rotations, Equation (2.12) may be expressed as

$$[X]^N = C_U^N \, C_V^U \, C_B^V \, [X]^B \tag{2.13}$$

where

$$C_B^N = C_U^N \, C_V^U \, C_B^V \tag{2.14}$$

Expressed in terms of the roll, pitch, and heading angles, the three component matrices are

$$C_U^N = \begin{bmatrix} \cos\psi & \sin\psi & 0 \\ -\sin\psi & \cos\psi & 0 \\ 0 & 0 & 1 \end{bmatrix}$$

$$C_V^U = \begin{bmatrix} \cos\theta & 0 & -\sin\theta \\ 0 & 1 & 0 \\ \sin\theta & 0 & \cos\theta \end{bmatrix}$$

$$C_B^V = \begin{bmatrix} 1 & 0 & 0 \\ 0 & \cos\phi & \sin\phi \\ 0 & -\sin\phi & \cos\phi \end{bmatrix}$$

thus

$$C_B^N = \begin{bmatrix} \cos\psi\cos\theta & \sin\psi\cos\phi + \cos\psi\sin\theta\sin\phi & \sin\psi\sin\phi - \cos\psi\sin\theta\cos\phi \\ -\sin\psi\cos\theta & \cos\psi\cos\phi - \sin\psi\sin\theta\sin\phi & \cos\psi\sin\phi + \sin\psi\sin\theta\cos\phi \\ \sin\theta & -\cos\theta\sin\phi & \cos\theta\cos\phi \end{bmatrix} \tag{2.15}$$

A related quantity that is required in Chapter III is $\boldsymbol{\omega}_{NB}^B$, the B-frame expression of the N-frame to B-frame angular velocity vector. This vector is computed as

$$\boldsymbol{\omega}_{NB}^B = C_V^B C_U^V \begin{bmatrix} 0 \\ 0 \\ \dot{\psi} \end{bmatrix}^U + C_V^B \begin{bmatrix} 0 \\ \dot{\theta} \\ 0 \end{bmatrix}^V + \begin{bmatrix} \dot{\phi} \\ 0 \\ 0 \end{bmatrix}^B . \tag{2.16}$$

The result is

$$\boldsymbol{\omega}_{NB}^B = \begin{bmatrix} 1 & 0 & \sin\theta \\ 0 & \cos\phi & -\sin\phi\cos\theta \\ 0 & \sin\phi & \cos\phi\cos\theta \end{bmatrix} \begin{bmatrix} \dot{\phi} \\ \dot{\theta} \\ \dot{\psi} \end{bmatrix} \tag{2.17}$$

2.3 Kalman Filter Theory

A Kalman filter is a recursive data processing algorithm used to compute time-dependent estimates of quantities of interest. When certain assumptions are made, the Kalman filter algorithm has been mathematically proven to be optimal with respect to several criteria [8]. The term "Kalman filter" is used to describe several variations of a common algorithmic basis. The model of a continuous-time linear system with discrete-time linear measurements is used here to present the Kalman filter concept.

The dynamics of the continuous-time system are assumed well modeled by a set of n coupled first-order linear differential equations during some time period of interest, T.

Such a description of a physical system is termed a *state-variable* model. These equations are written using vector/matrix notation as

$$\dot{\mathbf{x}}(t) = \mathbf{F}(t)\mathbf{x}(t) + \mathbf{B}(t)\mathbf{u}(t) + \mathbf{G}(t)\mathbf{w}(t) \tag{2.18}$$

where $\mathbf{F}$ is a n-by-n matrix describing the undriven (homogeneous) state dynamics, $\mathbf{x}$ is a n-by-1 state vector, $\mathbf{B}$ is a n-by-r control distribution matrix, $\mathbf{u}$ is a r-by-1 deterministic control input vector, $\mathbf{G}$ is a n-by-s driving noise distribution matrix, and $\mathbf{w}$ is a s-by-1 stochastic driving noise vector. The matrices $\mathbf{F}$, $\mathbf{B}$, $\mathbf{G}$, and the vector $\mathbf{u}$ are, in general, piecewise continuous functions of time. The elements of the vector $\mathbf{w}$ are required to be *white* with zero-mean Gaussian statistics. The term "white" means uncorrelated in time. This concept is described mathematically by

$$E\{\mathbf{w}(t)\} = \mathbf{0} \tag{2.19}$$

$$E\{\mathbf{w}(t)\,\mathbf{w}^T(t')\} = \mathbf{Q}(t)\,\delta(t-t') \tag{2.20}$$

where the notation $E\{\cdot\}$ denotes *expected value.* Matrix $\mathbf{Q}$ is the s-by-s driving noise *strength* matrix, and $\delta(t-t')$ in the *Dirac delta* (unit impulse) function. Matrix $\mathbf{Q}$ is symmetric, positive semidefinite, and whose diagonal elements represent the power spectral densities, constant at all frequencies, of the corresponding scalar elements of $\mathbf{w}$.

At discrete times $t_i \in T$, m noise-corrupted measurements are available. These measurements, assumed to be linear combinations of the states and *white* discrete-time measurement noises, are described by

$$\mathbf{z}_i \equiv \mathbf{z}(t_i) = \mathbf{H}(t_i)\,\mathbf{x}(t_i) + \mathbf{v}(t_i) \tag{2.21}$$

where $\mathbf{z}$ is the m-by-1 measurement vector, $\mathbf{H}$ is the m-by-n measurement (state observation) matrix, $\mathbf{x}$ is the n-by-1 state vector. and $\mathbf{v}$ is the m-by-1 stochastic measurement noise vector. The elements of $\mathbf{v}$ are required to be *white* with zero-mean, Gaussian statistics described by

$$E\{\mathbf{v}(t_i)\} = \mathbf{0} \tag{2.22}$$

$$E\{\mathbf{v}(t_i)\,\mathbf{v}^T(t_j)\} = \begin{cases} \mathbf{R}(t_i) & t_i = t_j \\ \mathbf{0} & t_i \neq t_j \end{cases} \tag{2.23}$$

where $\mathbf{R}$ is symmetric, positive definite, and may be interpreted as the covariance of $\mathbf{v}$ at time t_i. Furthermore, the measurement noises for each measurement type are usually assumed uncorrelated with each other. This assumption results in a diagonal $\mathbf{R}$ matrix. When $\mathbf{R}$ is diagonal, the measurements may be incorporated sequentially at each measurement time. For a standard linear Kalman filter, the final result does not depend on the order in which the measurements are incorporated.

The filter state estimate $\hat{\mathbf{x}}$ is interpreted as the mean value of a *Gaussian* conditional probability density function (PDF) with covariance $\mathbf{P}$. The Gaussian requirement implies that $\hat{\mathbf{x}}$ is also the mode (most likely value) for the conditional PDF. This PDF is conditioned on $\mathbf{Z}_i$, the measurement history through time t_i. This conditional PDF is described by

$$f_{\mathbf{x}(t_i)|\mathbf{Z}(t_i)}(\boldsymbol{\xi} \mid \mathbf{Z}_i) = \left[(2\pi)^{n/2} \mid \mathbf{P}(t_i^+) \mid^{1/2}\right]^{-1} \exp\left\{-\frac{1}{2}\left[\boldsymbol{\xi} - \hat{\mathbf{x}}(t_i^+)\right]^T \mathbf{P}(t_i^+)^{-1}\left[\boldsymbol{\xi} - \hat{\mathbf{x}}(t_i^+)\right]\right\} \quad (2.24)$$

(Superscripts "+" and "–" appearing with t_i are used throughout this thesis to indicate "just after" and "just before" a measurement update, respectively). The function of the Kalman filter is to propagate this conditional probability density function forward in time between measurements and to update the density function when measurements are available. The filtering process is started from the initial estimates of the state vector, $\hat{\mathbf{x}}_0$, and covariance, $\mathbf{P}_0$, where

$$\hat{\mathbf{x}}_0 = E\{\mathbf{x}(t_0)\} \quad (2.25)$$

$$\mathbf{P}_0 = E\{[\mathbf{x}(t_0) - \hat{\mathbf{x}}_0][\mathbf{x}(t_0) - \hat{\mathbf{x}}_0]^T\} \quad (2.26)$$

The state estimate and covariance are propagated from measurement time t_i^+ (or initial time) to measurement time t_{i+1}^- by (numerical) integration of

$$\dot{\hat{\mathbf{x}}}(t/t_i) = \mathbf{F}(t)\hat{\mathbf{x}}(t/t_i) + \mathbf{B}(t)\mathbf{u}(t) \quad (2.27)$$

$$\dot{\mathbf{P}}(t/t_i) = \mathbf{F}(t)\mathbf{P}(t/t_i) + \mathbf{P}(t/t_i)\mathbf{F}^T(t) + \mathbf{G}(t)\mathbf{Q}(t)\mathbf{G}^T(t) \quad (2.28)$$

The notation "t/t_i" is used to indicate time t in the interval $\left[t_i^+, t_{i+1}^-\right]$ where all measurements through time t_i have been incorporated in the filter estimates $\hat{\mathbf{x}}$ and $\mathbf{P}$. At measurement times t_i, these two quantities are updated using

$$\mathbf{K}(t_i) = \mathbf{P}(t_i^-)\mathbf{H}^T(t_i)\left[\mathbf{H}(t_i)\mathbf{P}(t_i^-)\mathbf{H}^T(t_i) + \mathbf{R}(t_i)\right]^{-1} \tag{2.29}$$

$$\hat{\mathbf{x}}(t_i^+) = \hat{\mathbf{x}}(t_i^-) + \mathbf{K}(t_i)\left[\mathbf{z}_i - \mathbf{H}(t_i)\hat{\mathbf{x}}(t_i^-)\right] \tag{2.30}$$

$$\mathbf{P}(t_i^+) = \mathbf{P}(t_i^-) - \mathbf{K}(t_i)\mathbf{H}(t_i)\mathbf{P}(t_i^-) \tag{2.31}$$

The quantity $\mathbf{K}$ is called the Kalman filter gain. Note that $\mathbf{K}$ and $\mathbf{P}$ do not depend on the history of the measurement vectors $\mathbf{z}_1$, $\mathbf{z}_2$, $\mathbf{z}_3$,...$\mathbf{z}_i$. This important fact allows the filter gain and covariance to be precomputed. However, this holds true only for the case of linear dynamics and measurements. The derivation of these equations is presented in Chapter 5 of reference [8]. Differences between the standard Kalman filter structure presented here and the Kalman filter actually implemented for this research are discussed later.

2.4 *Time Correlated Errors and Residual Characteristics*

The basic Kalman filter presented above assumes all driving and measurement noises are white. The plot of the power spectral density (PSD) of such a white noise is a horizontal line over all frequencies; a white noise contains equal power at all frequencies. A continuous–time white noise is therefore an infinite power process and thus cannot really exist. "Whiteness" is still a valid and useful characteristic for many noise models provided the white noise adequately models the real noise within the bandpass of the system of interest. In cases where the time correlation of th. noise cannot be neglected, the concept of a *shaping filter* is used to model the time correlation properties of the noise. Such a noise is modeled by one or more additional states, x_j, which are augmented to the basic state vector. The Kalman filter described in this thesis involves three simple types of shaping filters: the random bias, the random walk (Brownian motion), and the first–order Gauss–Markov process.

The term *random bias* describes a quantity with an unknown, random, initial value with a Gaussian PDF. The value of the quantity does not change after the initial time; it

remains a constant bias. The differential equation describing this concept is simply

$$\dot{x}(t) = 0 \tag{2.32}$$

with

$$x(t_0) = x_0, \qquad x_0 \in N[0, \sigma^2_{x_0}]$$

The term *random walk* is a synonym for Brownian motion. Since white noise is conceptually the derivative of a Brownian motion process, the differential equation describing random walk is

$$\dot{x}(t) = w(t) \tag{2.33}$$

Quantities that are known to be constant biases are frequently modeled, in the Kalman filter design, with random walk shaping filters. In these cases, the "$w(t)$" appearing in Equation (2.33) is a small strength *pseudonoise* employed simply to prevent the corresponding elements of the covariance matrix and, in turn, the Kalman gain matrix, from becoming and remaining zero. If the filter covariance associated with a particular state becomes zero, then subsequent measurements will have no impact on the filter estimate of that state.

The term *first-order Gauss-Markov* describes a process with exponentially decaying time correlation. The differential equation describing such a process is

$$\dot{x}(t) = -\frac{1}{\tau}x(t) + w(t) \tag{2.34}$$

where τ is the correlation time. The autocorrelation function and PSD plots for a first-order Markov process are shown in Figure 2.4. The first-order Markov process shaping filter is seen to be a simple low-pass filter; it attenuates the high-frequency content of the white noise. More complex (higher order) shaping filters may be synthesized to match the PSD of almost any real noise, but no such filters were considered necessary for this research.

The quantity $[\mathbf{z}_i - \mathbf{H}\hat{\mathbf{x}}]$ appearing in Equation (2.30) is called the measurement *residual*, $\mathbf{r}_i$. The residual vector is the difference between the actual measurement vector $\mathbf{z}_i$, at time t_i and the "expected" measurement vector, $\mathbf{H}(t_i)\,\hat{\mathbf{x}}(t_i^-)$. That is,

$$\mathbf{r}_i \equiv \mathbf{r}(t_i) = \mathbf{z}_i - \mathbf{H}\hat{\mathbf{x}} \tag{2.35}$$

Ideally, the statistics of the residual vector residuals are described by

$$E\{\mathbf{r}_i\} = \mathbf{0} \tag{2.36}$$

$$E\{\mathbf{r}_i\mathbf{r}_i^T\} = \mathbf{H}(t_i)\mathbf{P}(t_i^-)\mathbf{H}^T(t_i) + \mathbf{R}(t_i) \tag{2.37}$$

An example of such an ideal residual time history is shown in Figure 2.5. When all significant processes, including time correlated noises, are adequately described in a state–space model, and the Kalman filter based on this model has is properly *tuned*, the true estimation error $\mathbf{e}(t)$ defined by

$$\mathbf{e}(t) \equiv \hat{\mathbf{x}}(t) - \mathbf{x}(t) \tag{2.38}$$

can be shown to have Gaussian statistics described by

$$E\{\mathbf{e}(t)\} = \mathbf{0} \tag{2.39}$$

$$E\{\mathbf{e}(t)\mathbf{e}^T(t)\} = \mathbf{P}(t) \tag{2.40}$$

Thus a *correctly tuned* Kalman filter based on the *complete* state–space model is an unbiased estimator; its estimates have zero mean error. The state covariance estimate, $\mathbf{P}(t)$, propagated and updated by the filter is seen to be equal to the covariance of the true estimation error.

2.5 Extended Kalman Filter and Error State Concepts

In many cases, the dynamics and/or the measurements involved in a state–variable model cannot be adequately described by linear equations. In such cases, the nonlinear equations corresponding to Equations (2.18) and (2.21) are

$$\dot{\mathbf{x}}(t) = \mathbf{f}[\mathbf{x}(t), \mathbf{u}(t), t] + \mathbf{G}(t)\mathbf{w}(t) \tag{2.41}$$

$$\mathbf{z}(t_i) = \mathbf{h}[\mathbf{x}(t_i), t_i] + \mathbf{v}(t_i) \tag{2.42}$$

where $\mathbf{f}$ is the nonlinear dynamics function and $\mathbf{h}$ is the nonlinear measurement function. Note that both the dynamics driving noise and the measurement noise are still linearly additive.

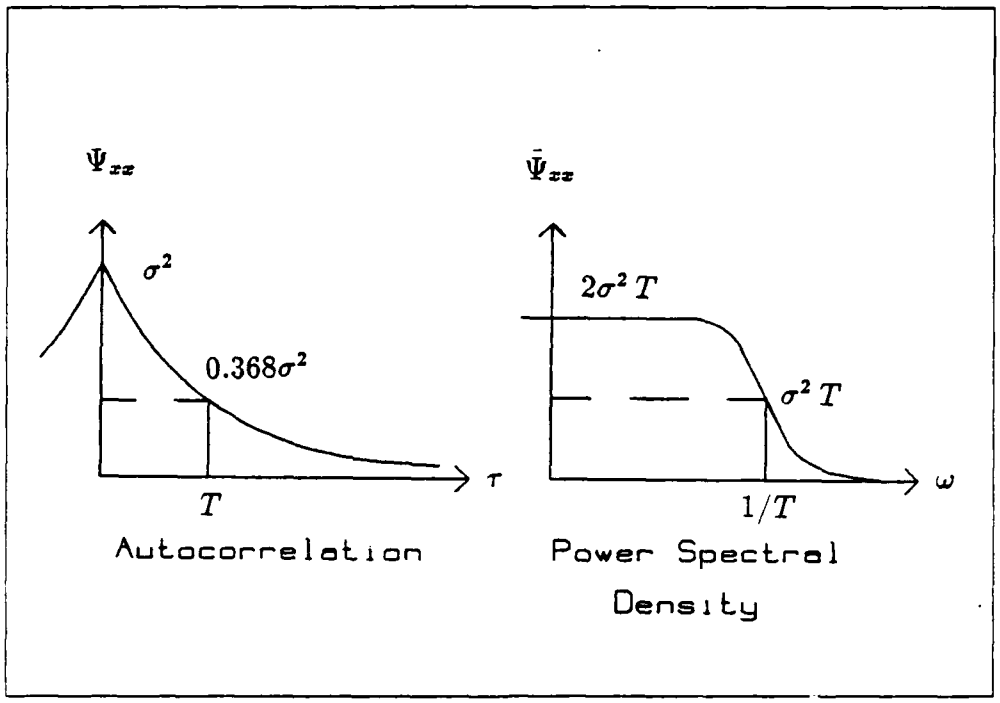

Figure 2.4. First-Order Markov Characteristics

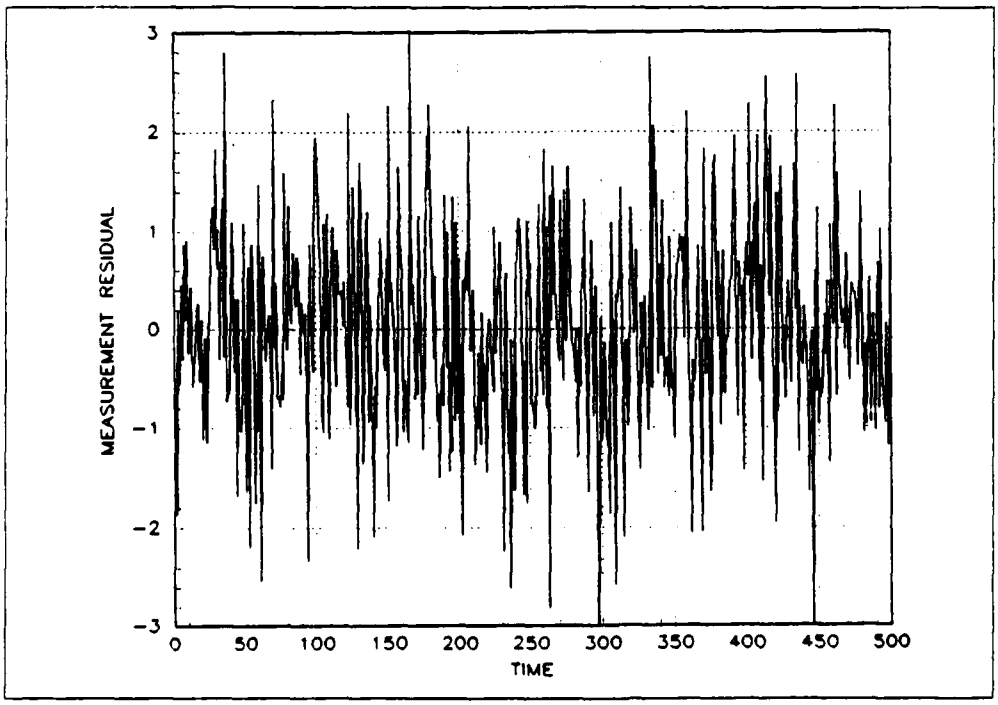

Figure 2.5. Example of a "White" Residual Sequence

The *extended Kalman filter* provides a state estimation algorithm for such nonlinear systems. It can be derived from the standard Kalman filter using a linear perturbation procedure based on first–order Taylor series approximations [9]. The state and covariance propagation from time t_i to time t_{i+1} is accomplished via (numerical) integration of the equations

$$\dot{\hat{\mathbf{x}}}(t/t_i) = \mathbf{f}[\hat{\mathbf{x}}(t/t_i), \mathbf{u}(t), t] \tag{2.43}$$

$$\dot{\mathbf{P}}(t/t_i) = \mathbf{F}[t; \hat{\mathbf{x}}(t/t_i)]\mathbf{P}(t/t_i) + \mathbf{P}(t/t_i)\mathbf{F}^T[t; \hat{\mathbf{x}}(t/t_i)] + \mathbf{G}(t)\mathbf{Q}(t)\mathbf{G}^T(t) \tag{2.44}$$

where

$$\mathbf{F}[t; \hat{\mathbf{x}}(t/t_i)] \equiv \left.\frac{\partial \mathbf{f}[\mathbf{x}, \mathbf{u}(t), t]}{\partial \mathbf{x}}\right|_{\mathbf{x}=\hat{\mathbf{x}}(t/t_i)} \tag{2.45}$$

At a measurement time t_i, the extended Kalman filter updates the state and covariance using the equations

$$\mathbf{K}(t_i) = \mathbf{P}(t_i^-)\,\mathbf{H}^T[t_i; \hat{\mathbf{x}}(t_i^-)]\,\{\mathbf{H}[t_i; \hat{\mathbf{x}}(t_i^-)]\,\mathbf{P}(t_i^-)\,\mathbf{H}^T[t_i; \hat{\mathbf{x}}(t_i^-)] + \mathbf{R}(t_i)\}^{-1} \tag{2.46}$$

$$\hat{\mathbf{x}}(t_i^+) = \hat{\mathbf{x}}(t_i^-) + \mathbf{K}(t_i)\,\{\mathbf{z}_i - \mathbf{h}[\hat{\mathbf{x}}(t_i^-), t_i]\} \tag{2.47}$$

$$\mathbf{P}(t_i^+) = \mathbf{P}(t_i^-) - \mathbf{K}(t_i)\,\mathbf{H}[t_i; \hat{\mathbf{x}}(t_i^-)]\,\mathbf{P}(t_i^-) \tag{2.48}$$

where

$$\mathbf{H}[t_i; \hat{\mathbf{x}}(t_i^-)] \equiv \left.\frac{\partial \mathbf{h}[\mathbf{x}, t_i]}{\partial \mathbf{x}}\right|_{\mathbf{x}=\hat{\mathbf{x}}(t_i^-)} \tag{2.49}$$

Note the structural similarity of the extended Kalman filter equations to the standard Kalman filter equations presented earlier. The major differences are that the nonlinear dynamics equation is used for propagation of the state estimates and the nonlinear measurement equation is used in formulating the measurement residual. The matrices **F** and **H** are, in general, functions of the state estimates as a result of the linearization process. This state dependency prevents the filter gain and covariance estimates from being precomputed. The accuracy and stability of an extended Kalman filter's state and covariance estimates are dependent on the adequacy of the linearization process for the system of interest. As a result of the the approximations involved in the calculation of **F** and **H**, the state estimates produced by an extended Kalman filter cannot be mathematically

proven to be optimal. Even so, extended Kalman filters may work very well for certain applications [9].

Another important concept used in this thesis is that of *error states*. Instead of directly estimating the numeric value of some state, it may be more convenient to estimate the error, $\delta \mathrm{x}$, in the true value of that state relative to some nominal value x_n. That is,

$$\delta \mathrm{x}(t) = \mathrm{x}(t) - \mathrm{x}_n(t) \tag{2.50}$$

and the Kalman filter estimate of $\delta \mathrm{x}$ is $\widehat{\delta \mathrm{x}}$. Since the nominal value is known for all $t \in T$, the (indirect) filter estimate of the whole valued state is calculated as

$$\widehat{\mathrm{x}}(t) = \mathrm{x}_n(t) + \widehat{\delta \mathrm{x}}(t) \tag{2.51}$$

2.6 Simulation Software

All of the data processing described in this thesis is conducted with the aid of two major software packages, MSOFE [1] and $MATRIX_X$[6]. An overview of the purpose, capabilities, and use of each of these software packages is provided below.

MSOFE is the acronym for the *Multimode Simulation for Optimal Filter Evaluation* software package. MSOFE was jointly developed by the Avionics Laboratory of Wright-Patterson AFB, Ohio, and Integrity Systems Inc. of Winchester, Massachusetts. It is a multimode simulation tool for designing and evaluating integrated systems based on optimal (Kalman) filtering techniques. The primary modes of use are Monte Carlo analysis and covariance analysis. These two modes may be used separately or simultaneously. The conceptual and mathematical basis of these two analysis techniques is described in reference [8:325–341]. MSOFE is written in ANSII standard FORTRAN 77 and can be used on any reasonably fast computer for which there is a FORTRAN 77 compiler available.

An executable MSOFE program consists of an executive routine, 56 fixed subroutines, and at least 14 user–written subroutines. It is these 14 user subroutines that allow MSOFE to be customized to handle almost any Kalman filter problem. The user subroutines required for this research involved a significant amount of original programming. Although MSOFE was conceived as a simulation tool in which the simulated measurements occur at synchronous intervals, it is easily modified to filter empirically recorded

data where the real measurements occur asynchronously. MSOFE has two companion programs called PROFGEN and MPLOT. PROFGEN generates simulated trajectory data for use in MSOFE simulations while MPLOT performs statistical calculations and provides high quality plots of MSOFE and PROFGEN output. PROFGEN was not required in this research and MPLOT was not used because it requires commercial plotting routines which are not available on AFIT computers. More information on the use and capabilities of MSOFE is available in the MSOFE User's Manual [1].

$MATRIX_X$ is a commercial software product developed by Integrated Systems Inc. of Palo Alto, California [6]. It is a powerful, general purpose, interactive program for the computer-aided design and analysis of control systems. $MATRIX_X$ implements an interpreted programming language similar to FORTRAN and it can read data files created by FORTRAN programs. Only a small portion of its capabilities were used in thisthesis effort. $MATRIX_X$ was used for interpolation and plotting of the MSOFE output. Several small FORTRAN and $MATRIX_X$ programs are used to handle routine tasks such as reading CIRIS data tapes, producing correctly formatted input data files for the MSOFE runs, and plotting data.

2.7 Summary

This chapter introduces the spatial reference frames, Kalman filter theory, and simulation software used in this research. The primary function of CIRIS is to estimate position and velocity quantities. The WGS 84 geodetic reference system is chosen as the basic reference frame for defining position and velocity. The WGS-84 system defines the earth-centered earth-fixed (E-frame) rectangular coordinate frame and the relationship between E-frame coordinates and geodetic latitude, longitude, and altitude coordinates. Several additional reference frames are required to simplify development and specification of the Advanced CIRIS filter. These include the north—west—up local-level navigation frame (N-frame), the true frame (T-frame), the platform frame (P-frame), the computer frame (C-frame), and the body frame (B-frame). These frames and the transformations between them are specified in Sections 2.1 and 2.2.

The concept and mathematical structure of the standard linear Kalman filter is

discussed in Section 2.3. This discussion is augmented with the concepts of time correlated errors, ideal measurement residual characteristics, the *extended* Kalman filter, and error states in Sections 2.4 and 2.5.

The results presented in Chapters IV and V are obtained with the aid of two major software packages. The first is the *Multimode Simulation for Optimal Filter Evaluation* (MSOFE) program. Standard MSOFE subroutines implement the propagation and measurement processing procedures generic to any Kalman filter application while additional, user–written, subroutines customize MSOFE for a particular application. The second software package is $MATRIX_X$, a control system design and analysis program. $MATRIX_X$ is used here only for data interpolation and data plotting. These two software packages are described in more detail in Section 2.6

III. 70-State Filter Description

The Advanced CIRIS filter described in this chapter is basically identical to the 70–state filter described by Solomon [13] except for four significant changes. The first change is that the measurement models are developed using an extended Kalman filter formulation rather than a linearized Kalman filter formulation. The second change is that the filter is updated with barometric altitude measurements in addition to the transponder range and range–rate measurements. The third change is that the atmospheric propagation delay is modeled as being range–dependent rather than range–independent, and that the atmospheric delays associated with the different transponders have non–zero correlation. The fourth change is the compensation for the position and motion of the CIRIS interrogator antenna relative to the INS. In the past, this lever arm correction was provided by the CIRIS II software.

3.1 Notation

The primary function of the filter is to produce accurate estimates of the position and velocity of the CIRIS LN–39 INS during a specified time interval. The mathematical equations which describe the filter's computations require rather complex notation. This section defines terms and explains notation.

The measurements processed by the filter are *range* and *range–rate* measurements provided by the Cubic Range and Range–Rate Subsystem (RRS) and a *barometric altitude* measurement provided by the central air data computer (CADC). The principle components of the Cubic RRS are the transponder electronics, transponder antennas, interrogator electronics, and interrogator antenna. The filter estimation of the position and velocity of the INS requires estimates of the position and velocity of the transponder antennas and the interrogator antenna.

Let the position vectors of the jth transponder antenna, the interrogator antenna, and INS be denoted by $\boldsymbol{P}_{T_j}$, $\boldsymbol{P}_A$, and $\boldsymbol{P}_I$, respectively. In the E–frame, these positions

are shown in terms of their components as

$$\boldsymbol{P}_{T_j}^E \equiv \begin{bmatrix} X_{T_j} \\ Y_{T_j} \\ Z_{T_j} \end{bmatrix}^E \qquad \boldsymbol{P}_A^E \equiv \begin{bmatrix} X_A \\ Y_A \\ Z_A \end{bmatrix}^E \qquad \boldsymbol{P}_I^E \equiv \begin{bmatrix} X_I \\ Y_I \\ Z_I \end{bmatrix}^E$$

The familiar "dot" ($\dot{}$) notation is used to indicate differentiation with respect to time. Thus the E–frame velocities of these three points are denoted as

$$\dot{\boldsymbol{P}}_{T_j}^E \equiv \begin{bmatrix} \dot{X}_{T_j} \\ \dot{Y}_{T_j} \\ \dot{Z}_{T_j} \end{bmatrix}^E \qquad \dot{\boldsymbol{P}}_A^E \equiv \begin{bmatrix} \dot{X}_A \\ \dot{Y}_A \\ \dot{Z}_A \end{bmatrix}^E \qquad \dot{\boldsymbol{P}}_I^E \equiv \begin{bmatrix} \dot{X}_I \\ \dot{Y}_I \\ \dot{Z}_I \end{bmatrix}^E$$

The "tilde" ($\tilde{}$) symbol is used to indicate measured or calculated quantities where the measurement or calculation process is assumed to introduce error. For example, transponder positions are provided to the filter from a database containing the surveyed (measured) transponder WGS 84 latitude, longitude, and altitude. The INS calculates its own position based on its initialization and subsequent inertial measurements. The interrogator antenna position is calculated relative to the INS position assuming a fixed B–frame offset vector and knowledge of the aircraft orientation. These measured or calculated quantities are denoted as

$$\tilde{\boldsymbol{P}}_{T_j}^E \equiv \begin{bmatrix} \tilde{X}_{T_j} \\ \tilde{Y}_{T_j} \\ \tilde{Z}_{T_j} \end{bmatrix}^E \qquad \tilde{\boldsymbol{P}}_A^E \equiv \begin{bmatrix} \tilde{X}_A \\ \tilde{Y}_A \\ \tilde{Z}_A \end{bmatrix}^E \qquad \tilde{\boldsymbol{P}}_I^E \equiv \begin{bmatrix} \tilde{X}_I \\ \tilde{Y}_I \\ \tilde{Z}_I \end{bmatrix}^E$$

Error (difference) quantities are indicated with a delta (δ) prefix. For example, the error in the indicated INS position relative to the true INS position is denoted as

$$\begin{bmatrix} \delta X_I \\ \delta Y_I \\ \delta Z_I \end{bmatrix}^E = \begin{bmatrix} \tilde{X}_I \\ \tilde{Y}_I \\ \tilde{Z}_I \end{bmatrix}^E - \begin{bmatrix} X_I \\ Y_I \\ Z_I \end{bmatrix}^E$$

Finally, filter estimates of a quantity are indicated by a "hat" ($\hat{}$) symbol. For example, if the E–frame X, Y, and Z errors in the INS position are three of the filter states, the filter

estimates of these states are denoted as

$$\begin{bmatrix} \widehat{\delta X}_I \\ \widehat{\delta Y}_I \\ \widehat{\delta Z}_I \end{bmatrix}^E$$

The (indirect) filter estimate of the true INS position is calculated by subtracting the filter estimate of the error in the INS indicated position from the INS indicated position. This concept is formulated as

$$\begin{bmatrix} \hat{X}_I \\ \hat{Y}_I \\ \hat{Z}_I \end{bmatrix}^E = \begin{bmatrix} \tilde{X}_I \\ \tilde{Y}_I \\ \tilde{Z}_I \end{bmatrix}^E - \begin{bmatrix} \widehat{\delta X}_I \\ \widehat{\delta Y}_I \\ \widehat{\delta Z}_I \end{bmatrix}^E$$

The symbolic order of operations is important. For example, $\widehat{\delta \dot{Z}}_I$ indicates the filter estimate of the error in the indicated INS *velocity* along the Z axis while $\dot{\widehat{\delta Z}}_I$ indicates the time rate of change *of the filter estimate* of the error in indicated INS *position* along the Z axis.

3.2 Error State Vector

This version of the Advanced CIRIS filter models 70 error quantities. The error state vector is partitioned into four subvectors which group related error states. The total error state vector is denoted as $\delta\mathbf{x}$. The subvectors are defined as follows: $\delta\mathbf{x}_1$ contains the 13 general INS dynamics errors such as position, attitude, velocity, and vertical channel errors; $\delta\mathbf{x}_2$ contains 12 additional INS gyro and accelerometer errors; $\delta\mathbf{x}_3$ contains 3 baro–altimeter errors; and $\delta\mathbf{x}_4$ contains all 42 transponder related errors. While many of the individual elements of $\delta\mathbf{x}$ are defined along a specific axis of either the T–frame or the E–frame, others are defined along time varying line–of–sight directions or do not correspond to a spatial direction at all. Thus it is not correct to think of the whole $\delta\mathbf{x}$ vector as being coordinatized in a particular 3–dimensional spatial reference frame; the elements of $\delta\mathbf{x}$ are the coordinates of a point in a 70–dimensional *error state-space*. In general, the elements of subvectors $\delta\mathbf{x}_1$, $\delta\mathbf{x}_2$, and $\delta\mathbf{x}_3$ are defined relative to the T–frame while the elements of subvector $\delta\mathbf{x}_4$ are defined relative to the E–frame. The individual

elements of $\delta\mathbf{x}$ and their associated initial 1σ value are defined in Appendix A, Tables A.1 thru A.6. The most significant error states, those in subvectors $\delta\mathbf{x}_1$,$\delta\mathbf{x}_3$, and $\delta\mathbf{x}_4$, are described in more detail below. The elements of error state subvector $\delta\mathbf{x}_2$, while necessary for the completeness of the INS error model, are more difficult to visualize. For more information on these error quantities the reader is referred to the Litton LN-39 Systems Engineering Analysis Report [14].

3.2.1 INS Primary Error State Subvector The errors in the INS indicated position and platform wander angle are modeled by the four error states $\delta\Theta_X$, $\delta\Theta_Y$, $\delta\Theta_Z$, and δh. Error states $\delta\Theta_X$, $\delta\Theta_Y$, and $\delta\Theta_Z$ are the error angles appearing in Equation (2.6). Together, they define the INS latitude, longitude, and platform wander angle errors, while error state δh defines the INS altitude (vertical position) error. Their relation of the $\delta\Theta$ error angles to the more familiar latitude (δL), longitude ($\delta\lambda$), and wander angle ($\delta\alpha$) errors is

$$\begin{bmatrix} \delta L \\ \delta\lambda \\ \delta h \end{bmatrix} = \begin{bmatrix} \sin\alpha & \cos\alpha & 0 \\ \cos\alpha\sec L & -\sin\alpha\sec L & 0 \\ 0 & 0 & 1 \end{bmatrix} \begin{bmatrix} \delta\Theta_X \\ \delta\Theta_Y \\ \delta h \end{bmatrix} \tag{3.1}$$

and

$$\delta\alpha = -(\cos\alpha\tan L)\,\delta\Theta_X + (\sin\alpha\tan L)\,\delta\Theta_Y + \delta\Theta_Z \tag{3.2}$$

These equations are taken from the Litton LN-39 Systems Engineering Analysis Report [14]. The error quantity $\delta\alpha$ is explicitly computed to correct the INS indicated wander angle for use in calculating the state dynamics matrix and various coordinate transformation matrices.

The latitude and longitude errors shown in Equation (3.1) are in angular units (radians). The transformation which converts these errors to linear distance units coordinatized in the N-frame is

$$\begin{bmatrix} \delta N \\ \delta W \\ \delta U \end{bmatrix}^N = \begin{bmatrix} (R+h) & 0 & 0 \\ 0 & -(R+h)\cos L & 0 \\ 0 & 0 & 1 \end{bmatrix} \begin{bmatrix} \delta L \\ \delta\lambda \\ \delta h \end{bmatrix} \tag{3.3}$$

where

$$R = A(1 - f\sin^2 L) \tag{3.4}$$

is the radius from the center of the WGS 84 ellipsoid to a point on its surface at latitude L. When Equations (3.1) and (3.3) are combined, the result is

$$\begin{bmatrix} \delta N \\ \delta W \\ \delta U \end{bmatrix}^N = \begin{bmatrix} (R+h)\sin\alpha & (R+h)\cos\alpha & 0 \\ -(R+h)\cos\alpha & (R+h)\sin\alpha & 0 \\ 0 & 0 & 1 \end{bmatrix} \begin{bmatrix} \delta\Theta_X \\ \delta\Theta_Y \\ \delta h \end{bmatrix} \tag{3.5}$$

The transformation matrix, $\boldsymbol{T}_X^N$, appearing in Equation (3.5) is used in the similarity transformation for transforming the filter computed covariances associated with $\delta\Theta_X$, $\delta\Theta_Y$, and δh into the corresponding N–frame covariances.

The error in the INS platform orientation relative to the true local–level plane is modeled by the error states ϕ_X, ϕ_Y, and ϕ_Z. These three error states are the misalignment angles appearing in Equation (2.5). Together, they describe the platform tilt relative to the T–frame.

The error in the INS indicated velocity is modeled by the error states δV_X, δV_Y, and δV_Z. These three error states are defined as the components of the difference vector between the INS computed (C–frame) velocity and the true (T–frame) velocity. These three error states may be transformed into equivalent N–frame velocity errors by compensating for the platform wander angle. The transformation is

$$\begin{bmatrix} \delta\dot{N} \\ \delta\dot{W} \\ \delta\dot{U} \end{bmatrix}^N = \begin{bmatrix} \cos\alpha & -\sin\alpha & 0 \\ \sin\alpha & \cos\alpha & 0 \\ 0 & 0 & 1 \end{bmatrix} \begin{bmatrix} \delta V_X \\ \delta V_Y \\ \delta V_Z \end{bmatrix} \tag{3.6}$$

The transformation matrix, $\boldsymbol{C}_P^N$, appearing in Equation (3.6) is used in the similarity transformation for transforming the filter computed covariances associated with δV_X, δV_Y, and δV_Z into the corresponding N–frame covariances.

The three error states δh_l, δS_3, and δS_4 model errors in quantities used internally by the INS for calculating vertical channel aiding gains. The LN-39 requires baro-altimeter aiding for stabilization of the vertical channel. Figure 3.1 is taken from reference [14] to illustrate the LN-39 vertical channel error model. The INS indicated altitude is lagged (held) for one second before being compared to the baro-altimeter indicated altitude. This one second wait is used to compensate for the delay inherent in baro-altimeter operation. The difference signal, $\tilde{h}(t_{i-1}) - \tilde{h}_b(t_i)$, is used by four different vertical channel aiding loops within the LN-39. The aiding gains for these loops are designated K_1, K_2, K_3, and K_4. They are nonlinear functions of the rate of change of the baro-altimeter indicated altitude, $\dot{h}_b$. The Litton LN-39 Systems Engineering Analysis Report defines these gains as

$$K_1 = \frac{3}{\lambda} \tag{3.7}$$

$$K_2 = \frac{2g_0}{A} + \frac{4}{\lambda^2} \tag{3.8}$$

$$K_3 = \frac{2}{\lambda^3} \tag{3.9}$$

$$K_4 = \frac{\Delta^2}{\Delta_0^2 + \Delta^2} \tag{3.10}$$

where

$$\Delta = |\dot{h}_b| \tag{3.11}$$

$$\Delta_0 = \begin{cases} \Delta_0 + 8 & \text{if } \Delta_0 \leq \Delta \\ \Delta_0 - 8 & \text{if } \Delta_0 > \Delta \text{ and } \Delta_0 > 38 \\ 30\ ft/sec & \textit{otherwise (and initially)} \end{cases} \tag{3.12}$$

$$\lambda = 100\left[1 + \left(\frac{\Delta}{\Delta_0}\right)^2\right] \tag{3.13}$$

Note that Δ_0 changes in discrete increments (0,+8, or -8) each time it is recalculated. This implies the aiding gains also change in discrete increments.

The dynamics matrix elements for error states δh_l, δS_3, and δS_4 are listed in Appendix A, Tables A.7 through A.9. Note that the differential equation for $\delta \dot{S}_4$ contains discontinuities due to its dependence on K_4. Within the filter software, the aiding gains are

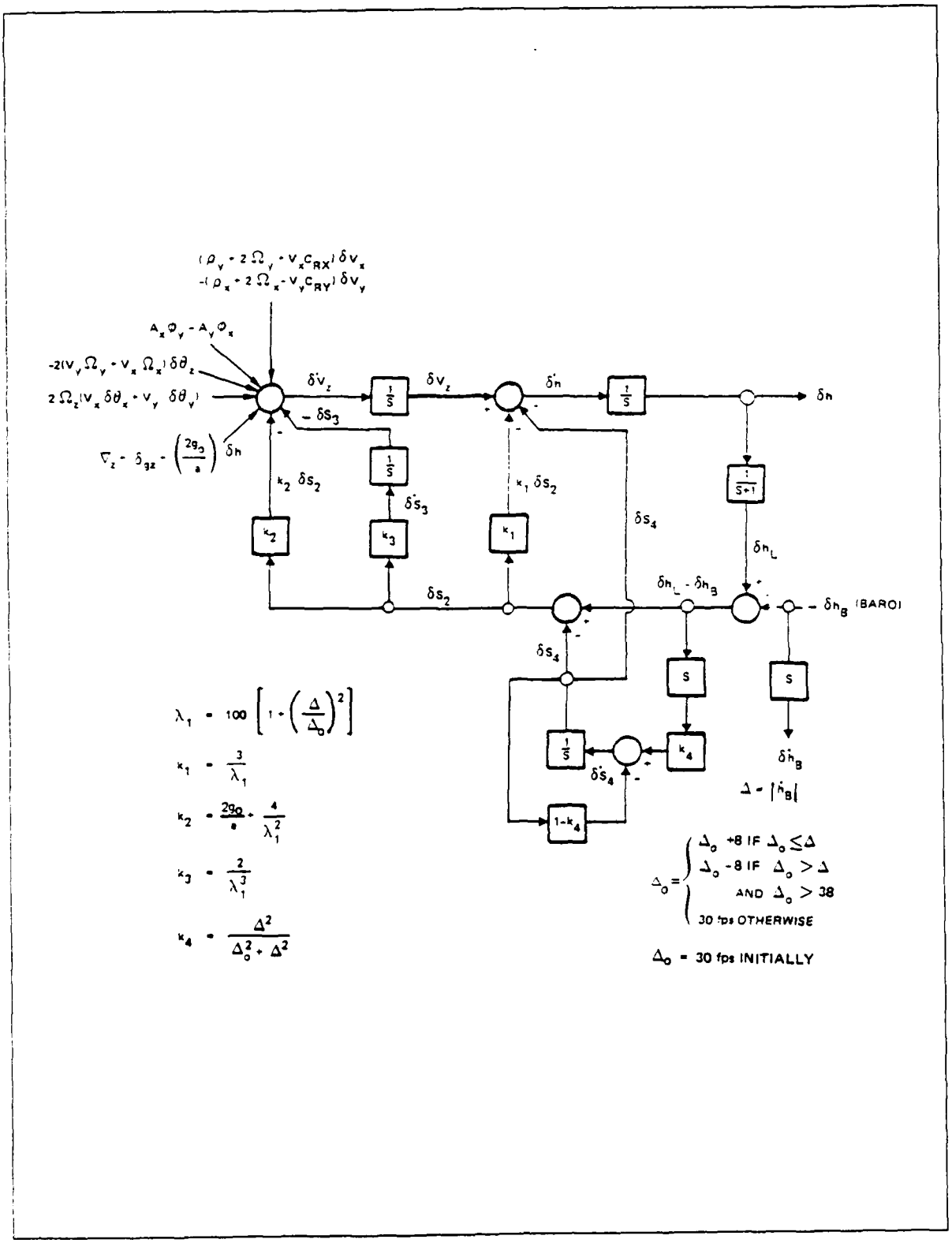

Figure 3.1. LN-39 INS Vertical Channel Error Model

recalculated only after each measurement update cycle so that the $\delta \dot{S}_4$ differential equation is continuous throughout each propagation cycle.

The initial 1σ values for the 13 states in subvector $\delta \mathbf{x}_1$ are specified in Appendix A, Table A.1.

3.2.2 Baro–Altimeter Error State Subvector The baro-altimeter error is modeled by the three error states δh_{b1}, δh_{b2}, and δh_{b3}. State δh_{b1} represents the time–correlated component of the baro–altimeter error. It is modeled with a first–order Markov shaping filter. State δh_{b2} represents the constant bias in the baro–altimeter output. It is modeled with a random bias shaping filter. State δh_{b3} represents the altitude scale factor for the altitude dependent bias in the baro–altimeter output. It is also modeled with a random bias shaping filter. The total baro–altimeter error, δh_b, is defined in terms of these three error states and the true altitude h as

$$\delta h_b(t) \equiv \tilde{h}_b(t) - h(t) = \delta h_{b1}(t) + \delta h_{b2} + h(t)\,\delta h_{b3} \tag{3.14}$$

The initial 1σ values for these three states are specified in Appendix A, Tables A.3. The dynamics matrix elements are listed in Appendix A, Tables A.7 through A.9.

3.2.3 Transponder Error State Subvector The transponder related errors are divided into those common to all transponders and those concerning individual transponders. The common element in the range and range–rate measurements from all transponders is the interrogator. The error common to all range measurements due to an interrogator calibration bias is represented by error state δE_{rc}. The error common to all range–rate measurements due to an interrogator calibration bias is represented by error state $\delta E_{\dot{r}c}$. Both error states are modeled with random bias shaping filters.

The errors associated with an individual transponder include survey (position) errors and a range measurement error caused by atmospheric propagation delay along the line–of–sight between the transponder and the interrogator antennas. The survey errors for transponder T_j are represented by error states δX_{T_j}, δY_{T_j}, and δZ_{T_j} which model the components of the position error along the X_e, Y_e, and Z_e axes, respectively. These three error states are each modeled with random bias shaping filters. The range error due to

the atmospheric propagation delay is represented by error state δA_{T_j}. This error state is interpreted as a scale factor; the range error is the product of the scale factor and the range. Error state δA_{T_j} is modeled with a first–order Markov process shaping filter. These four types of error are illustrated in Figure 3.2. The driving noises for the δA_{T_j} error states are modeled as being correlated with each other with a positive correlation coefficient. This additional tuning parameter provides a crude model for the commonality of atmospheric conditions along the lines–of–sight to each transponder. The initial 1σ values for these 42 error states are specified in Appendix A, Tables A.4 through A.6. The dynamics matrix elements are listed in Appendix A, Tables A.7 through A.9.

The filter model includes a δX_{T_j}, δY_{T_j}, δZ_{T_j}, and δA_{T_j} error state group for each of ten different transponders ($j = 1, 2, \ldots, 10$). However, a typical CIRIS test flight involves more than ten different transponders. The filter software includes a switching subroutine which "timeshares" each of the transponder error state groups between two different transponders. This permits the filter software to process measurements from up to twenty different transponders. At any given time, one member of each transponder pair is "active" (owns the error state group) while the other is "inactive." If the filter receives a measurement from the inactive transponder, the switching subroutine saves the four error state values associated with the active transponder and reloads the four error state values previously stored for the inactive transponder. It then clears the four rows and four columns of the covariance matrix associated with these error states, saving only the diagonal elements, and resets the four diagonal elements in these rows/columns to their previously stored values. The inactive transponder is thus activated while the previously active transponder is deactivated. This procedure doubles the number of allowable transponders at the expense of losing covariance information. The off–diagonal covariance information cannot be stored and later reloaded because any of the ten transponders pairs may "switch" at any time, thus rendering the cross–correlation information invalid. The frequency of switching is minimized by pairing widely separated transponders so that it is unlikely that the interrogator will request measurements form both members in any short (10–30 minutes) time interval.

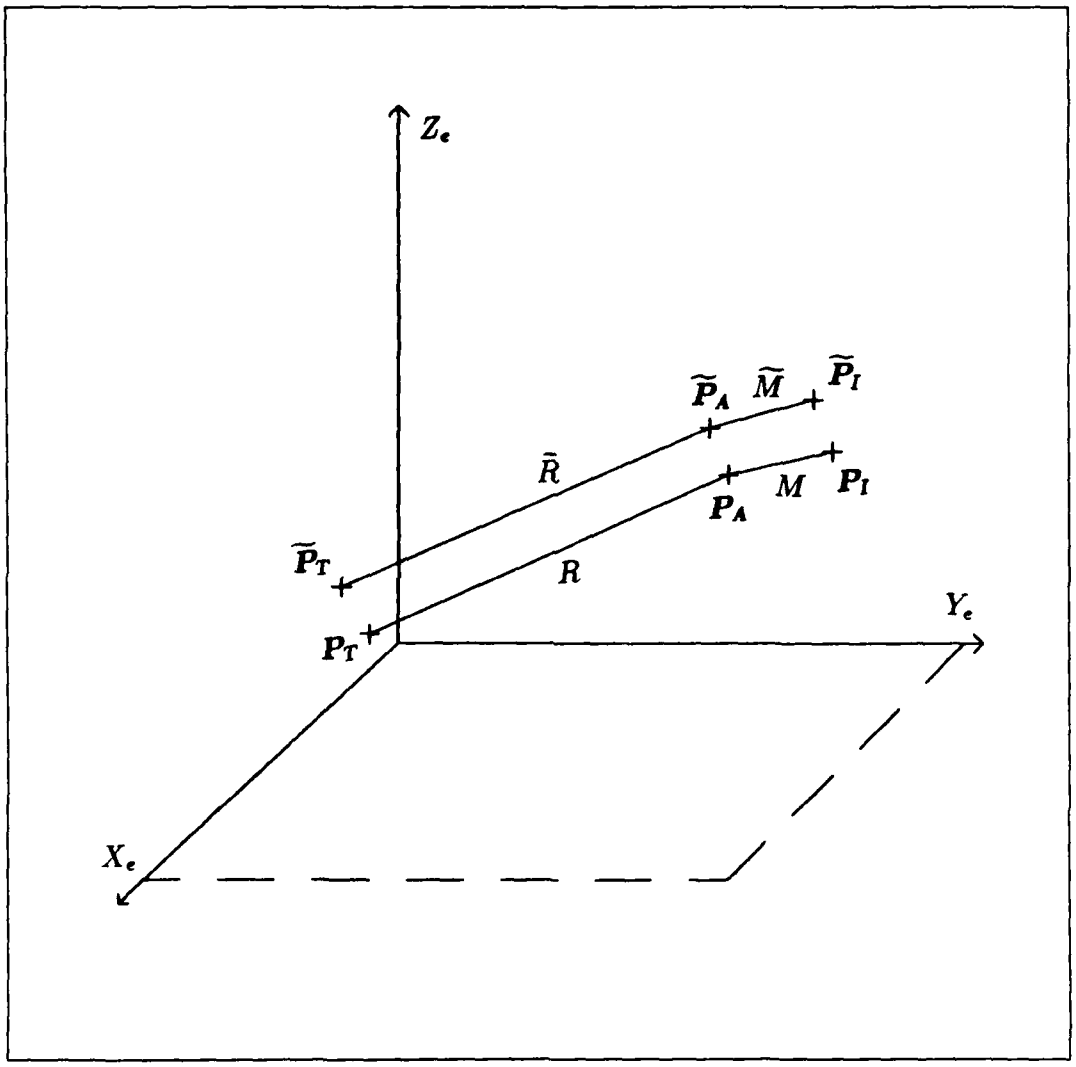

Figure 3.2. Relative Positions of Transponder, Antenna, and INS

3.3 *Error State Stochastic Differential Equation*

The dynamics of the error state vector are described by the first–order, linear, piecewise continuous, matrix differential equation

$$\dot{\delta\mathbf{x}}(t) = \mathbf{F}[t; \mathbf{x}(t)]\, \delta\mathbf{x}(t) + \mathbf{w}(t) \tag{3.15}$$

This equation is piecewise continuous because the elements of the $\mathbf{F}$ matrix that depend on the baro–altimeter aiding gains experience discontinuities at measurement times. The elements of the vector $\mathbf{w}$ represent the zero–mean white noises, if any, driving each state. The strengths of these noises are represented by a matrix $\mathbf{Q}$ which is defined in accordance with Equation (2.20).

It is useful to rewrite Equation (3.15) to illustrate the interdependencies of the error state vector partitions. The partitioned form of Equation (3.15) is

$$\begin{bmatrix} \dot{\delta\mathbf{x}}_1 \\ \dot{\delta\mathbf{x}}_2 \\ \dot{\delta\mathbf{x}}_3 \\ \dot{\delta\mathbf{x}}_4 \end{bmatrix} = \begin{bmatrix} \mathbf{F}_{1,1} & \mathbf{F}_{1,2} & \mathbf{F}_{1,3} & 0 \\ 0 & \mathbf{F}_{2,2} & 0 & 0 \\ 0 & 0 & \mathbf{F}_{3,3} & 0 \\ 0 & 0 & 0 & \mathbf{F}_{4,4} \end{bmatrix} \begin{bmatrix} \delta\mathbf{x}_1 \\ \delta\mathbf{x}_2 \\ \delta\mathbf{x}_3 \\ \delta\mathbf{x}_4 \end{bmatrix} + \begin{bmatrix} \mathbf{w}_1 \\ \mathbf{w}_2 \\ \mathbf{w}_3 \\ \mathbf{w}_4 \end{bmatrix} \tag{3.16}$$

This form of the dynamics matrix shows that subvectors $\delta\mathbf{x}_2$, $\delta\mathbf{x}_3$, and $\delta\mathbf{x}_4$ do not interact during the filter propagation cycle. Cross–coupling of these subvectors occurs only during the measurement update procedure. The non–zero elements of submatrices $\mathbf{F}_{1,1}$, $\mathbf{F}_{1,2}$, $\mathbf{F}_{1,3}$, $\mathbf{F}_{2,2}$, and $\mathbf{F}_{3,3}$ are given in Appendix A, Tables A.7 through A.9. The elements of the submatrices $\mathbf{Q}_1$, $\mathbf{Q}_3$, $\mathbf{Q}_3$, and $\mathbf{Q}_4$, which correspond to the four partitions of the $\mathbf{w}$ vector, are given in Appendix A, Table A.10. Pseudonoise is not used with any of the random bias shaping filter states because analysis using real data indicated the covariances associated with these states remained non–zero throughout the required time–interval. In general, pseudonoise with an appropriately chosen strength should be used with random bias errors.

3.4 *Measurement Models*

The filter state estimates are periodically updated with three types of measurements. A transponder interrogation occurs approximately once per second; a successful interrogation provides a range and a range–rate measurement from one of the transponders in the

current transponder set. A barometric altitude measurement is made at the same time as each transponder interrogation. Therefore the measurement vector $\mathbf{z}$ can be written in terms of its three components as

$$\mathbf{z}(t_i) = \begin{bmatrix} z_r(t_i) \\ z_{\dot{r}}(t_i) \\ z_{h_b}(t_i) \end{bmatrix} \tag{3.17}$$

where the three components are, from top to bottom, the transponder range measurement, the transponder range–rate measurement, and the barometric altitude measurement. These three measurements are processed one at a time (scalar update) by the MSOFE software. The U–D factorization scalar update procedure used by MSOFE [1] requires a *scalar* equation of the form of Equation (2.42) be specified for each of the three measurement types. Thus

$$\mathbf{h}[\mathbf{x}(t_i), t_i] = \begin{bmatrix} \mathrm{h}_r[\mathbf{x}(t_i), t_i] \\ \mathrm{h}_{\dot{r}}[\mathbf{x}(t_i), t_i] \\ \mathrm{h}_{h_b}[\mathbf{x}(t_i), t_i] \end{bmatrix} \tag{3.18}$$

where h_r, $\mathrm{h}_{\dot{r}}$, and h_{h_b} are each scalar valued equations. Each of these three functions has a corresponding 1–by–70 observation matrix row defined in accordance with Equation (2.49).

All range and range–rate measurements are defined in terms of E–frame coordinates. They must be projected into the error state vector space for correct updating of the INS error and baro–altimeter error states. This projection operation transforms the INS and baro–altimeter elements of the E–frame observation matrix into the equivalent error state–vector space observation matrix. The form of this transformation is presented in Appendix A, Table A.11 for the range measurement and in Table A.12 for the range–rate measurement.

3.4.1 Range Measurement The range measurement is provided by the Cubic RRS. Ideally, the range measurement is the line–of–sight distance between the transponder and interrogator antennas plus a known bias caused by propagation delay in the cables connecting the antennas to their associated signal processing electronics. The range measurements used in this thesis research contain an open–loop correction for the cable propagation delay as provided by the CIRIS II software [11].

The following discussion develops the range measurement model used in the Advanced CIRIS Kalman filter. As before, let the E–frame position vectors of the jth transponder antenna, the interrogator antenna, and INS be denoted by $\boldsymbol{P}^E_{T_j}$, $\boldsymbol{P}^E_A$, and $\boldsymbol{P}^E_I$, respectively. The line–of–sight range, R_j, between the two antennas is a nonlinear function of these position coordinates. The functional form of this Euclidian distance is

$$R_j = \left|\boldsymbol{P}^E_{T_j} - \boldsymbol{P}^E_A\right| \equiv \sqrt{(X_{T_j} - X_A)^2 + (Y_{T_j} - Y_A)^2 + (Z_{T_j} - Z_A)^2} \tag{3.19}$$

This nonlinear dependence dictates the use of the extended Kalman filter measurement update procedure, Equations (2.46) through (2.49).

The range measurement function, h_r, is defined as the sum of the true line–of–sight range, R_j, the range dependent atmospheric propagation delay, $R_j\,\delta A_{T_j}$, and the interrogator range measurement calibration bias, δE_{rc}. This measurement is corrupted by a random measurement noise, v_r. In accordance with Equation (2.42), the assumed model of the range measurement provided by transponder T_j is

$$\mathrm{z}_r(t_i) = \mathrm{h}_r[t_i, \mathbf{x}(t_i)] + v_r(t_i) \tag{3.20}$$

where

$$\mathrm{h}_r[t_i, \mathbf{x}(t_i)] = R_j[\mathbf{x}(t_i)] + R_j[\mathbf{x}(t_i)]\,\delta A_{T_j}(t_i) + \delta E_{rc}(t_i) \tag{3.21}$$

The range measurement noise is modeled as a zero–mean white noise. The range measurement noise strength is specified in Appendix A, Table A.14.

The corresponding range observation vector, $\mathbf{H}_r$, is calculated using Equation (2.49). The result, shown here as the bracketed terms in the product $\mathbf{H}_r\widehat{\delta\mathbf{x}}$, is

$$\begin{aligned}
\mathbf{H}_r[t_i; \widehat{\mathbf{x}}(t_i^-)]\widehat{\delta\mathbf{x}}(t_i) \;=\; & +\left[\frac{\widehat{X}_{T_j} - \widehat{X}_A}{\widehat{R}_j}\right]\widehat{\delta X}_{T_j} + \left[\frac{\widehat{Y}_{T_j} - \widehat{Y}_A}{\widehat{R}_j}\right]\widehat{\delta Y}_{T_j} + \left[\frac{\widehat{Z}_{T_j} - \widehat{Z}_A}{\widehat{R}_j}\right]\widehat{\delta Z}_{T_j} \\
& - \left[\frac{\widehat{X}_{T_j} - \widehat{X}_A}{\widehat{R}_j}\right]\widehat{\delta X}_I - \left[\frac{\widehat{Y}_{T_j} - \widehat{Y}_A}{\widehat{R}_j}\right]\widehat{\delta Y}_I - \left[\frac{\widehat{Z}_{T_j} - \widehat{Z}_A}{\widehat{R}_j}\right]\widehat{\delta Z}_I \\
& + \left[\widehat{R}_j\right]\widehat{\delta A}_{T_j} + [1]\,\widehat{\delta E}_{rc}
\end{aligned} \tag{3.22}$$

Note that h_r and $\mathbf{H}_r$ both depend on the E–frame position of the interrogator antenna,

but the position error states estimated by the filter are for the INS position. The antenna location must be calculated using the filter estimates of the INS position error and knowledge of the offset (lever arm) between the INS platform and the interrogator antenna. The offset vector is constant in the B-frame but depends on the aircraft position and orientation in the E-frame. This offset vector, $\boldsymbol{M}$, is illustrated in Figure 3.2. It is defined by

$$[\boldsymbol{M}]^B = \begin{bmatrix} X_M \\ Y_M \\ Z_M \end{bmatrix}^B \equiv \begin{bmatrix} X_I \\ Y_I \\ Z_I \end{bmatrix}^B - \begin{bmatrix} X_A \\ Y_A \\ Z_A \end{bmatrix}^B \tag{3.23}$$

$$[\boldsymbol{M}]^E = \boldsymbol{C}_N^E \boldsymbol{C}_B^N [\boldsymbol{M}]^B = \begin{bmatrix} X_M(L,\lambda,h,\psi,\theta,\phi) \\ Y_M(L,\lambda,h,\psi,\theta,\phi) \\ Z_M(L,\lambda,h,\psi,\theta,\phi) \end{bmatrix}^E \tag{3.24}$$

The E-frame position coordinates of the interrogator antenna are estimated by the filter software as

$$\begin{bmatrix} \hat{X}_A \\ \hat{Y}_A \\ \hat{Z}_A \end{bmatrix}^E = \begin{bmatrix} \hat{X}_I \\ \hat{Y}_I \\ \hat{Z}_I \end{bmatrix}^E + \begin{bmatrix} \hat{X}_M \\ \hat{Y}_M \\ \hat{Z}_M \end{bmatrix}^E \tag{3.25}$$

The E-frame components of $\widehat{\boldsymbol{M}}$ are determined from Equation (3.24) using filter estimates of the six arguments.

3.4.2 Range-Rate Measurement The range-rate measurement is also provided by the Cubic RRS. Ideally, the range-rate is simply the magnitude of the relative velocity between the transponder and interrogator antennas. This (E-frame) range-rate is found by differentiating Equation (3.19). The result is

$$\begin{aligned} \dot{R}_j[\mathbf{x}(t),t] \equiv \frac{dR_j}{dt} &= \frac{\partial R_j}{\partial X_{T_j}}\frac{dX_{T_j}}{dt} + \frac{\partial R_j}{\partial X_A}\frac{dX_A}{dt} + \cdots + \frac{\partial R_j}{\partial Z_{T_j}}\frac{dZ_{T_j}}{dt} + \frac{\partial R_j}{\partial Z_A}\frac{dZ_A}{dt} \\ &= -\left(\frac{X_{T_j}-X_A}{R_j}\right)\dot{X}_A - \left(\frac{Y_{T_j}-Y_A}{R_j}\right)\dot{Y}_A - \left(\frac{Z_{T_j}-Z_A}{R_j}\right)\dot{Z}_A \end{aligned} \tag{3.26}$$

The range–rate measurement function, $\mathrm{h}_{\dot{r}}$, is defined as the sum of the true line–of–sight range–rate, $\dot{R}_j$, and the interrogator range–rate measurement calibration bias, $\delta E_{\dot{r}c}$. This measurement is corrupted by a random measurement noise, $v_{\dot{r}}$. In accordance with Equation (2.42), the assumed model of the range–rate measurement provided by transponder T_j is

$$\mathrm{z}_{\dot{r}}(t_i) = \mathrm{h}_{\dot{r}}[t_i, \mathbf{x}(t_i)] + v_{\dot{r}}(t_i) \tag{3.27}$$

where

$$\mathrm{h}_{\dot{r}}[t_i, \mathbf{x}(t_i)] = \dot{R}_j[\mathbf{x}(t_i)] + \delta E_{\dot{r}c}(t_i) \tag{3.28}$$

The range–rate measurement noise is modeled as a zero–mean white noise. The range–rate measurement noise strength is specified in Appendix A, Table A.14.

The corresponding range–rate observation vector, $\mathbf{H}_{\dot{r}}$, is calculated using Equation (2.49). The result, shown here as the bracketed terms in the product $\mathbf{H}_{\dot{r}}\widehat{\delta\mathbf{x}}$, is

$$\begin{aligned}
&\mathbf{H}_{\dot{r}}[t_i; \hat{\mathbf{x}}(t_i^-)]\,\widehat{\delta\mathbf{x}}(t_i) = \\
&\quad - \left[\frac{(\hat{X}_{T_j} - \hat{X}_A)^2\hat{\dot{X}}_A + (\hat{X}_{T_j} - \hat{X}_A)(\hat{Y}_{T_j} - \hat{Y}_A)\hat{\dot{Y}}_A + (\hat{X}_{T_j} - \hat{X}_A)(\hat{Z}_{T_j} - \hat{Z}_A)\hat{\dot{Z}}_A - \hat{R}^2_{T_j}\hat{\dot{X}}_A}{\hat{R}^3_{T_j}}\right]\widehat{\delta X}_I \\
&\quad - \left[\frac{(\hat{Y}_{T_j} - \hat{Y}_A)(\hat{X}_{T_j} - \hat{X}_A)\hat{\dot{X}}_A + (\hat{Y}_{T_j} - \hat{Y}_A)^2\hat{\dot{Y}}_A + (\hat{Y}_{T_j} - \hat{Y}_A)(\hat{Z}_{T_j} - \hat{Z}_A)\hat{\dot{Z}}_A - \hat{R}^2_{T_j}\hat{\dot{Y}}_A}{\hat{R}^3_{T_j}}\right]\widehat{\delta Y}_I \\
&\quad - \left[\frac{(\hat{Z}_{T_j} - \hat{Z}_A)(\hat{X}_{T_j} - \hat{X}_A)\hat{\dot{X}}_A + (\hat{Z}_{T_j} - \hat{Z}_A)(\hat{Y}_{T_j} - \hat{Y}_A)\hat{\dot{Y}}_A + (\hat{Z}_{T_j} - \hat{Z}_A)^2\hat{\dot{Z}}_A - \hat{R}^2_{T_j}\hat{\dot{Z}}_A}{\hat{R}^3_{T_j}}\right]\widehat{\delta Z}_I \\
&\quad - \left[\frac{\hat{X}_{T_j} - \hat{X}_A}{R_{T_j}}\right]\widehat{\delta\dot{X}}_I - \left[\frac{\hat{Y}_{T_j} - \hat{Y}_A}{R_{T_j}}\right]\widehat{\delta\dot{Y}}_I - \left[\frac{\hat{Z}_{T_j} - \hat{Z}_A}{R_{T_j}}\right]\widehat{\delta\dot{Z}}_I + [1]\,\widehat{\delta E}_{\dot{r}c}
\end{aligned} \tag{3.29}$$

Note that $\mathrm{h}_{\dot{r}}$ and $\mathbf{H}_{\dot{r}}$ depend on the E–frame velocity of the interrogator antenna as well as well as its E–frame position, but the velocity error states estimated by the filter are for the INS velocity. The E–frame velocity of the interrogator antenna is found as follows. Since

$$[\boldsymbol{P}_A]^E = [\boldsymbol{P}_I]^E + [\boldsymbol{M}]^E \tag{3.30}$$

then

$$[\dot{\boldsymbol{P}}_A]^E = [\dot{\boldsymbol{P}}_I]^E + [\dot{\boldsymbol{M}}]^E \tag{3.31}$$

Also, since

$$[M]^E = C_B^E [M]^B \tag{3.32}$$

then

$$[\dot{M}]^E = \dot{C}_B^E [M]^B \tag{3.33}$$

because the B–frame representation of M is constant. The derivative of C_B^E is found using the identity

$$\dot{C}_B^E = C_B^E \Omega_{EB}^B \tag{3.34}$$

where Ω_{EB}^B is the skew–symmetric form of ω_{EB}^B, the E–frame to B–frame angular velocity vector expressed in the B–frame. Because ω_{EB}^B is not directly available, it is calculated as

$$\begin{aligned} \omega_{EB}^B &= \omega_{EN}^B + \omega_{NB}^B \\ &= C_N^B \omega_{EN}^N + \omega_{NB}^B \end{aligned} \tag{3.35}$$

where ω_{EN}^N is computed from the latitude and longitude rates and ω_{NB}^B is computed from the heading, pitch, and roll rates. These two angular rotation rate vectors are

$$\omega_{EN}^N = \begin{bmatrix} \dot{\lambda}\cos L \\ \dot{L} \\ \dot{\lambda}\sin L \end{bmatrix} \qquad \omega_{NB}^B = \begin{bmatrix} \dot{\phi} + \dot{\psi}\sin\theta \\ \dot{\theta}\cos\phi - \dot{\psi}\sin\phi\sin\theta \\ \dot{\theta}\sin\phi + \dot{\psi}\cos\phi\cos\theta \end{bmatrix}$$

When these equations are combined, and filter estimates used for all needed matrix elements, the filter estimate of the E–frame velocity of the interrogator antenna is computed as

$$[\hat{\dot{P}}_A]^E \equiv \begin{bmatrix} \hat{\dot{X}}_A \\ \hat{\dot{Y}}_A \\ \hat{\dot{Z}}_A \end{bmatrix}^E = \begin{bmatrix} \hat{\dot{X}}_I \\ \hat{\dot{Y}}_I \\ \hat{\dot{Z}}_I \end{bmatrix}^E + \hat{C}_B^E \hat{\Omega}_{EB}^B \begin{bmatrix} X_M \\ Y_M \\ Z_M \end{bmatrix}^B \tag{3.36}$$

3.4.3 Barometric Altitude Measurement The altitude measurement is provided by the barometric altimeter. Ideally, this measurement indicates the true altitude of the INS. In order to account for limitations inherent in the estimation of altitude based on barometric pressure and other error sources, the baro–altimeter output is modeled as the sum of the true altitude, a constant bias error, a time correlated bias error, a scale factor error, and a random measurement noise, v_{h_b}. In order to eliminate the true altitude from the

measurement and isolate the altitude errors, the measurement presented to the filter is the difference between the barometric altitude and the INS indicated altitude. In accordance with Equation (2.42), the assumed model of the barometric altitude measurement is

$$z_{h_b}(t_i) = \mathrm{h}_{h_b}[t_i, \mathbf{x}(t_i)] + v_{h_b}(t_i) \tag{3.37}$$

where

$$\begin{aligned}
\mathrm{h}_{h_b}[t_i, \mathbf{x}(t_i)] &= \widehat{h}_b(t_i) - \widehat{h}(t_i) && (3.38)\\
&= [h(t_i) + \delta h_b(t_i)] - [h(t_i) + \delta h(t_i)] && (3.39)\\
&= \delta h_b(t_i) - \delta h(t_i) && (3.40)\\
&= [\delta h_{b1}(t_i) + \delta h_{b2} + h(t_i)\delta h_{b3}] - \delta h && (3.41)
\end{aligned}$$

The corresponding barometric altitude observation vector, $\mathbf{H}_{h_b}$, is calculated using Equation (2.49). The result, shown here as the bracketed terms in the product $\mathbf{H}_{h_b}\widehat{\delta\mathbf{x}}$, is

$$\mathbf{H}_{h_b}[t_i; \widehat{\mathbf{x}}(t_i^-)]\widehat{\delta\mathbf{x}}(t_i) = [1]\,\widehat{\delta h}_{b1}(t_i) + [1]\,\widehat{\delta h}_{b2}(t_i) + \left[\widehat{h}(t_i)\right]\widehat{\delta h}_{b3}(t_i) - [1]\,\delta h \tag{3.42}$$

The baro–altimeter output is sampled within 50 milliseconds of each transponder interrogation. Since it is not separately time–tagged, the baro–altimeter measurement is assumed to have the same time–tag as the associated transponder range measurement [11].

3.5 Summary

This chapter presents the structure of the 70–state, MSOFE–based, extended Kalman filter that is the current incarnation of the Advanced CIRIS filter. The (error) state vector is partitioned into four error–state groups. The first group contains 13 INS position, velocity, platform tilt, and vertical channel aiding errors; the second group contains 12 gyro and accelerometer errors; the third group contains three baro–altimeter errors; and the fourth group contains 42 transponder calibration, position, and atmospheric propagation errors. Of the 42 transponder states, 40 represent ten sets of the four error states associated with each of up to ten different transponders. The filter software permits the use of up to twenty different transponders through a state time–sharing procedure.

The filter uses three types of measurements. Range and range–rate measurements are provided by the transponders, while barometric altitude is provided by a baro–altimeter. The range and range–rate measurement functions are nonlinear. Because of the position offset between the CIRIS antenna and the INS, a procedure for compensating for "lever–arm" effects is developed.

IV. 70-State Filter Evaluation: Ground Test Data

This chapter describes the use of the 70-state filter to process real measurements collected during a slow speed ground test.

4.1 Data Collection Procedure

The data used in this analysis was collected on 21 July 1989, during a series of tests at the 6585th Test Group's Rocket Sled Test Track. The CIRIS LN-39 INS, transponder interrogator, baro-altimeter, and HP-1000 computer were placed in a Recovery Support Vehicle (RSV). Starting from a known point on the track, the RSV was driven either north or south along the track while the CIRIS equipment recorded the INS data, barometric-altitude, and the transponder measurements. At the same time, the position of the RSV was recorded by an independent track data acquisition system (TDAS). Both sets of recorded data were referenced to a common IRIG time base. The starting configuration is illustrated in Figure 4.1. The offset dimensions between the INS and the TDAS sensor are listed in Table 4.1.

This series of tests involved six different transponders. The transponder ID's and their corresponding WGS 84 coordinates are listed in Table 4.2. The position of these transponders relative to the track is shown in Figure 4.2. The initial INS alignment location and starting point for each of the northward runs was 32° 53′ 6.5648″ N latitude, 106° 8′ 59.6288″ W longitude, and 3991 feet altitude.

The measurements from transponder 211 are not used because the range measurements contain an anomalous oscillation with a period of about 90 seconds. The oscillation is not apparent in the associated range-rate measurements. The oscillation is shown in Figure 4.3. This plot is obtained by using the TDAS indicated positions to calculate the expected range to the transponder at each point along the track. The expected range is then subtracted from the measured range at each measurement time. The bias shown in Figure 4.3 is most likely due the combination of an error in the surveyed position of transponder 211 and the offset between the CIRIS antenna and the TDAS sensor. However the oscillation cannot be explained at this time. The oscillation is not present when the

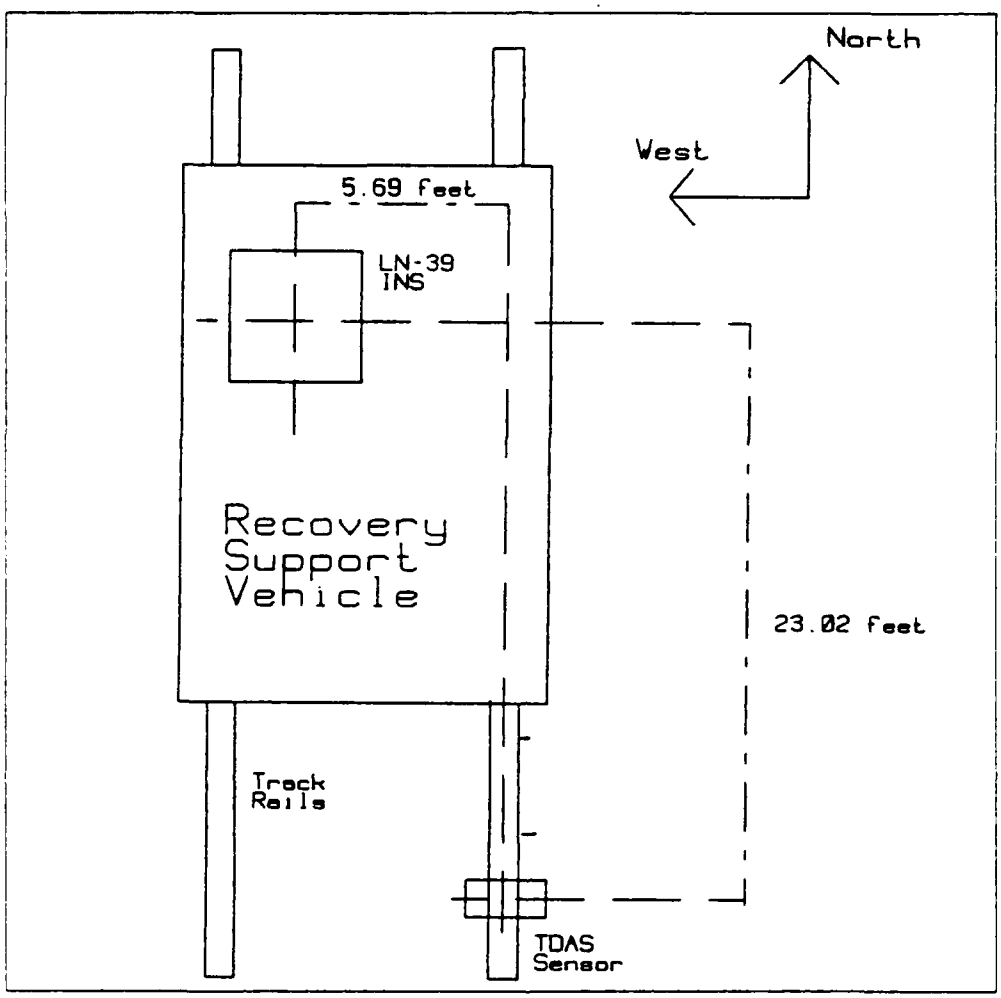

Figure 4.1. Equipment Configuration for the CIRIS/RSV Tests

Table 4.1. INS Position Offsets

South–to–North Run	North–to–South Run
23.02 *ft* North	-23.02 *ft* North
-5.69 *ft* East	2.60 *ft* East
4.75 *ft* Above	4.75 *ft* Above

Table 4.2. Transponder Locations for the CIRIS/RSV Tests

Transponder ID	Latitude	Longitude	Altitude
005	33° 01′ 36.1472″	−106° 08′ 20.7404″	4339 *ft*
102	32° 55′ 58.5986″	−106° 08′ 50.3339″	4074 *ft*
181	33° 44′ 58.035″	−106° 22′ 14.630″	7932 *ft*
211	33° 17′ 55.999″	−106° 31′ 44.311″	8842 *ft*
212	32° 47′ 16.418″	−105° 49′ 15.474″	9202 *ft*
216	32° 42′ 12.235″	−106° 07′ 38.907″	4481 *ft*

RSV is stationary. In two other track runs in which the RSV speed was purposely varied, the frequency of the oscillation increased in proportion to the speed. In computer runs where the transponder 211 range measurements are processed by the filter, the oscillation appears in plots of the measurement residuals and in both the transponder and INS position error states. An example of the oscillating residuals is shown in Figure 4.4. The dashed lines in this plot are the filter calculated residual $\pm 1\sigma$ bounds. The oscillation is also apparent in the transponder 211 range measurement residuals of the current CIRIS II filter.

4.2 70-State Filter Performance

The original objective for the use of this ground test data was to validate the structure of the filter's error model by tuning certain filter parameters (noise strengths and correlation times) so that the measurement residuals appeared "correct." That is, the residuals should appear white, zero-mean, with variance as predicted by the filter. If this is achieved, and the filter's error model is sufficiently valid, then the differences between the position and velocity estimates of the filter and TDAS should be minimized. The justification for this statement is that TDAS-indicated position and velocity are derived from precisely surveyed points along the length of the track; therefore, they are best available measurements of the true quantities. However the poor geometry of the transponders relative to the RSV trajectory partially frustrated this goal by limiting the observability of important error states. The lack of observability made the filter error state estimates very sensitive to the initial error state covariance estimates. The parameters considered

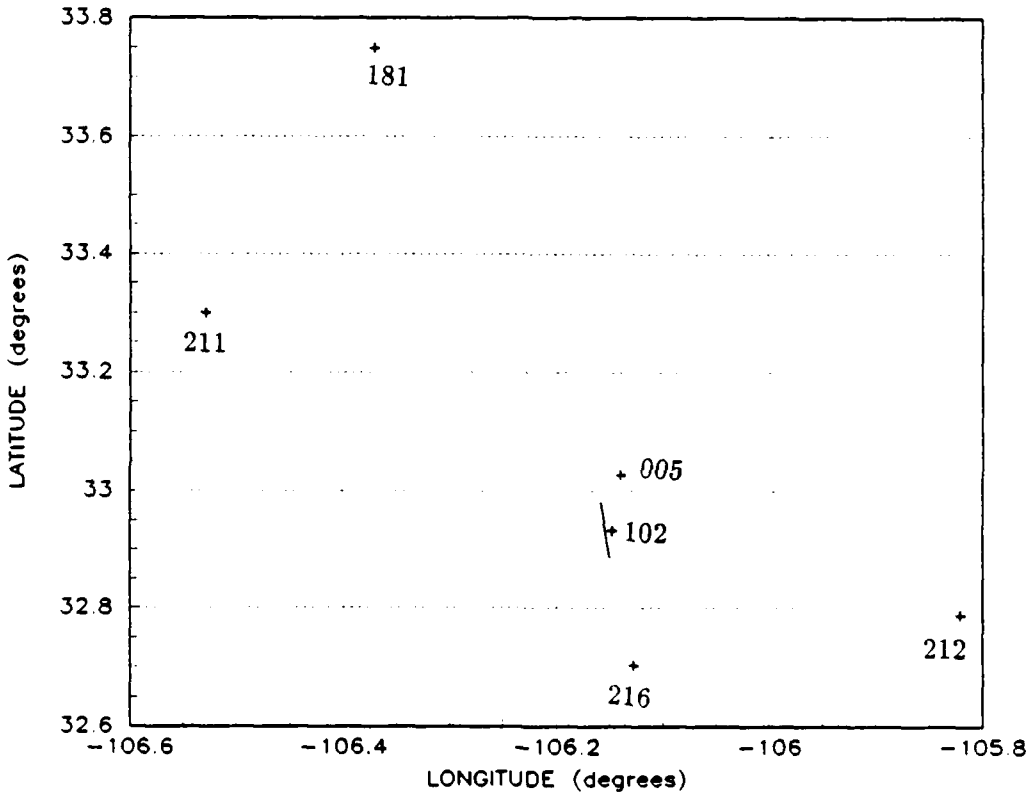

Figure 4.2. Transponder Locations Relative to the Test Track

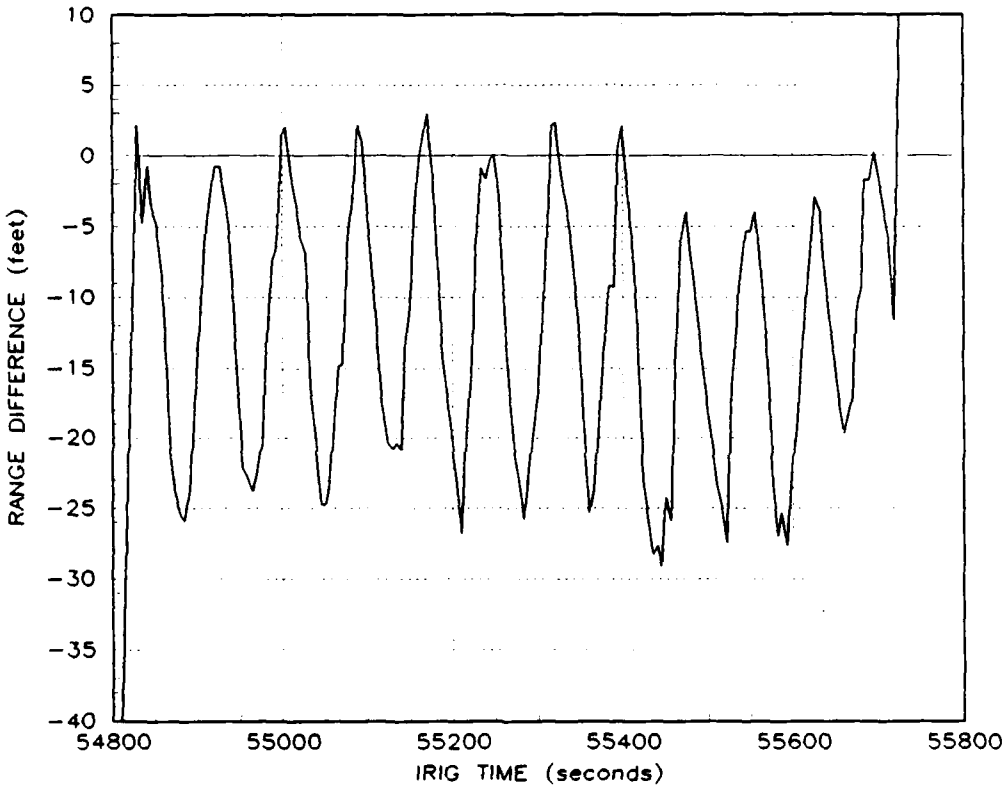

Figure 4.3. Anomalous Range Measurement Oscillation, Transponder 211

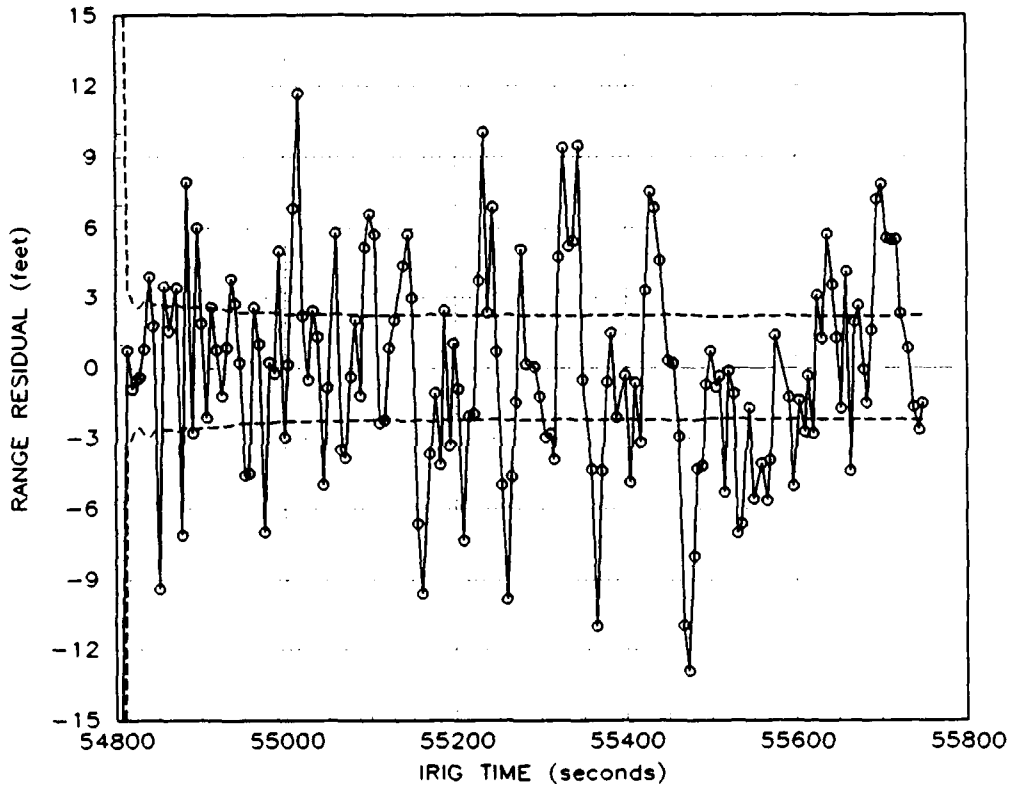

Figure 4.4. Oscillating Range Measurement Residuals, Transponder 211

least well known are: (1) the driving noise strengths the atmospheric propagation delay scale factors, (2) the correlation coefficients for these driving noises for each transponder pair, (3) the correlation times for these driving noises, (4) the driving noise strength for the baro–altimeter correlated noise, and (5) the correlation time for the baro–altimeter correlated noise.

Starting with the intial parameter values described in Appendix A, the 70–state filter was used to process data from three different track runs, two south–to–north and one north–to–south. Different combinations of tuning parameters and initial covariance estimates were tried for the five items mentioned above.

The two sets of estimates are compared at time points corresponding to filter measurement update times. Because the TDAS sampling times did not coincide with the filter measurement update times, the TDAS positions and velocities were interpolated at the filter update times. This interpolation is accomplished using the $MATRIX_X$ cubic spline function. After the interpolation is completed, the filter position estimates are corrected for the offset in the INS position relative to the TDAS sensor.

For the northward run, the position correction was made as follows. A *positive* latitude error means that the filter latitude estimate is too far north. A *positive* longitude error means that the filter longitude estimate is too far east. A *positive* altitude error means that the filter altitude estimate is too far up. The position of the INS relative to the TDAS sensor is shown in Table 4.1. Since the track heading relative to true north is constant throughout the length of the track, these position offsets are also constant. For the northward and southward runs, the appropriate offset quantities were *subtracted* from the filter estimates in order to translate the filter estimates to the TDAS sensor location.

The area where the filter is most sensitive is the baro–altimeter error model. The separation of the baro–altimeter error into three separate error states results in observability problems when, as in this case, the test trajectory is of short duration and involves only negligible altitude changes. When all three states were included in the filter, the sum of the constant and time–correlated biases tended to grow increasingly positive while the scale factor error grew increasingly negative. The result was the sum of the three errors

stayed in the range of 100 to −100 feet while the individual error states were divergent. This situation was corrected by using only one state to model the baro–altimeter error for the ground test data. The scale factor error state was eliminated and the other two error states combined into a first–order Markov error state with a correlation time of 2000 seconds and a driving noise variance of 4 ft^2. The initial variance for this single baro–altimeter error state and for the INS altitude error state were each reduced to 2500 ft^2. Even with the simplified baro–altimeter error model, the filter altitude estimates remain biased relative to the TDAS indicated altitude, as is shown in Figure 4.7.

The filter estimates are also sensitive to the atmospheric propagation delay error model parameters. The filter is most sensitive to the assumed driving noise strength and less sensitive to the assumed correlation time and driving noise correlation coefficient. The assumed driving noise variance is reduced to 4 ft^2 from the value shown in Appendix A. This reduction had a smoothing effect on the INS and transponder position error estimates as well as the atmospheric delay estimates.

The data set discussed here is designated Track Run E. Track Run E started at IRIG time 54826 and ended at IRIG time 55722. This starting time is approximately 50 minutes after the INS was aligned. Appendix B contains the plots of the recorded data. The TDAS position and velocity data for Track Run E is plotted in Figures B.1 and B.2. The LN–39 INS indicated position, velocity, and acceleration for Track Run E are plotted in Figures B.3, B.4, and B.5. The baro–altimeter, transponder range, and transponder range–rate measurements for Track Run E are plotted in Figures B.6 through B.12. The baro–altimeter discretization increment is 2.5 feet. The barometric altitude rate information is synthesized from the barometric altitude data.

The filter's estimates of position and velocity are compared to the TDAS indicated position and velocity in Figures 4.5 through 4.10. All of these plots show the filter estimate *minus* the corresponding TDAS measurements The latitude difference varies between 0.5 and −11.5 feet with the larger magnitudes in the last half of the run. The longitude difference varies between 16.5 and −7.0 feet with the larger magnitudes in the first half of the run. The altitude difference varies between 7.8 and 26.5 feet with the larger magnitudes in the second half of the run. The midpoint of the run is significant because that is when

the RSV passed by transponder 102, at time 55275. This is the only transponder for which the line–of–sight changes significantly during the run. If one assumes the TDAS measurement to be the "truth," then the growth of the latitude and altitude differences after passing the midpoint is the opposite of what is expected while the decrease in the longitude difference is as expected. The north, west, and up velocity differences are all essentially zero–mean. When the RSV is travelling at constant speed, the peak magnitudes of the velocity differences are 0.6 *fps* for the north velocity, 0.3 *fps* for the west velocity, and 1.7 *fps* for the up velocity.

The measurement residuals are shown in Figures 4.11 through 4.21. All residuals are approximately zero–mean. The dashed lines on the residual plots are the expected residual $\pm 1\sigma$ bounds as computed by the filter. Only measurements within a 5σ threshold are accepted by the filter. For the barometric altitude and range–rate measurements, the residuals have a generally "white" appearance and most of the residuals are within the 1σ bounds, indicating slightly over–conservative filter tuning for these two measurement types. For the range measurements, the residuals appear white for some transponders and less so for others. The ratio of the actual residual variance to the expected residual variance also appears to vary significantly among transponders.

The filter's estimates of the transponder position errors and the atmospheric propagation delay, along with the filter estimated standard deviations, are shown in Figures 4.22 through 4.31. The poor geometry of the transponders relative to the track is apparent in the 1σ plots. There is essentially no observability of the transponder vertical position errors. This is because the altitude of the RSV increases only 30 feet during the run, thus keeping the line–of–sight elevation angles for all transponders under 5°. The effect of passing by transponder 102 is apparent in most of the standard deviation plots; this is where the 1σ values decrease most rapidly.

The magnitudes of the estimated position errors remain resonable values throughout the run, remaining under 7.5 feet. Some of the position error estimates appear to converge on a relatively steady value in the second half of the run while others continue to vary. Of particular interest is the spike in the estimated west position error for transponder 102. This spike seems to be correlated with spikes in the estimated position errors of the

other transponders, particularly transponders 005 and 212. These rapid variations indicate the filter's redistribution of the measurement residual error during the period where it is gaining the most information about the actual position errors for transponder 102.

The magnitudes of the estimated atmospheric propagation delays, after scaling for range, correspond to linear range errors between 2.5 feet and −2.5 feet. Although the true value of the propagation delay must always be positive, the negative estimates are possible for two reasons. The first is the inability of the filter to distinguish between the atmospheric delay and the interrogator range calibration bias within the short duration of the run. The second is the possibility of error in the open loop correction for propagation delay made by the CIRIS interrogator. The 1σ plots for the atmospheric delay error states appear to be converging to steady values.

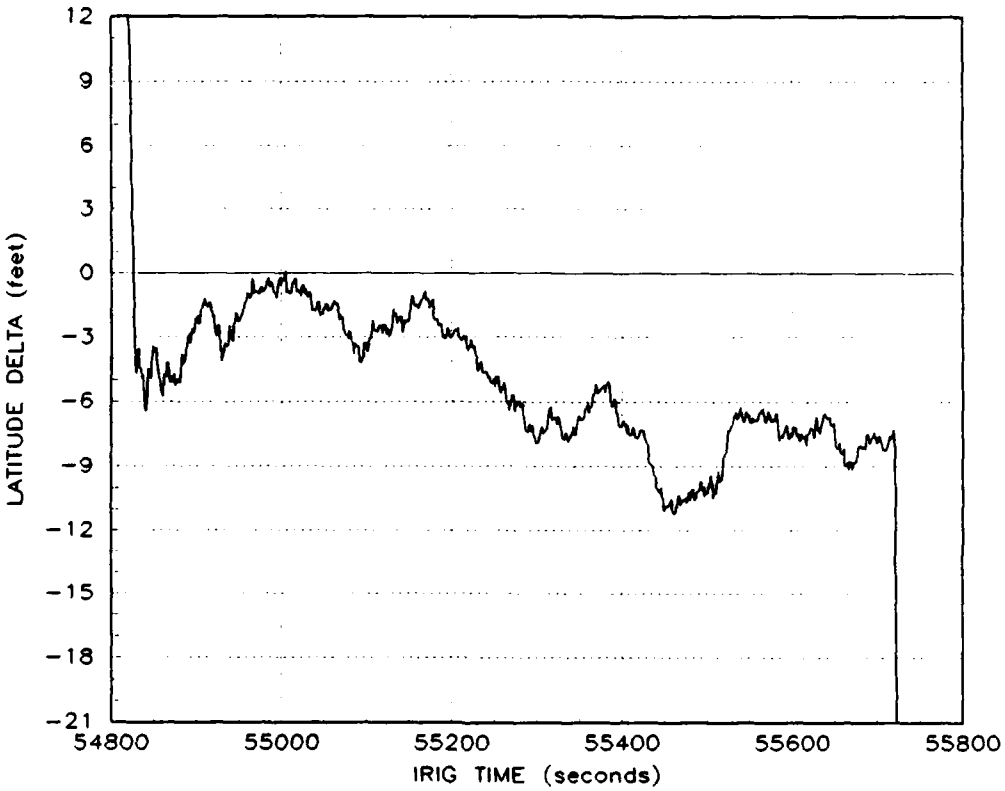

Figure 4.5. Latitude Difference, Track Run E

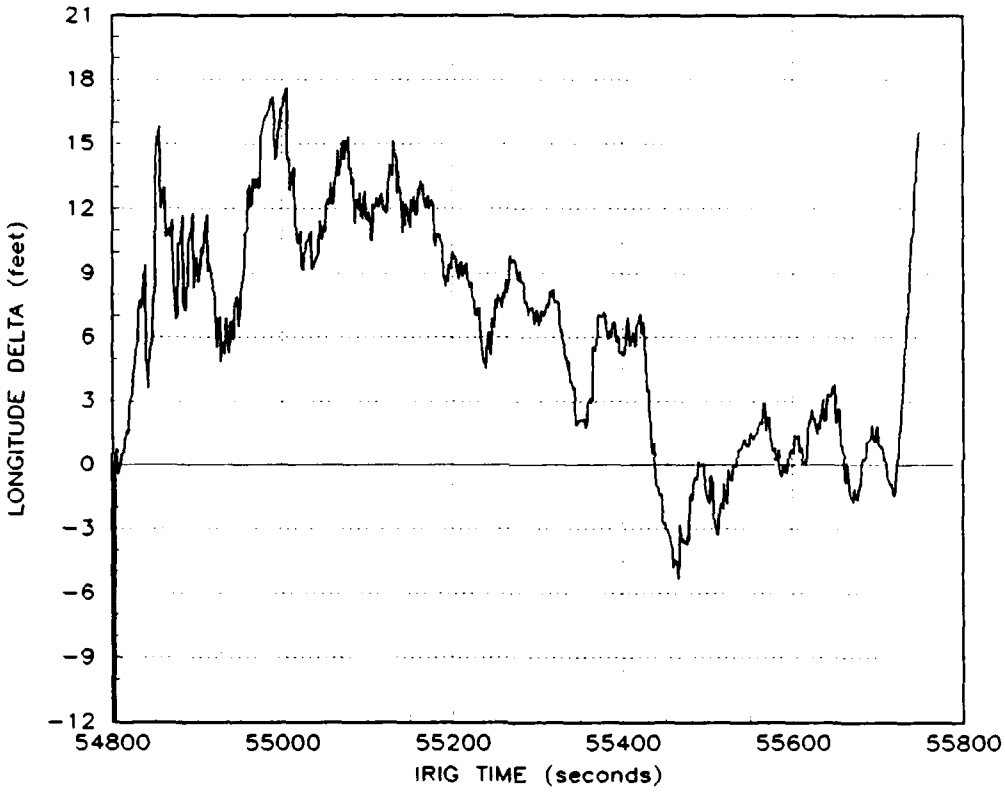

Figure 4.6. Longitude Difference, Track Run E

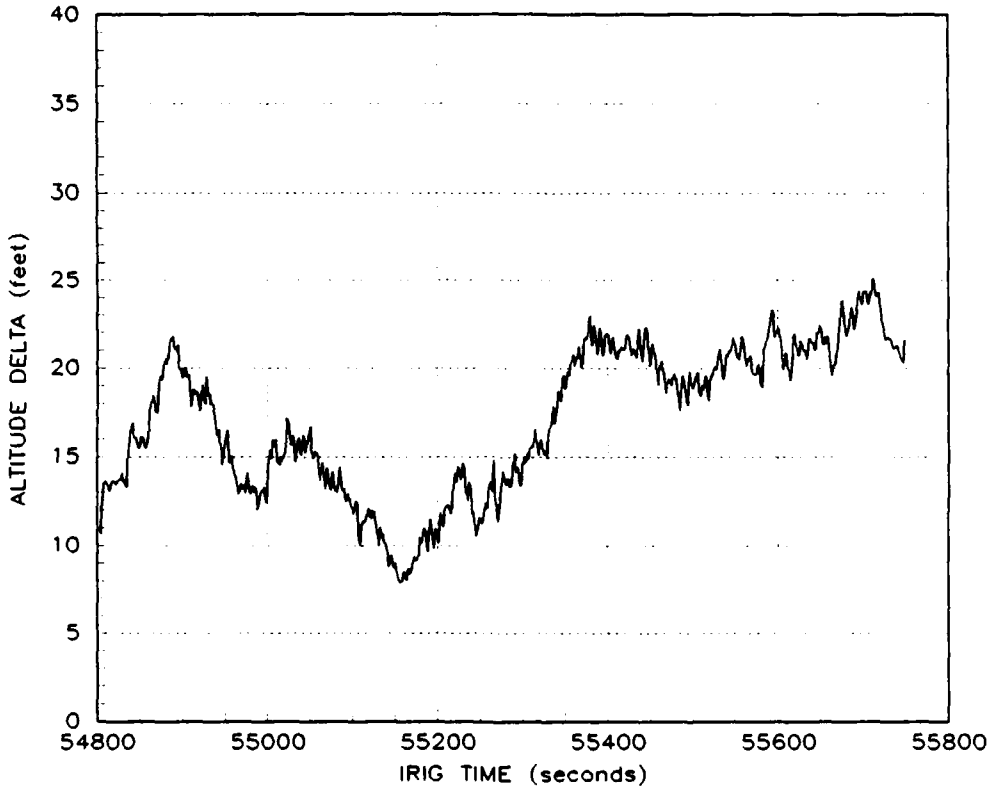

Figure 4.7. Altitude Difference, Track Run E

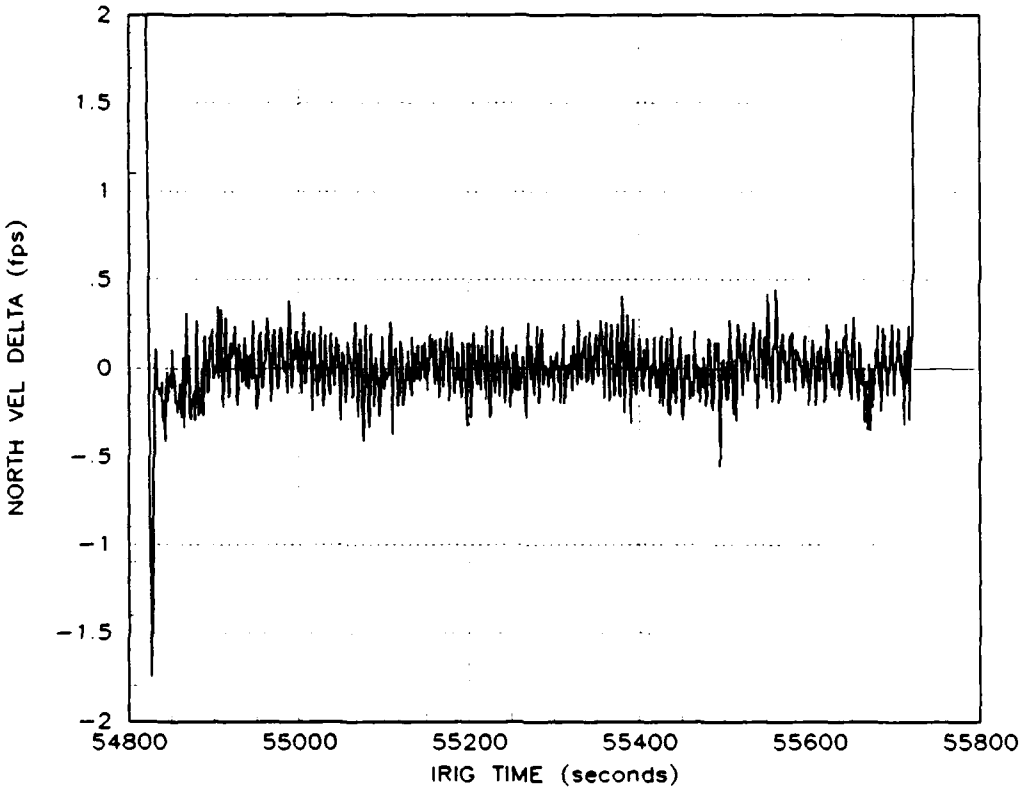

Figure 4.8. North Velocity Difference, Track Run E

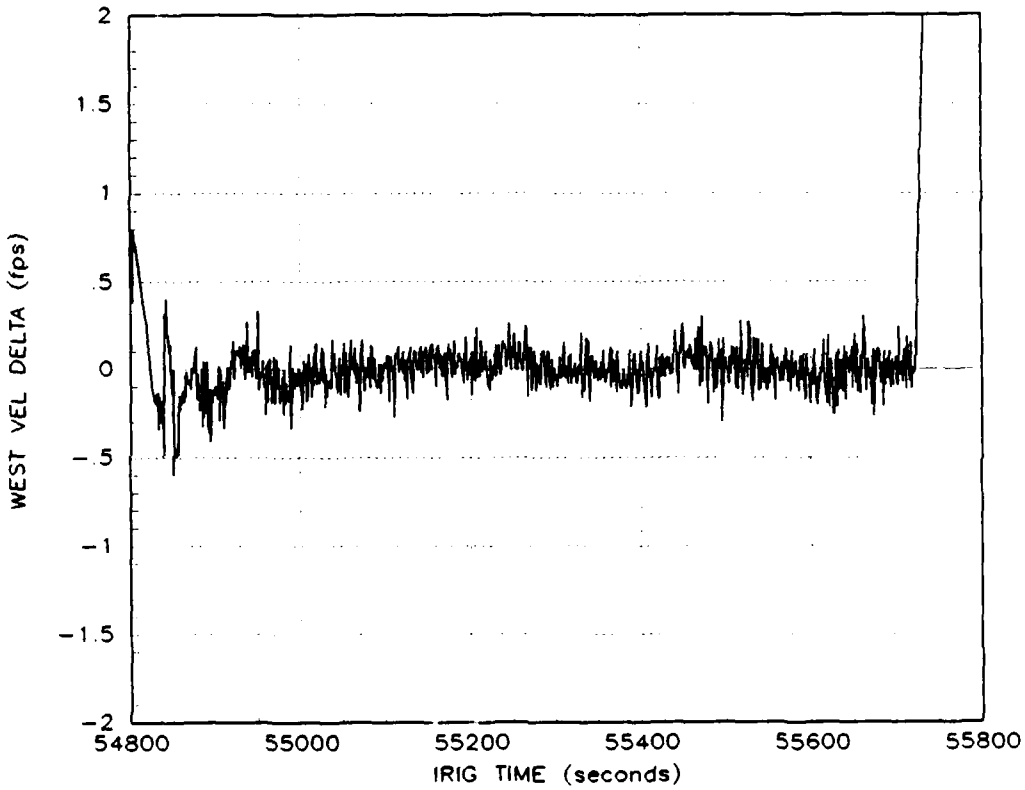

Figure 4.9. West Velocity Difference, Track Run E

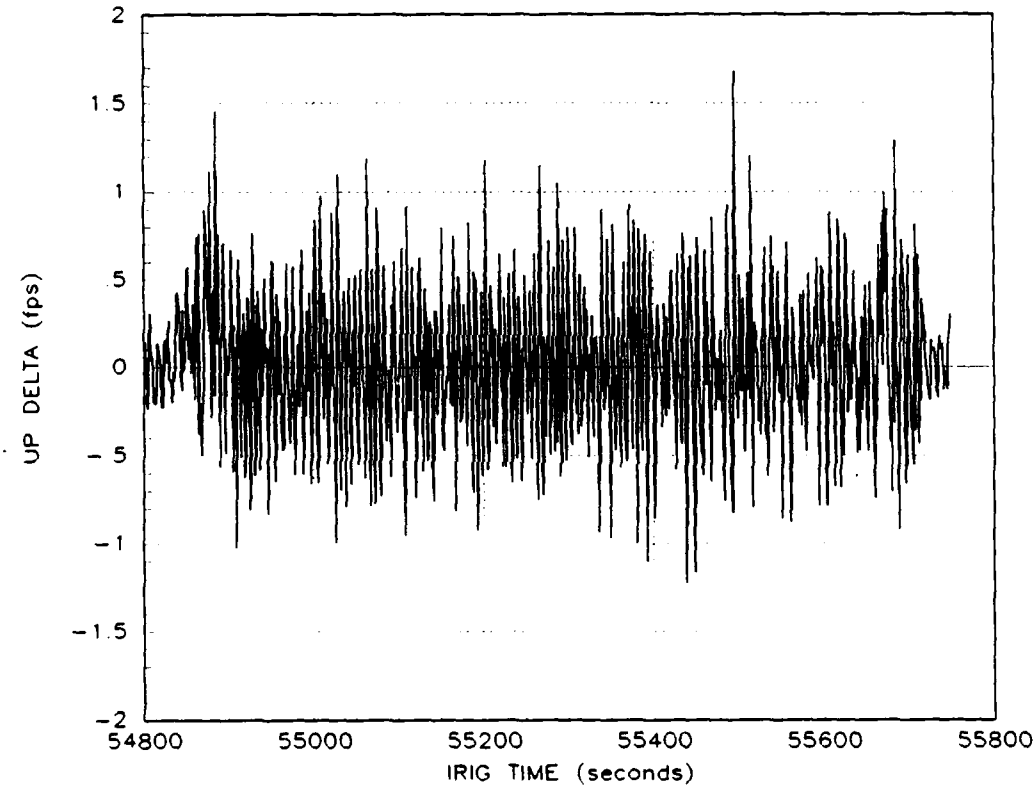

Figure 4.10. Vertical Velocity Difference, Track Run E

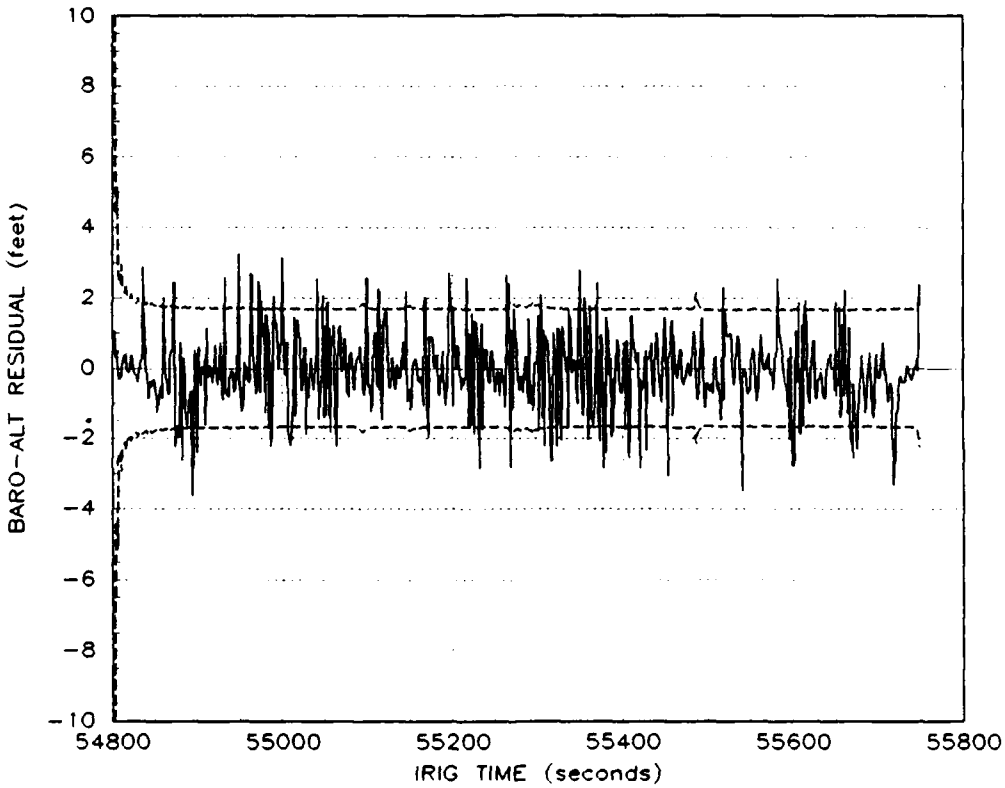

Figure 4.11. Baro-Altitude Residuals, Track Run E

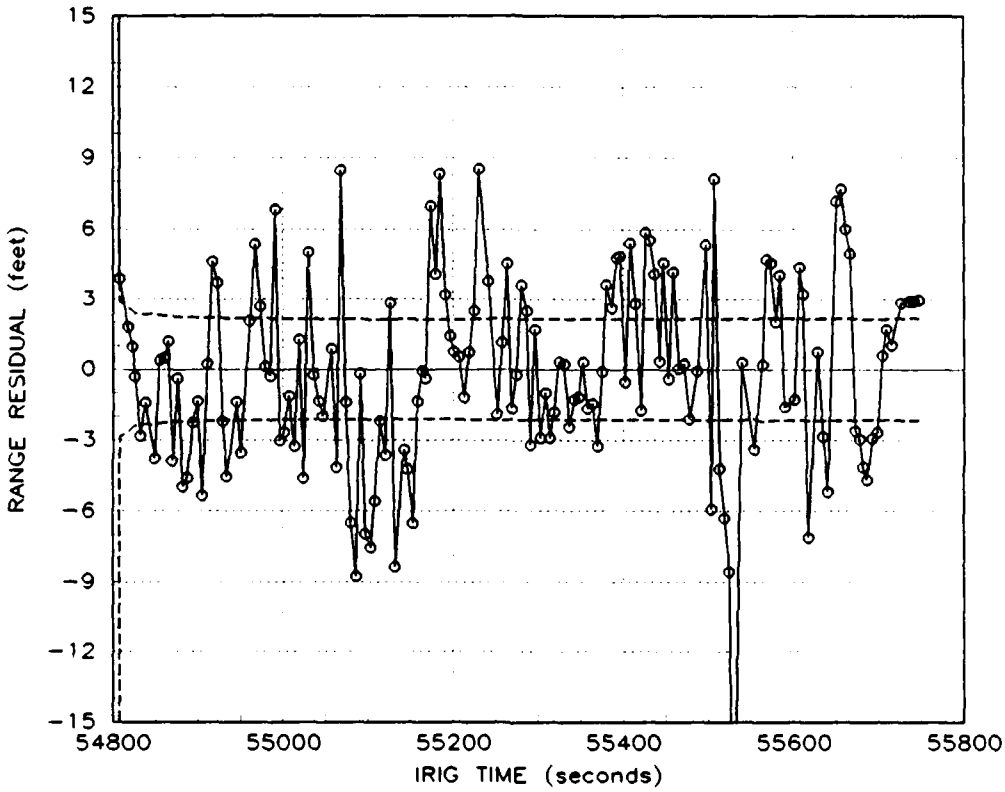

Figure 4.12. Transponder 005 Range Residuals, Track Run E

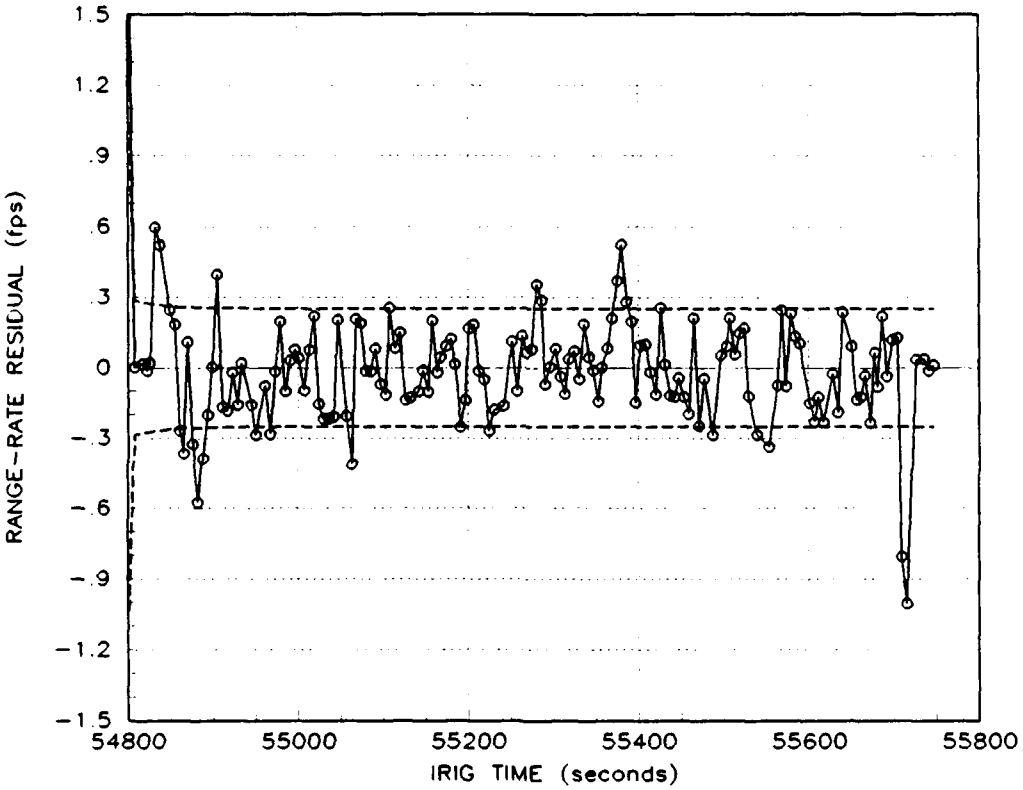

Figure 4.13. Transponder 005 Range–Rate Residuals, Track Run E

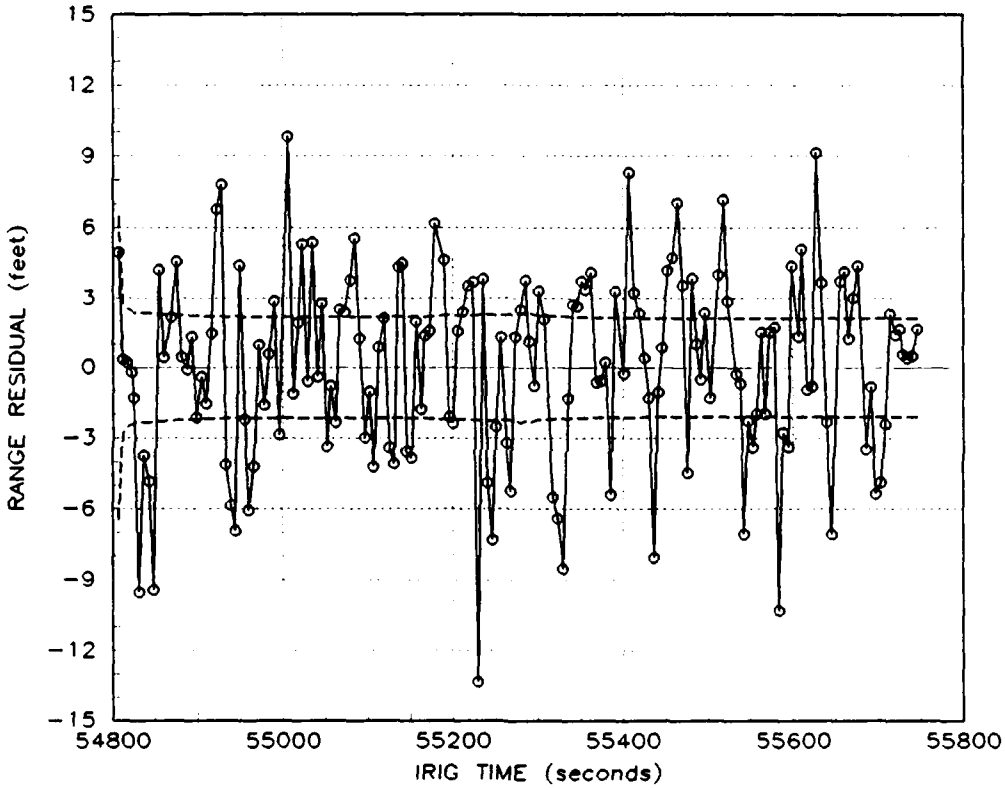

Figure 4.14. Transponder 102 Range Residuals, Track Run E

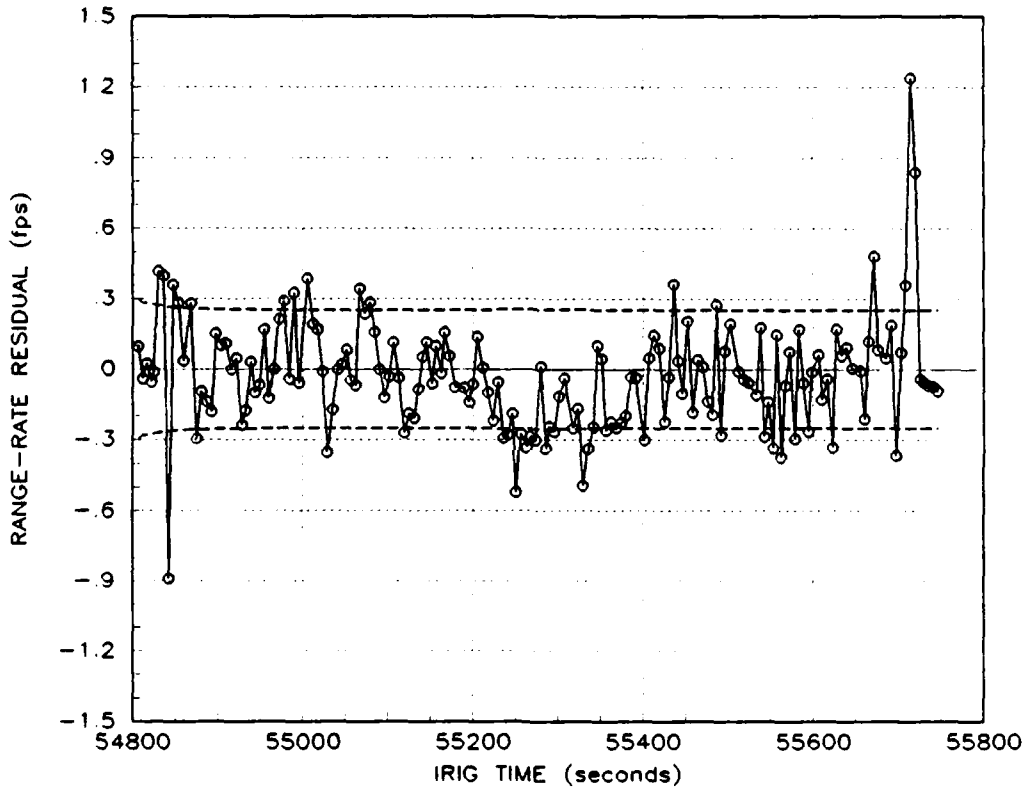

Figure 4.15. Transponder 102 Range–Rate Residuals, Track Run E

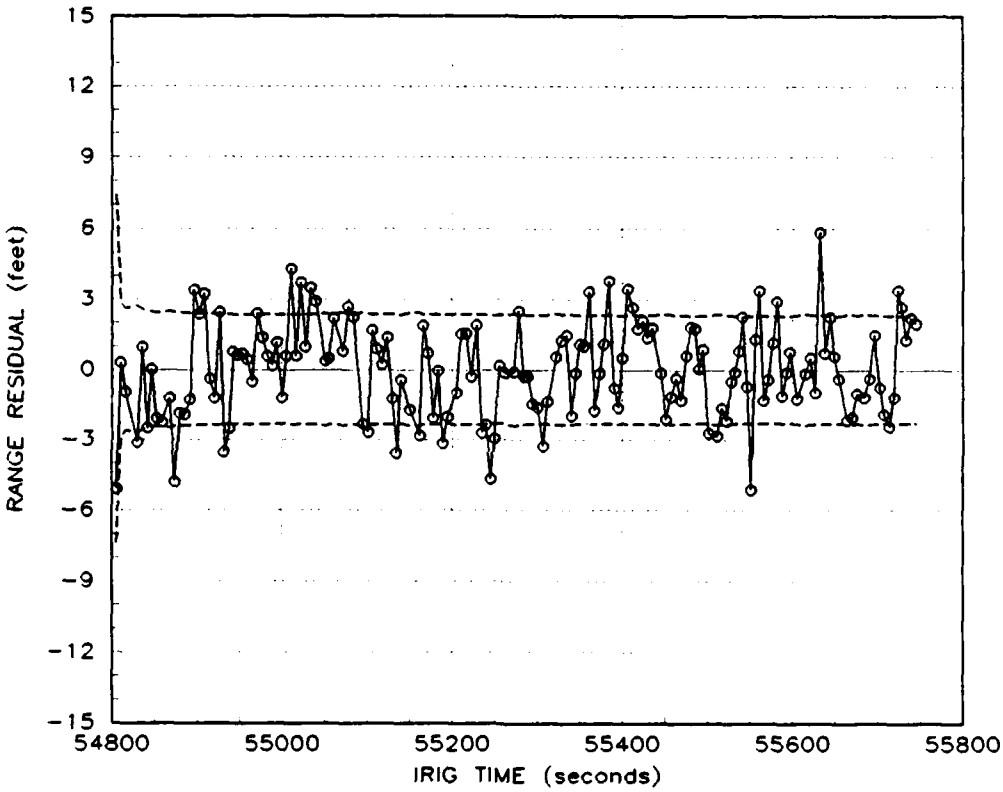

Figure 4.16. Transponder 181 Range Residuals, Track Run E

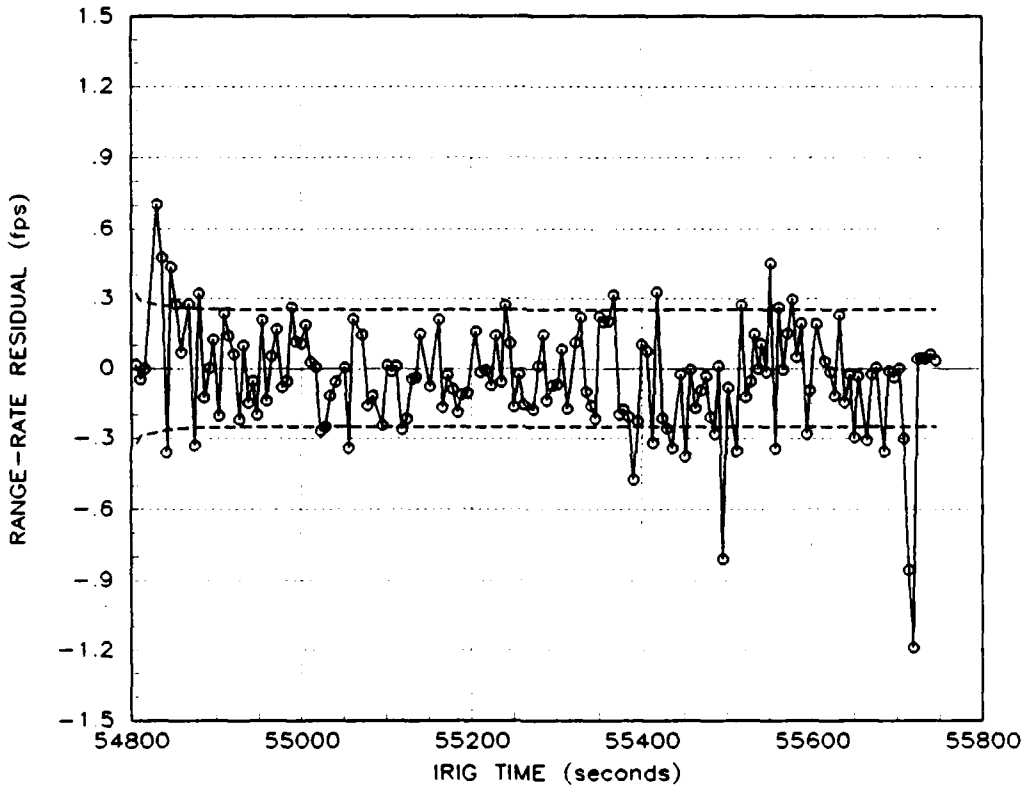

Figure 4.17. Transponder 181 Range–Rate Residuals, Track Run E

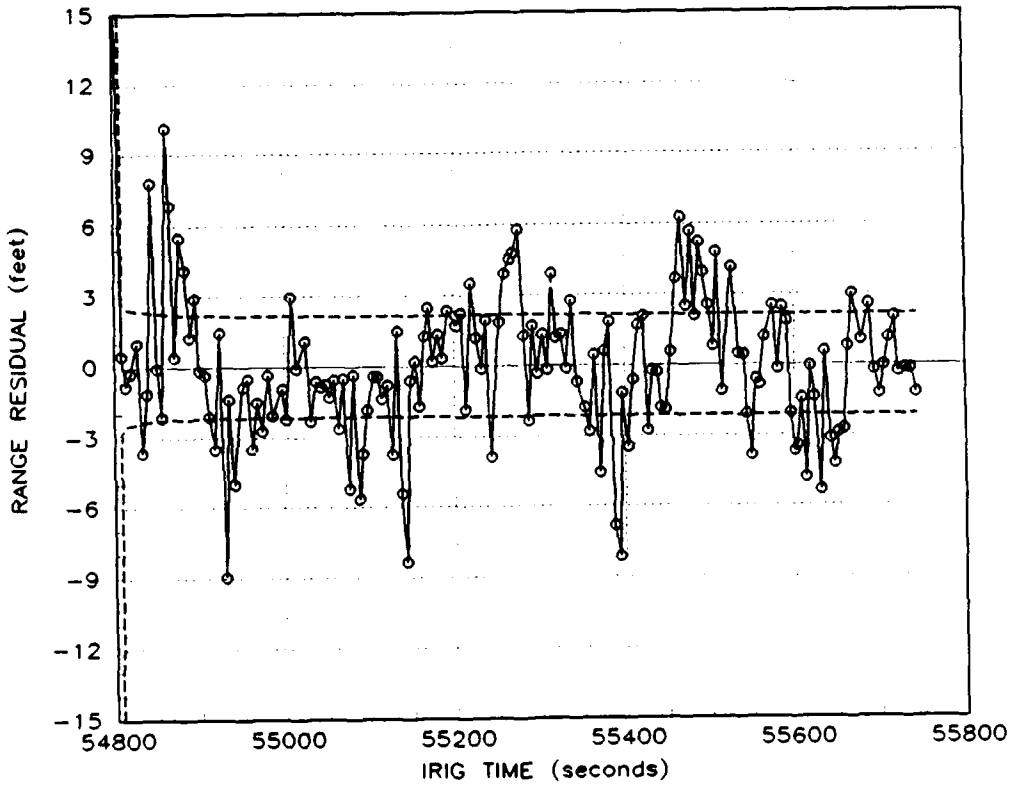

Figure 4.18. Transponder 212 Range Residuals, Track Run E

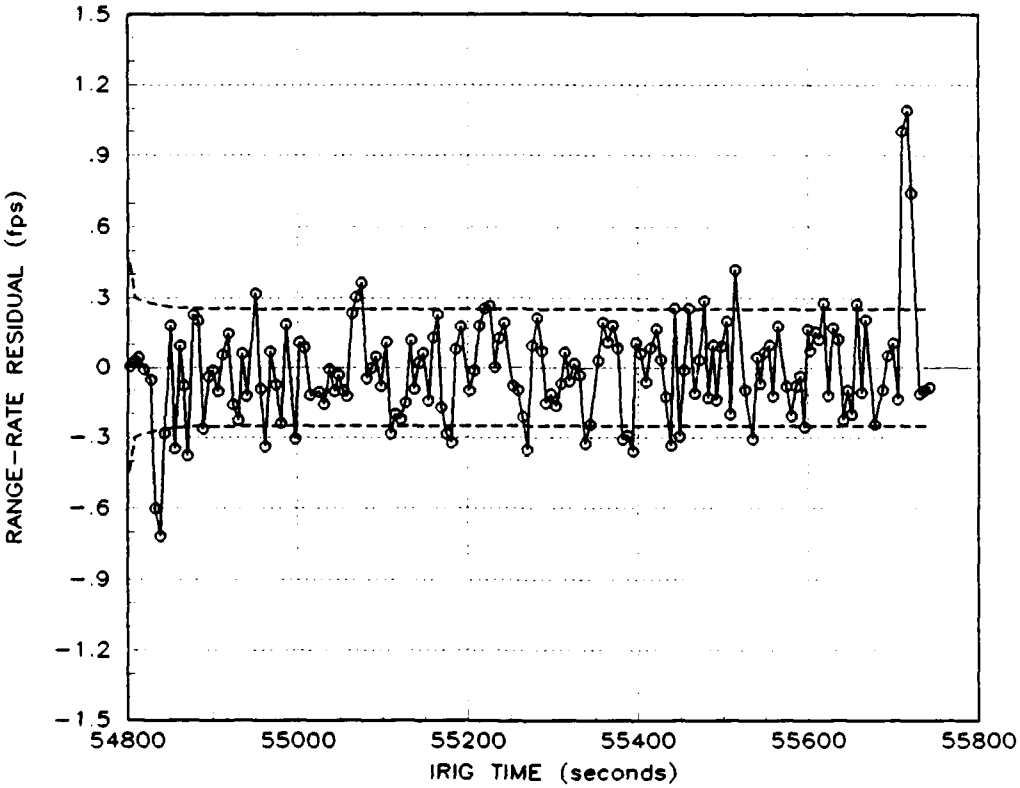

Figure 4.19. Transponder 212 Range–Rate Residuals, Track Run E

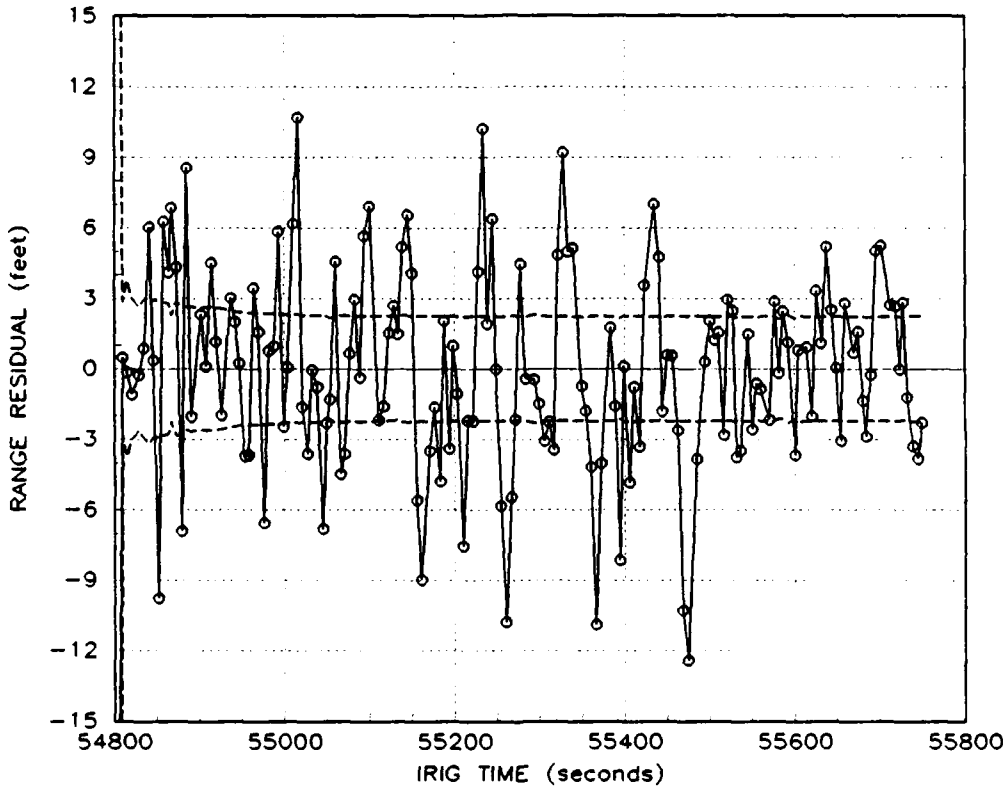

Figure 4.20. Transponder 216 Range Residuals, Track Run E

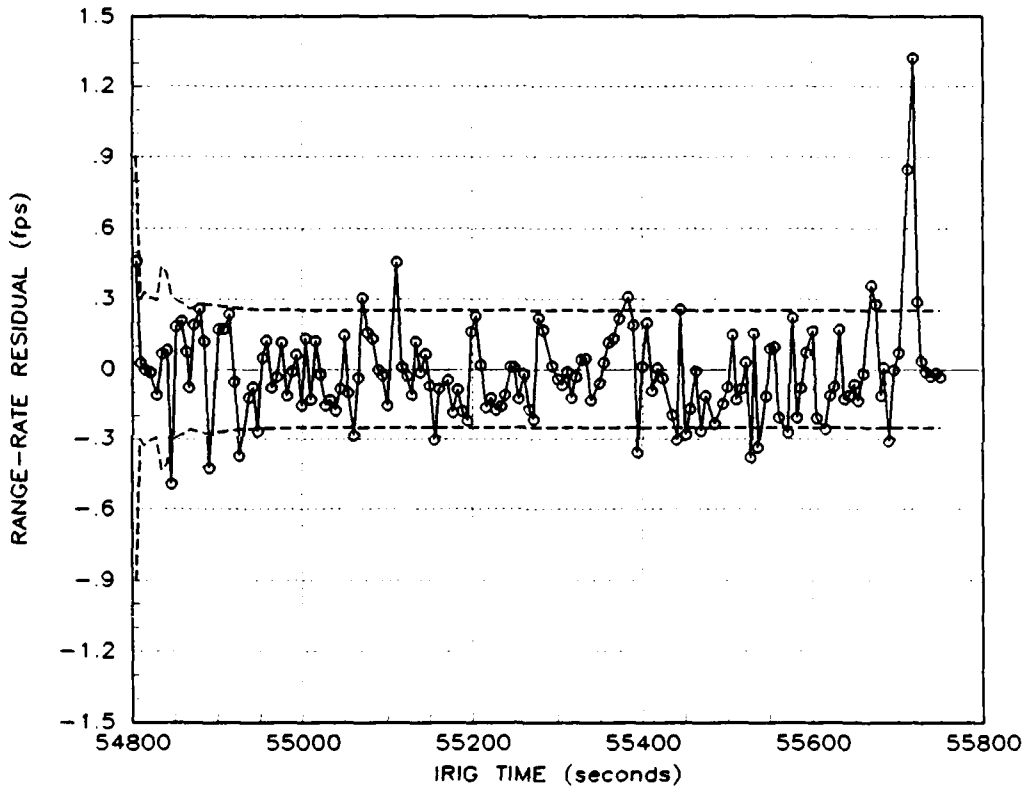

Figure 4.21. Transponder 216 Range–Rate Residuals, Track Run E

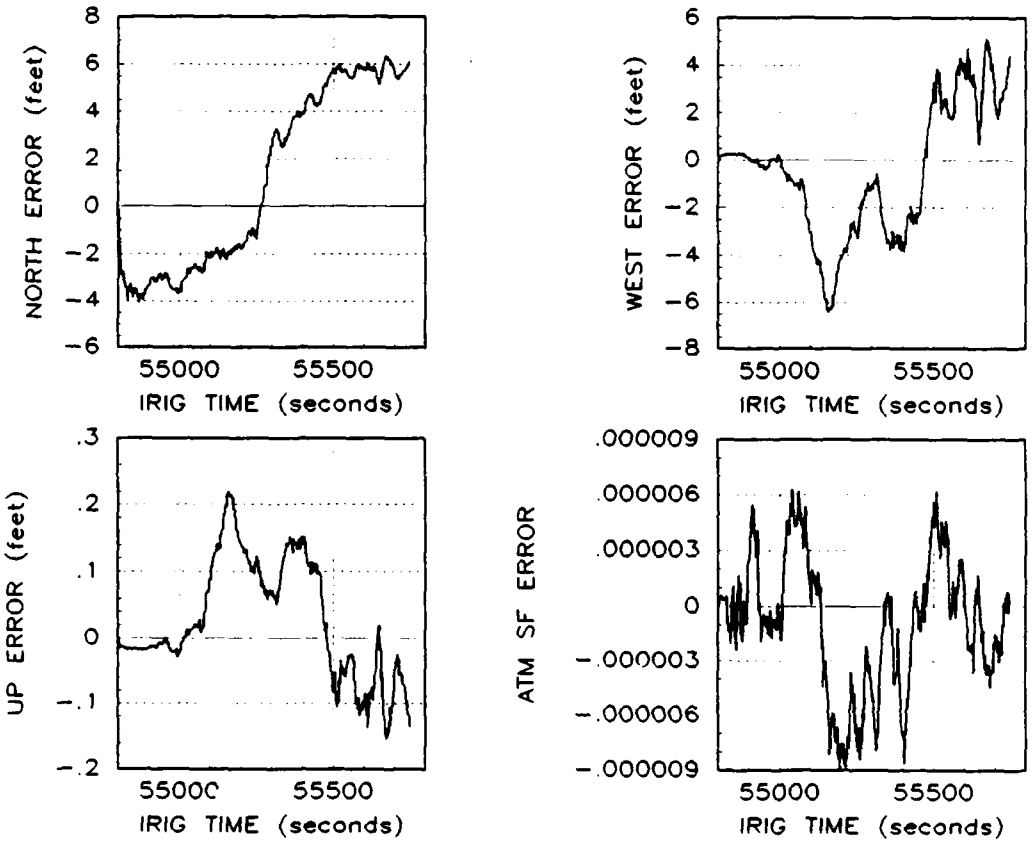

Figure 4.22. Estimated Position Error, Trans 005, Track Run E

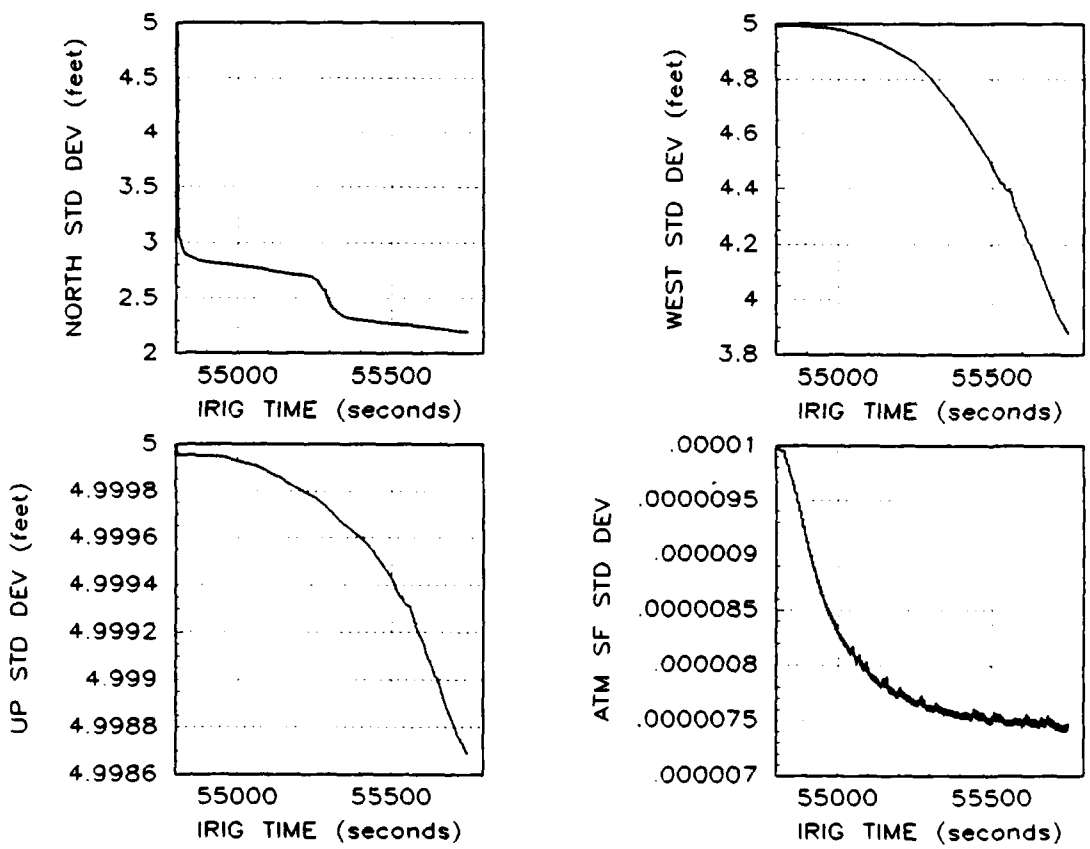

Figure 4.23. Estimated Position Std Dev, Trans 005, Track Run E

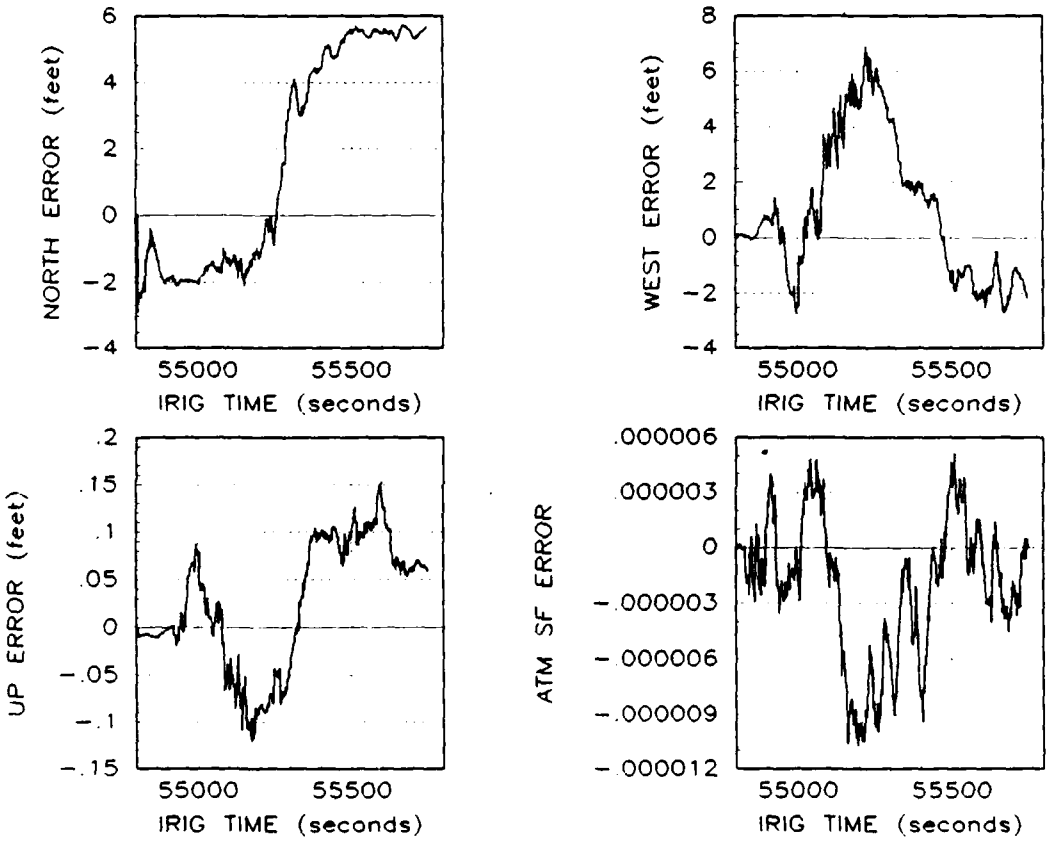

Figure 4.24. Estimated Position Error, Trans 102, Track Run E

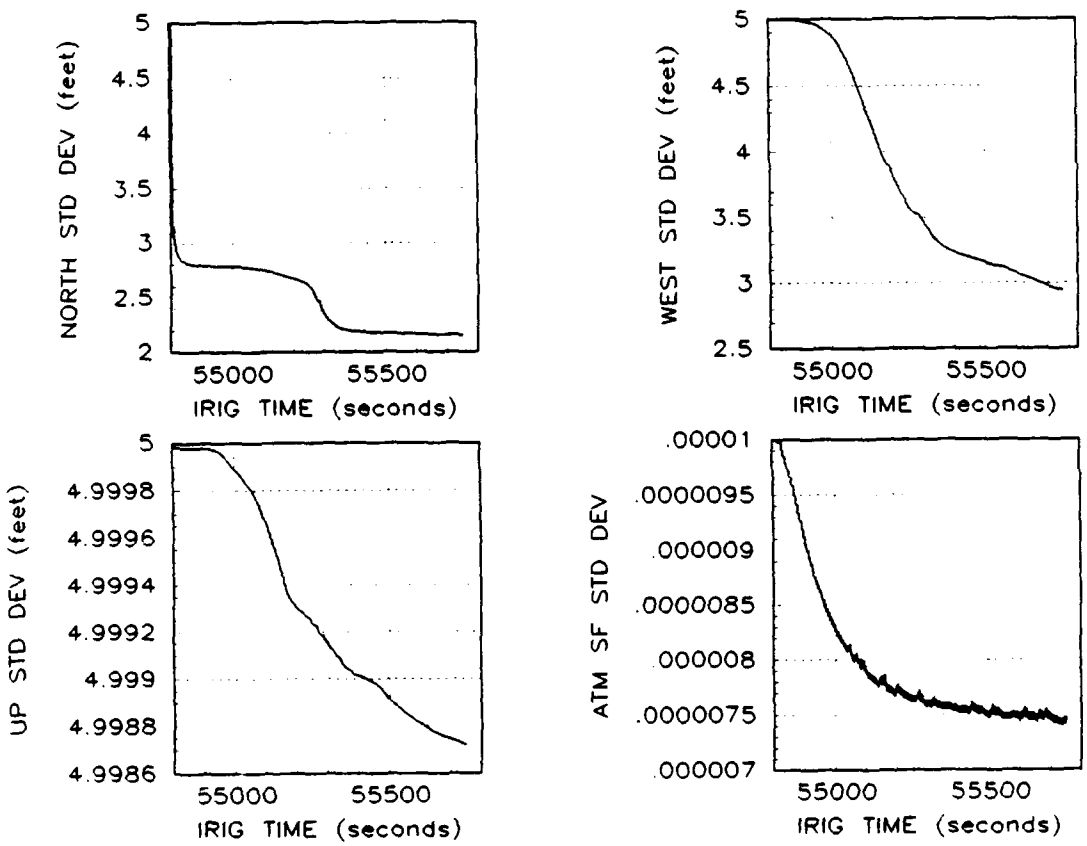

Figure 4.25. Estimated Position Std Dev, Trans 102, Track Run E

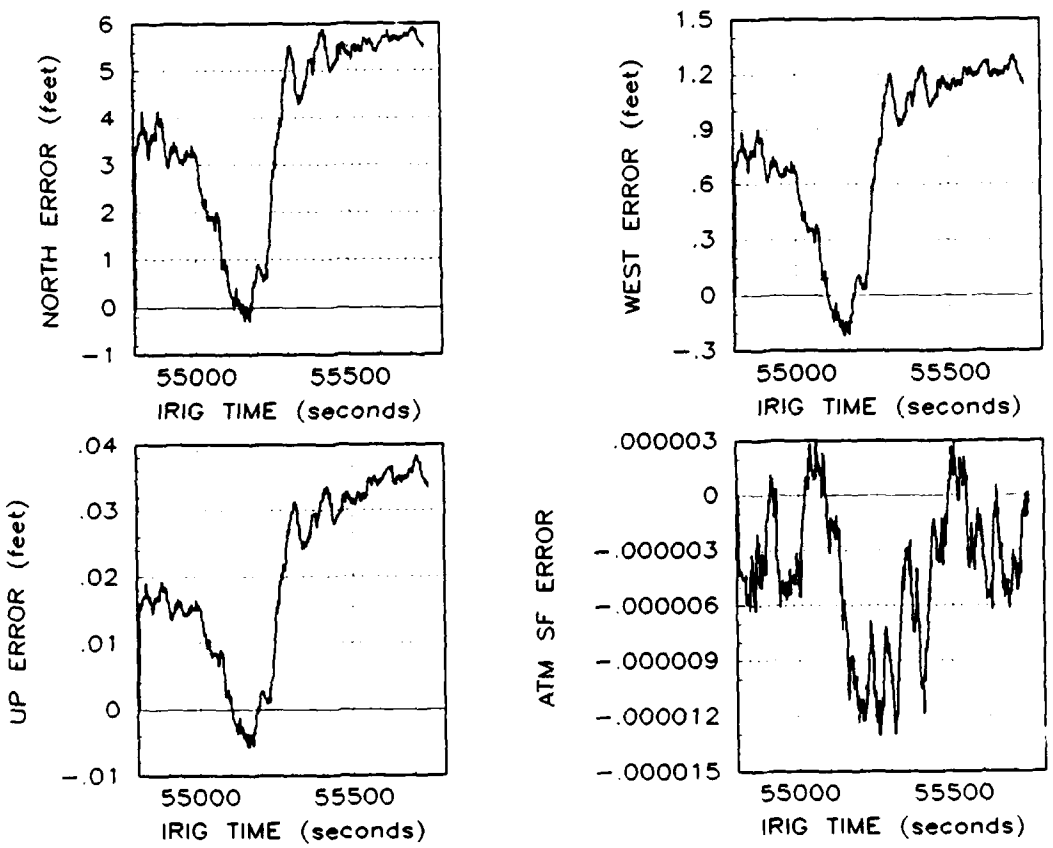

Figure 4.26. Estimated Position Error, Trans 181, Track Run E

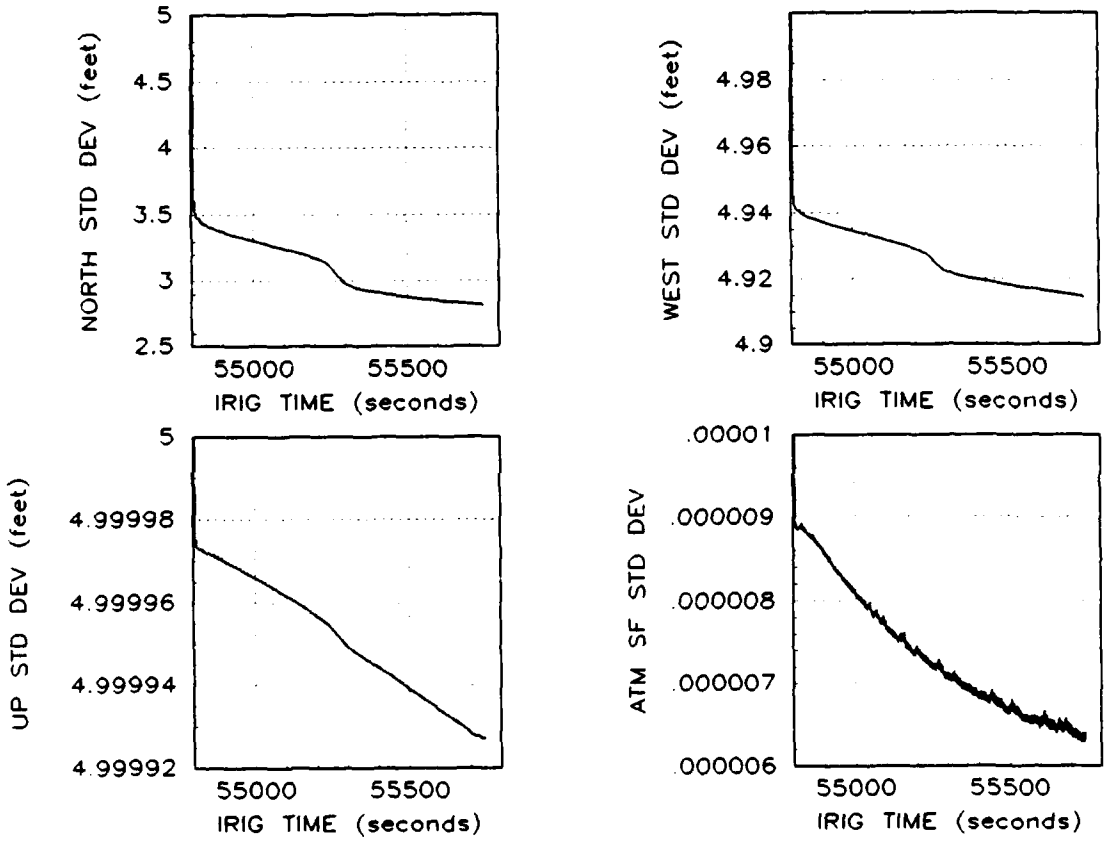

Figure 4.27. Estimated Position Std Dev, Trans 181, Track Run E

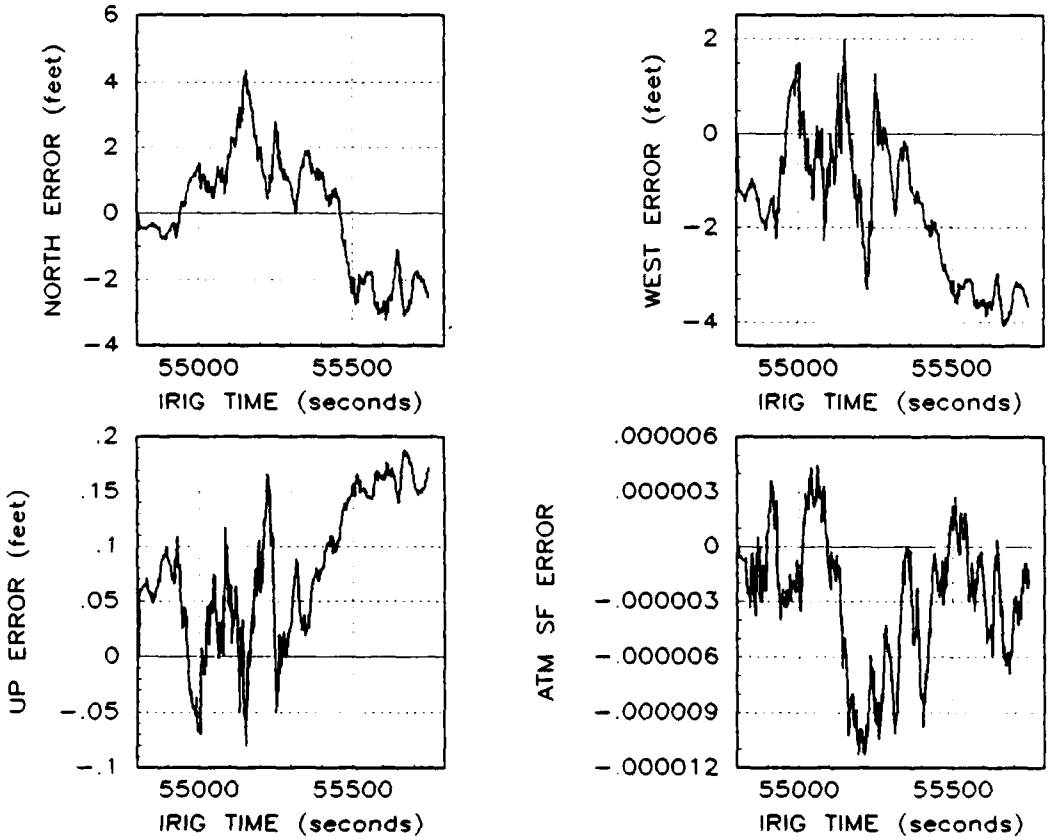

Figure 4.28. Estimated Position Error, Trans 212, Track Run E

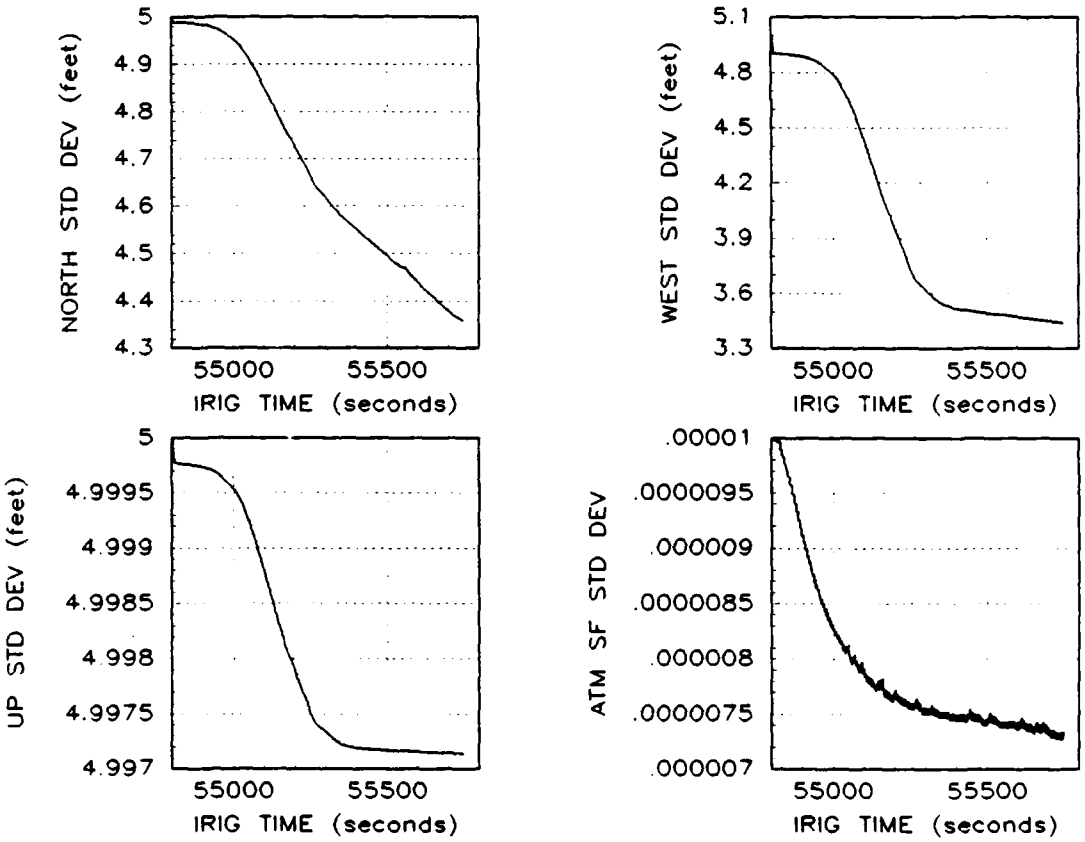

Figure 4.29. Estimated Position Std Dev, Trans 212, Track Run E

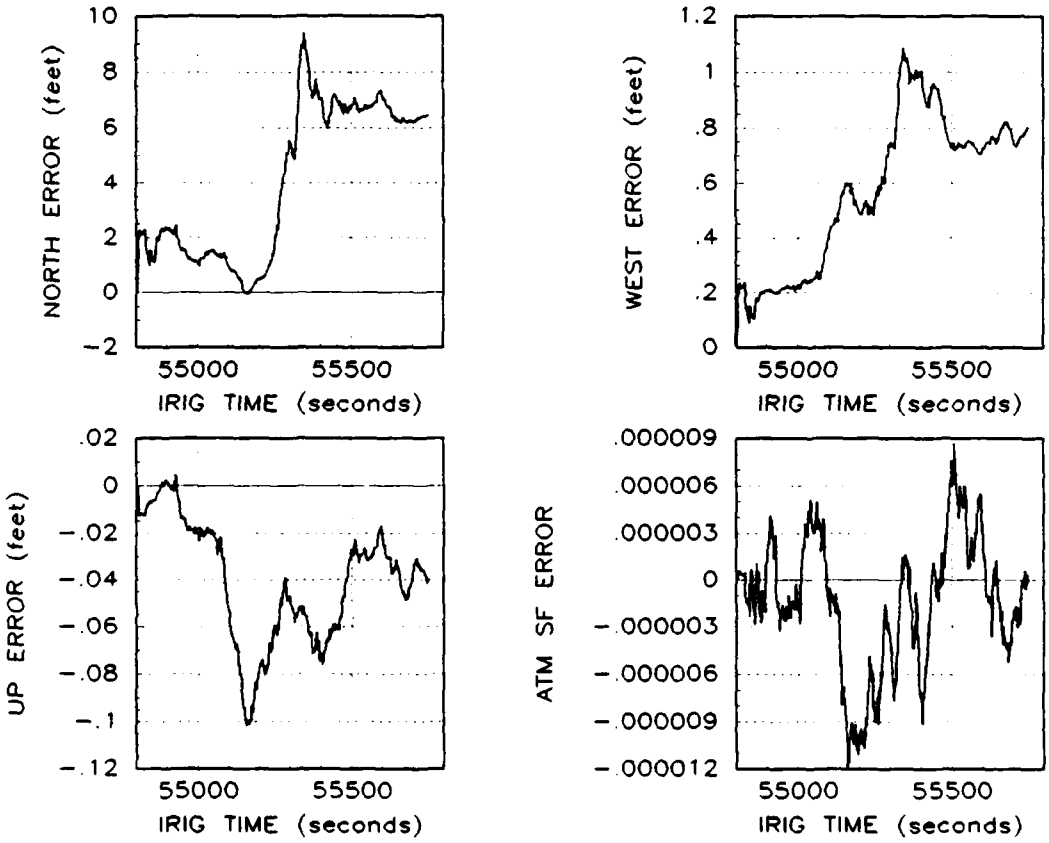

Figure 4.30. Estimated Position Error, Trans 216, Track Run E

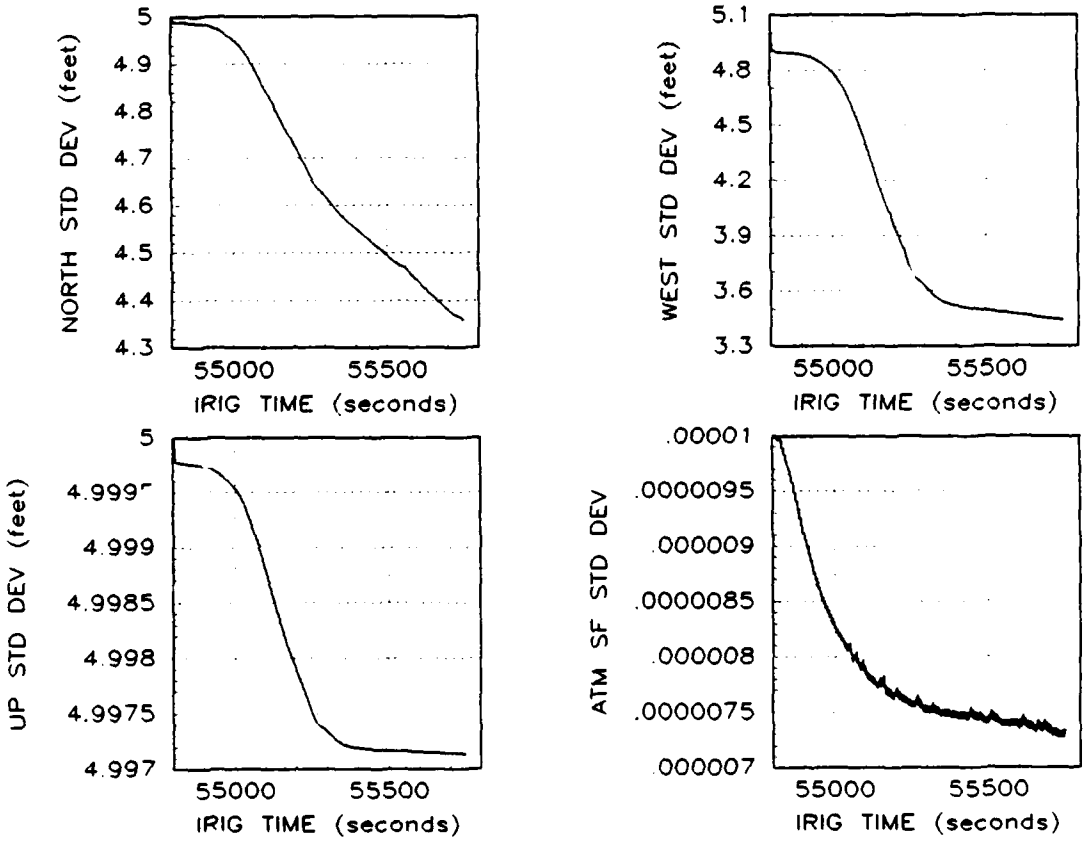

Figure 4.31. Estimated Position Std Dev, Trans 216, Track Run E

4.3 Summary

This chapter presents the results of using the Advanced CIRIS filter to process real CIRIS data (measurements and INS output) from a slow–speed ground test. The objective is to validate the filter's error model by analysis of the measurement residual characteristics and by comparison of the filter's position/velocity estimates with those of the track data acquisition system. Range measurements from one of the six transponders used in the test contain an anomalous oscillation (90 second period), so measurements from this transponder are not used. In general, the baro–altimeter and range–rate residuals appear zero–mean and white, with the expected residual variance achievable by tuning the measurement noise parameters. The range–residuals, although approximately zero–mean, exhibit short duration biases, and the actual residual variance appears to vary significantly among transponders. The errors in the filter's position estimates, relative to the TDAS measurements, fall mostly in the ± 20 ft range and exhibit biases. The corresponding velocity errors are mostly zero–mean with peak magnitudes in the ± 0.3 fps range, although the up–velocity error magnitudes are significantly larger. The problem with the up–velocity magnitudes is most likely due to the vibration environment. The filter's estimates of the transponder survey position errors and atmospheric propagation scale factor appear reasonable, although the associated 1σ plots provide definite indications of near–zero vertical position error observability. The overall results are interpreted as indicating the current filter structure is reasonable, but the adequacy of the measurement models requires further investigation.

V. 70-State Filter Evaluation: Flight Test Data

In this chapter, the performance of the 70-state filter is evaluated using data collected during a C-141 aircraft flight over the Yuma Test Range.

5.1 Data Collection Procedure

The data used in this analysis was collected on 12 September 1989. The CIRIS LN-39 INS, transponder interrogator, baro-altimeter, and HP-1000 computer were placed on a C-141 aircraft that flew from Holloman AFB to Yuma, Arizona and back. During the portion of the flight over the Yuma Test Range, the aircraft was tracked by a laser ranging system (LRS), from which aircraft position and velocity were determined. The LRS measurements are known to be about twice as accurate, on average, than CIRIS I filter estimates [7]. The aircraft trajectory, as determined by the LRS, is plotted in Figure 5.1. Appendix C contains more detailed plots of both the LRS and LN-39 INS indicated position and velocity for the Yuma Test Range portion of the flight.

During the entire flight, the CIRIS equipment recorded measurements from twenty-two different transponders. Since the 70-state filter software can accommodate only 20 transponders, measurements from the two least used transponders are not processed by this filter. The remaining twenty transponders are paired up such that the state switching procedure described in Chapter III is needed only once during the Yuma Test Range portion of the flight.

5.2 70-State Filter Performance

For this flight test, the LRS indicated position and velocity is used as the "truth" by which the the accuracy of the 70-state filter is evaluated. The initial state covariance estimates and other tuning parameters used in this test are exactly those described in Appendix A. The recording of LN-39 INS data and transponder and baro-altimeter measurements began prior to take-off and continued until the aircraft landed. The 70-state filter is used to process this data from just prior to take-off until the aircraft leaves the Yuma area. This requires almost 11 hours of CPU time on a MicroVAX III computer to

process 3.6 hours of real–time data. This figure includes the large amount of I/O required to read the input data and save calculated results for plotting.

The differences between the filter estimated position and velocity and the LRS indicated position and velocity are plotted in Figures 5.2 through 5.7. Compensation is made for the position offset between the LN–39 INS and the laser retro–reflector.

The baro–altimeter measurement residuals are plotted in Figure 5.8. The transponder range and range–rate residuals for the three most frequently interrogated transponders, 160, 163, and 226, are shown in Figures 5.9 through 5.14. The bounding lines on these plots are the residual $\pm 1\sigma$ values predicted by the filter. The baro–altimeter residuals are near zero–mean and have a true variance much smaller than the expected variance except when the aircraft is climbing or diving. During altitude changes, the residual variance increases dramatically. These plots indicate the filter baro–altimeter measurement noise parameter is set too high. It should probably be adjusted as a function of the vertical velocity. The range measurement for all three transponders look nearly ideal. They are near zero–mean, appear white most of the time, and have actual variances close to the expected variances. The range–rate residuals from all three transponders do not possess these ideal characteristics. They appear near zero–mean overall, but they exhibit time correlated variations and have actual variances much larger than the expected variances (some large magnitude residuals are not shown on the plot).

The filter residual tolerance was set to 5σ. During the portion of the flight from Holloman to Yuma (IRIG times 48660 to 53000) the filter received 2,946 barometric altitude measurements, 2,946 transponder range measurements, and 2,946 transponder range–rate measurements. Of these, none of the barometric–altitude measurements were rejected, 97 (3.293%) of the range measurements were rejected, and 135 (4.582%) of the range–rate measurements were rejected. Fifty–two of the rejected range measurements were from transponder 218. During the portion of the flight over the Yuma Test Range (IRIG times 53000 to 63000) the filter received 5,663 barometric altitude measurements, 5,663 transponder range measurements, and 5,663 transponder range–rate measurements. Of these, one (0.018%) of the barometric–altitude measurements was rejected, 83 (1.466%) of the range measurements were rejected, and 1,656 (29.242%) of the range–rate measurements were re-

jected. Forty–two of the rejected range measurements were from transponder 218. However the majority of the range measurements from this particular transponder were accepted by the filter in both portions of the flight.

The rejection of the range–rate measurements is correlated with the aircraft turning maneuvers. This may indicate that modeling the range–rate measurement process as occurring instantaneously is an over–optimistic assumption. The way the range–rate measurements are made by the Cubic RRS actually involves calculating a delta–range (distance units) over a short (approximately 0.5 seconds) measurement time interval. The delta–range, after dividing by the measurement time interval, represents the average range–rate during the interval. During aircraft turning maneuvers, because the INS is not at the aircraft's center of rotation, this average range–rate may not accurately reflect the true instantaneous range–rate at the end of the measurement interval when the measurement is time–tagged. This possibility requires further research; it may necessitate a redesign of the filter's range–rate measurement model.

5.3 CIRIS II Filter Performance

The CIRIS II filter position and velocity estimates are available for this same flight, so it is useful to compare these estimates to the LRS indicated position and velocity. This permits an evaluation of the performance of Advanced CIRIS relative to CIRIS II. The CIRIS II estimates used to make the plots in this section are not corrected for the INS to laser–retroreflector offset, however this type of correction made minimal difference in the corresponding Advanced CIRIS filter plots. The CIRIS II transponder measurement residuals are also available so they may be compared to the corresponding Advanced CIRIS residuals. The CIRIS II filter does not use separate barometric altitude measurements.

The CIRIS II latitude, longitude, and altitude errors, relative to the LRS measurements, are shown in Figures 5.15, 5.16, and 5.17. These plots exhibit spikes similar to the ones in the Advanced CIRIS plots, but the average error magnitudes are larger, especially for the altitude error. The CIRIS II north, west, and up velocity errors, relative to the LRS measurements, are shown in Figures 5.18, 5.19, and 5.20. These plots also contain

spikes similar to the ones in the Advanced CIRIS plots and the average error magnitudes are roughly the same as those of Advanced CIRIS.

The CIRIS II range and range–rate measurement residuals for transponders 160, 163, and 226 are shown in Figures 5.21 through Figures 5.26. Compared to the the corresponding Advanced CIRIS range residuals, the CIRIS II range residuals are obviously biased and have a larger variance. The CIRIS II range–rate residuals are also biased, but they have an obviously smaller variance than the Advanced CIRIS range-rate residuals.

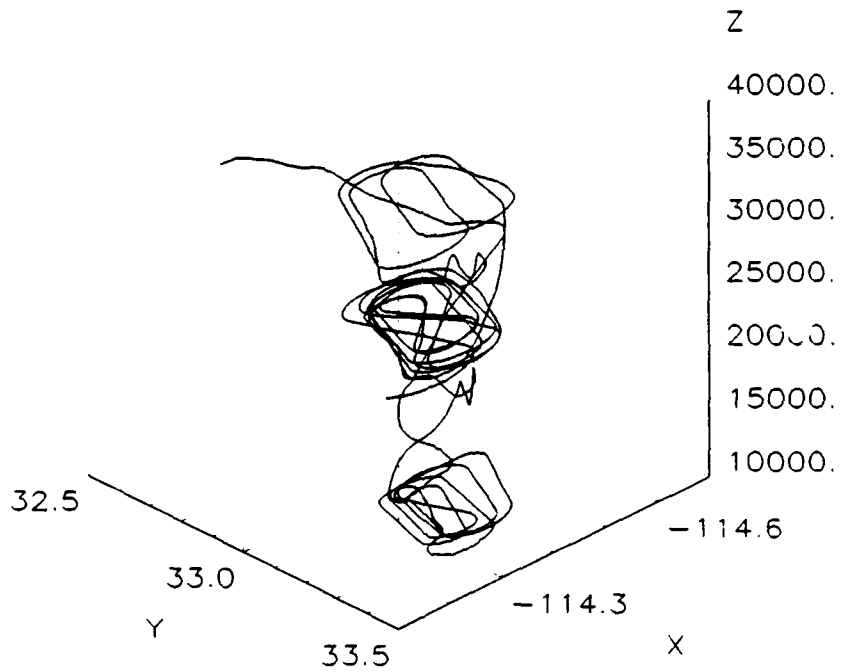

Figure 5.1. C-141 Aircraft Trajectory over Yuma Test Range

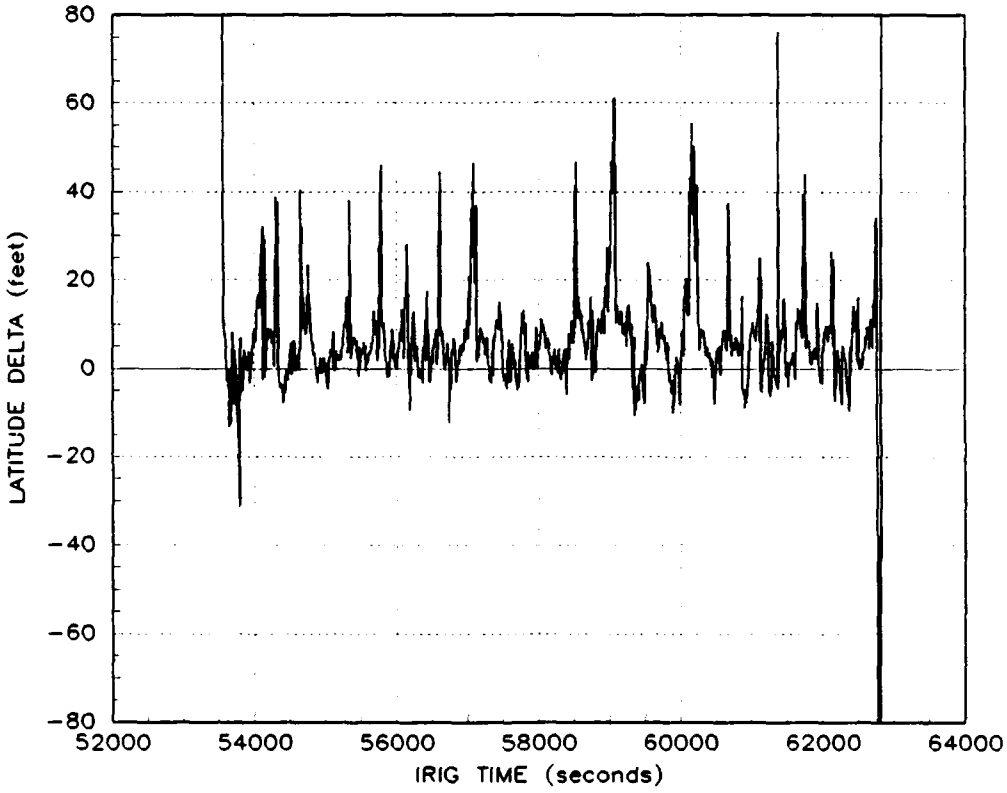

Figure 5.2. Latitude Difference, Yuma Flight, Adv. CIRIS

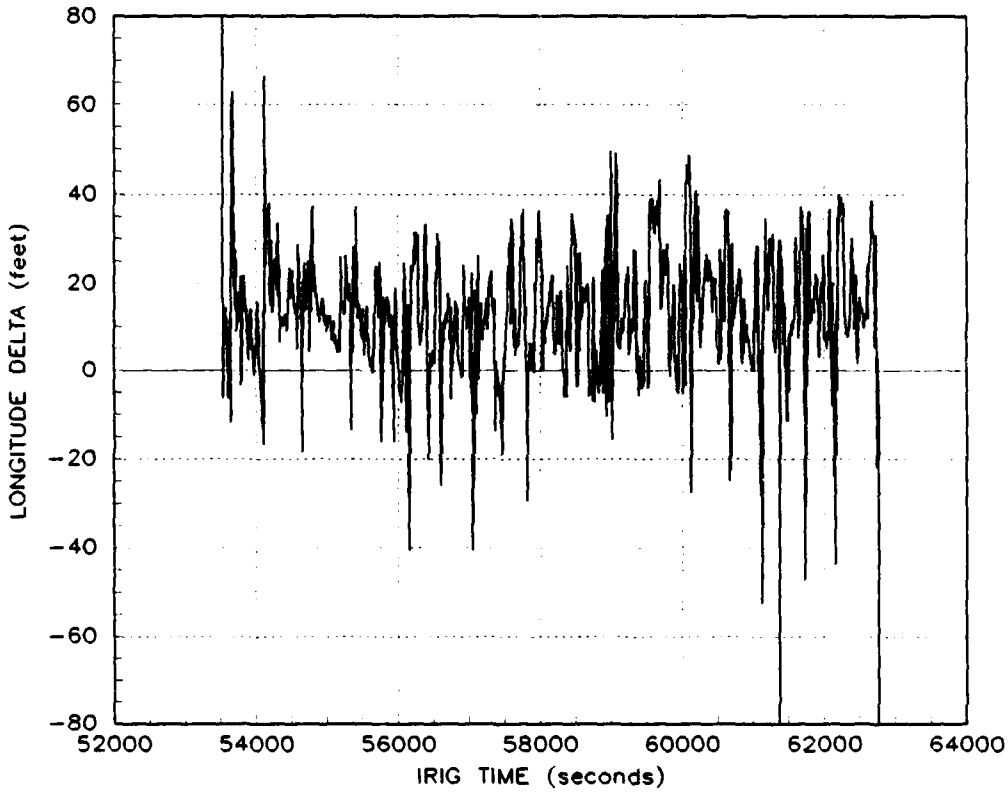

Figure 5.3. Longitude Difference, Yuma Flight, Adv. CIRIS

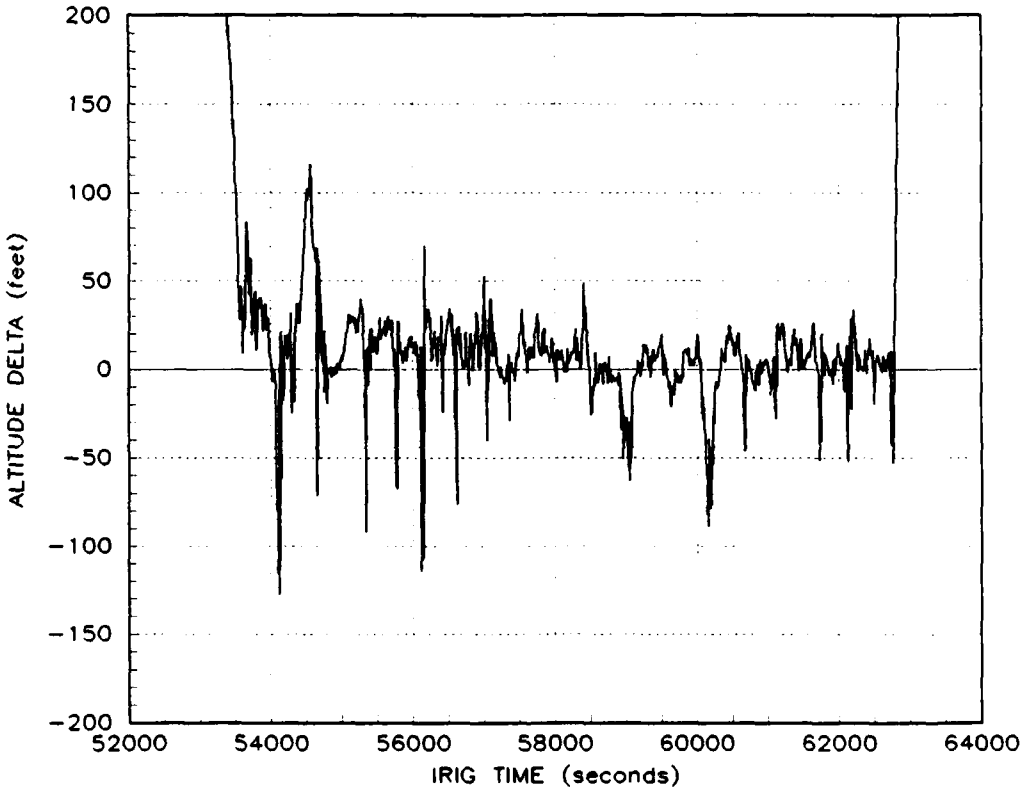

Figure 5.4. Altitude Difference, Yuma Flight, Adv. CIRIS

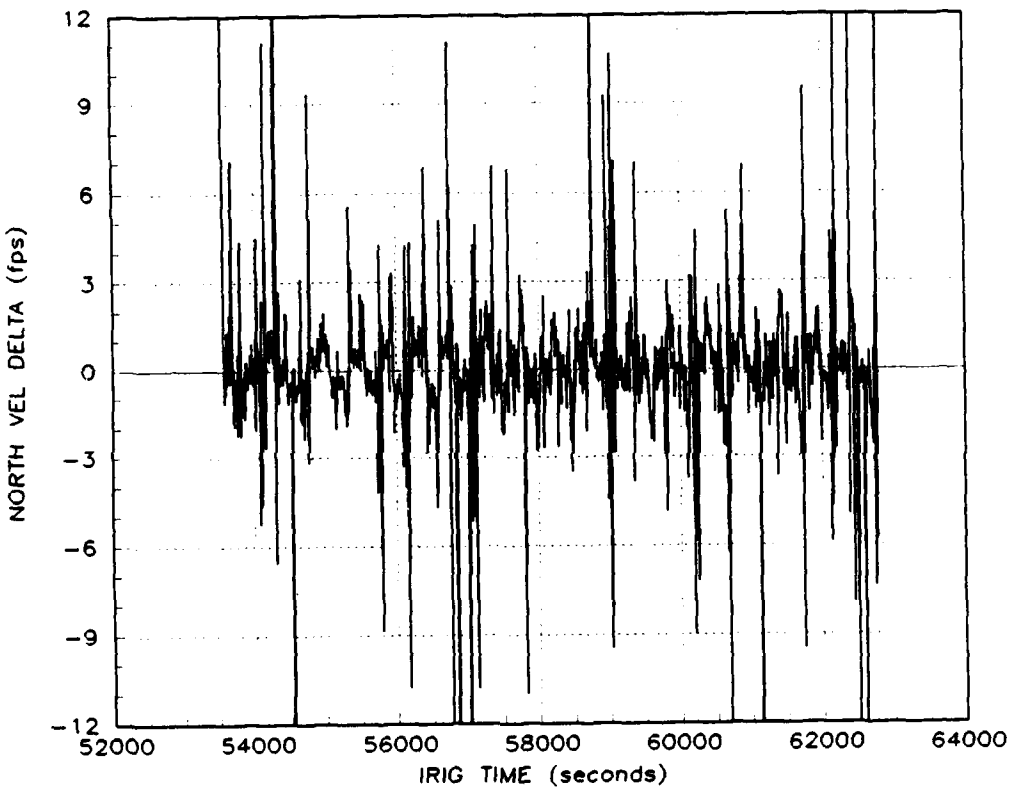

Figure 5.5. North Velocity Difference, Yuma Flight, Adv. CIRIS

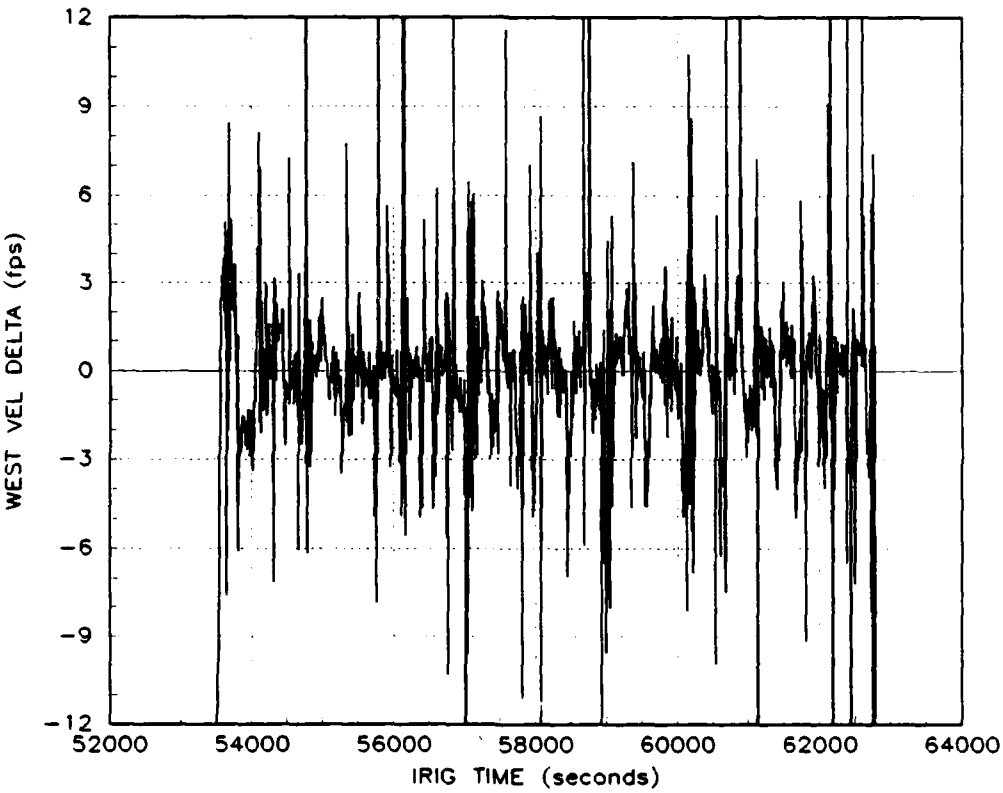

Figure 5.6. West Velocity Difference, Yuma Flight, Adv. CIRIS

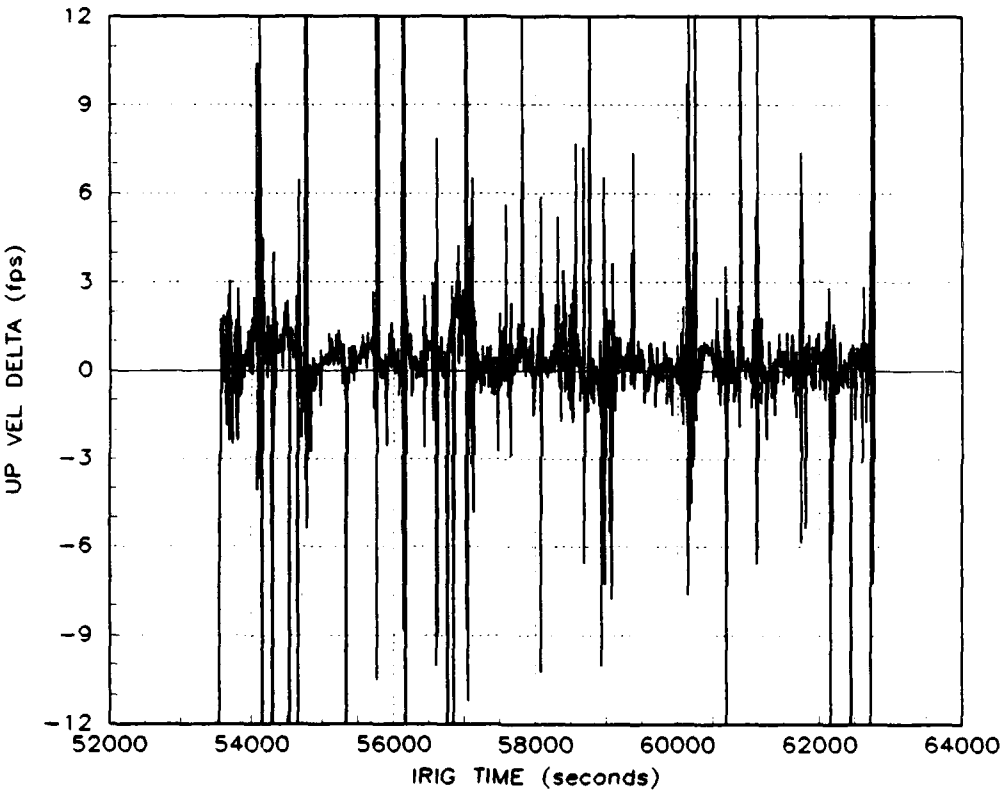

Figure 5.7. Up Velocity Difference, Yuma Flight, Adv. CIRIS

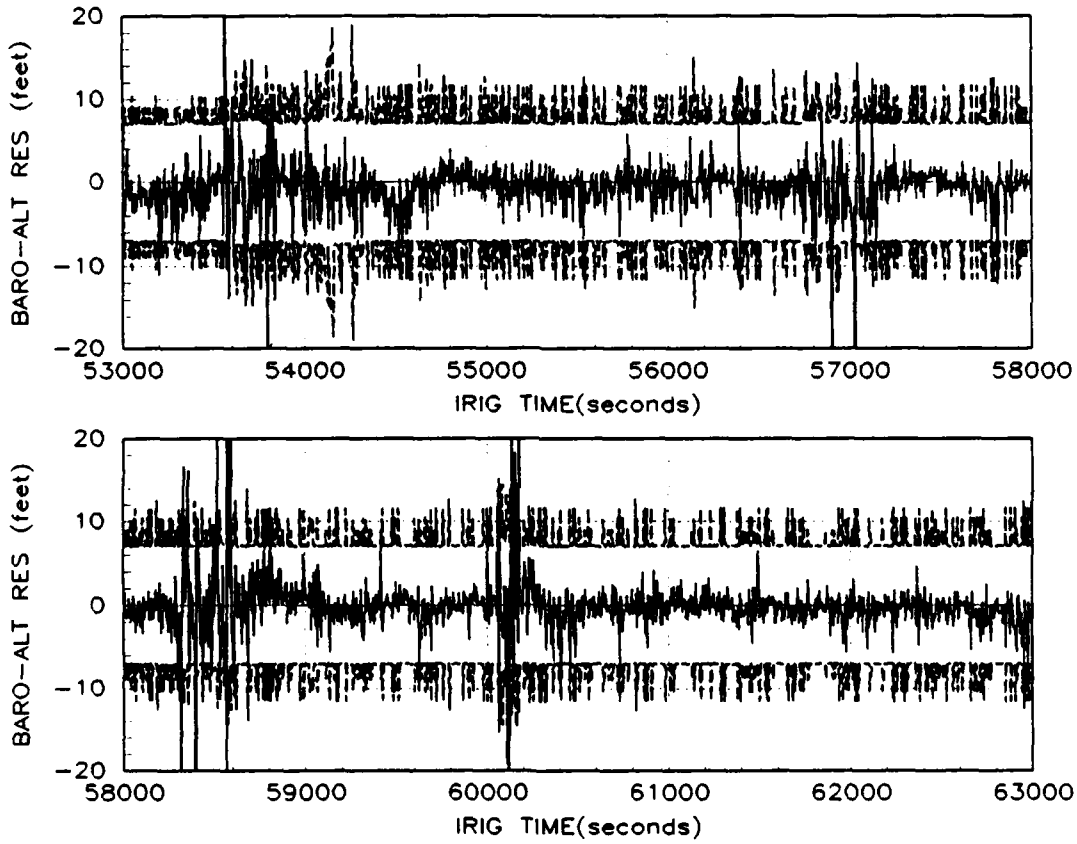

Figure 5.8. Baro–Altitude Meas. Residuals, Yuma Flight, Adv. CIRIS

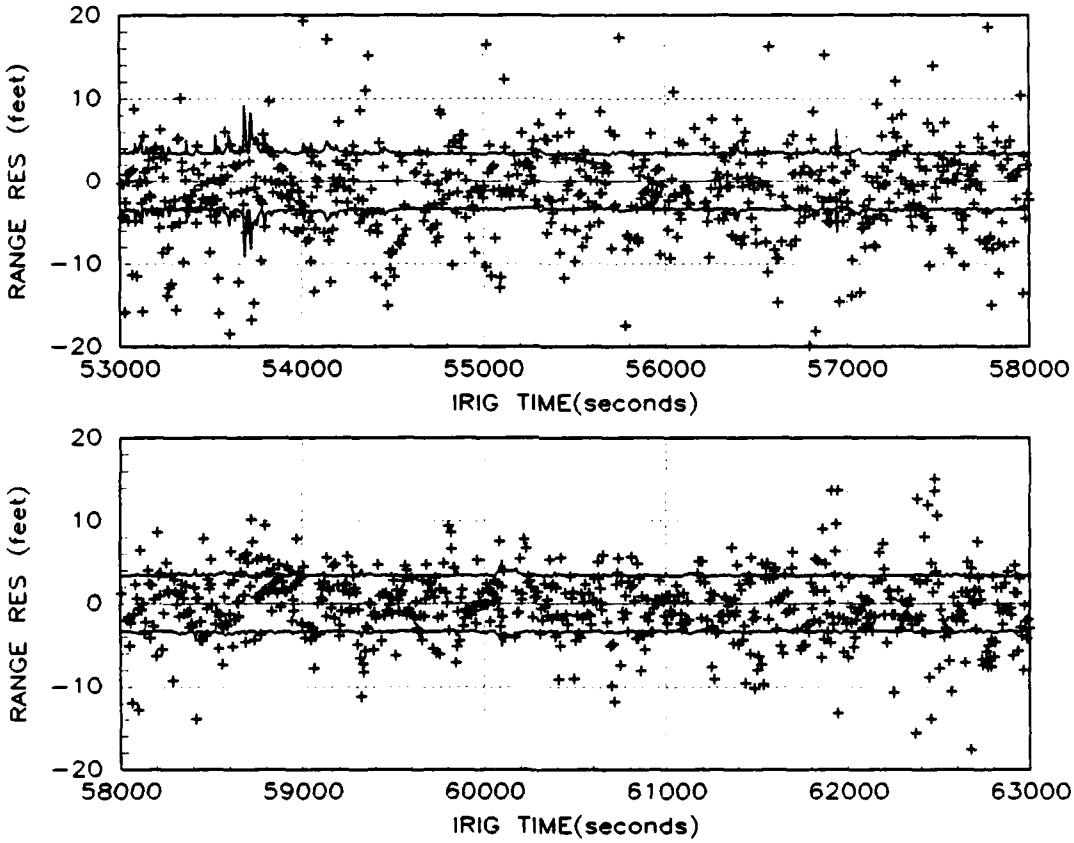

Figure 5.9. Trans. 160 Range Meas. Residuals, Yuma Flight, Adv. CIRIS

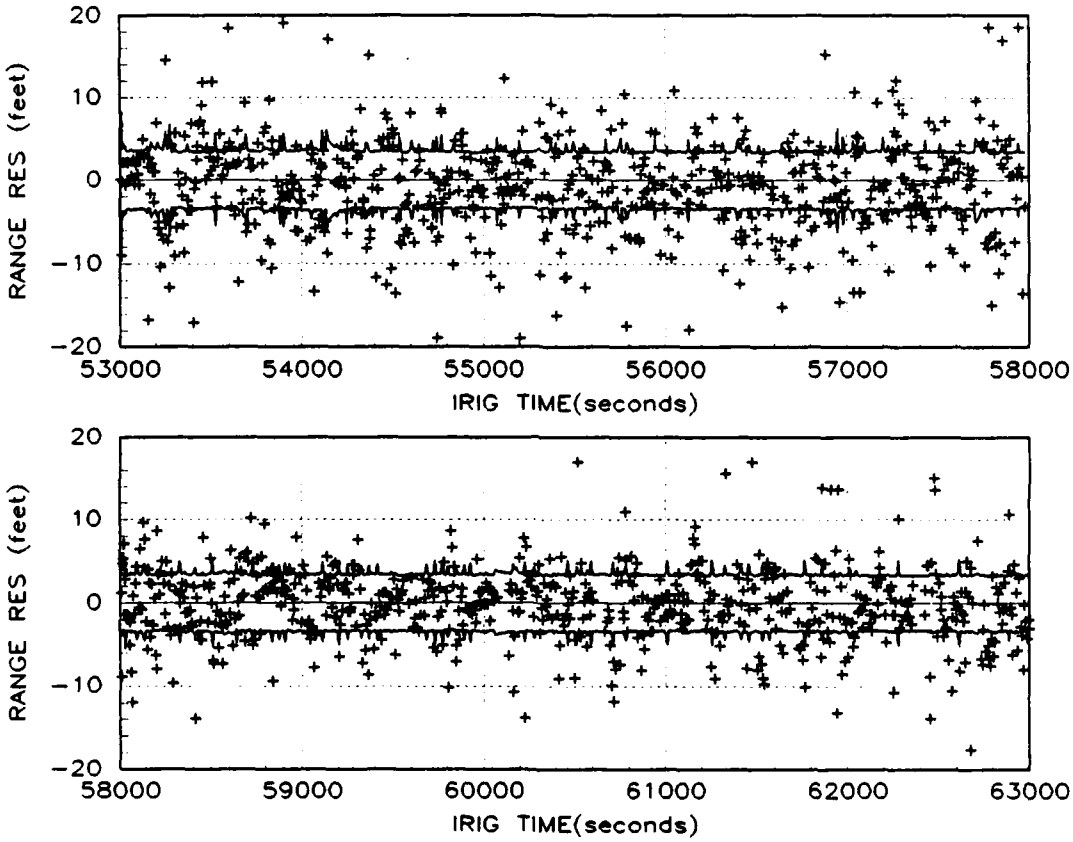

Figure 5.10. Trans. 163 Range Meas. Residuals, Yuma Flight, Adv. CIRIS

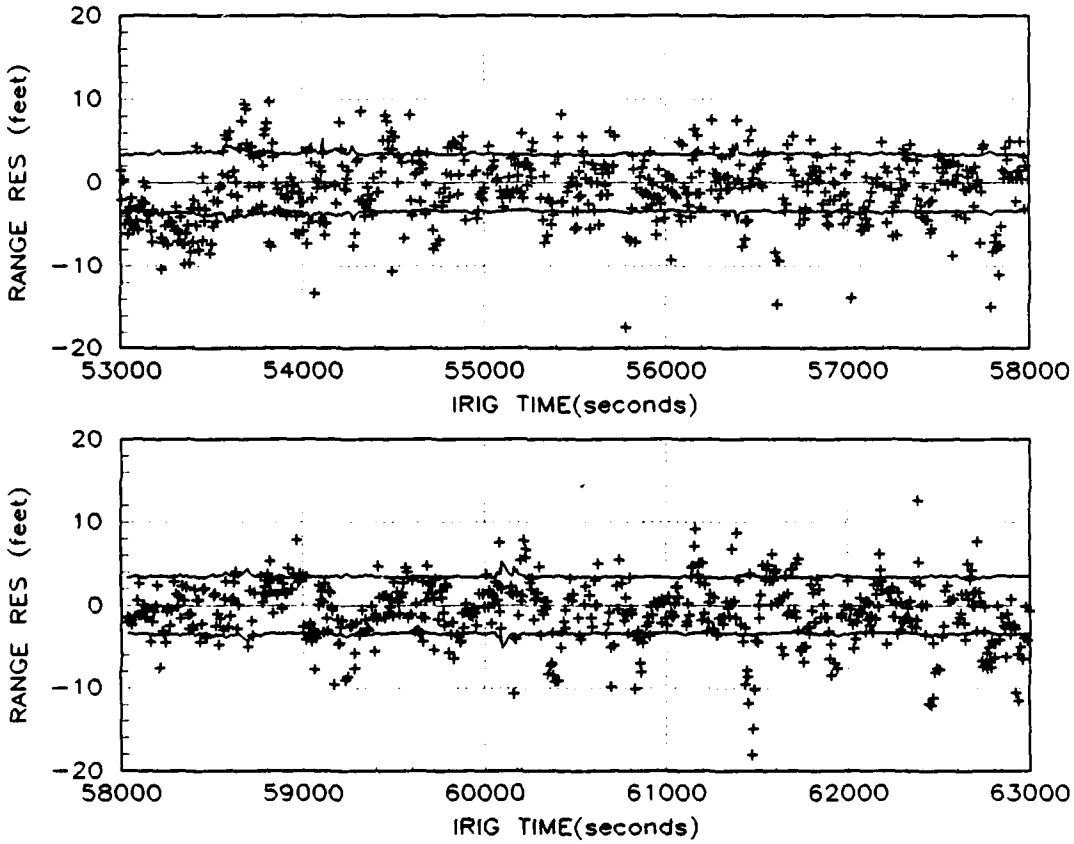

Figure 5.11. Trans. 226 Range Meas. Residuals, Yuma Flight, Adv. CIRIS

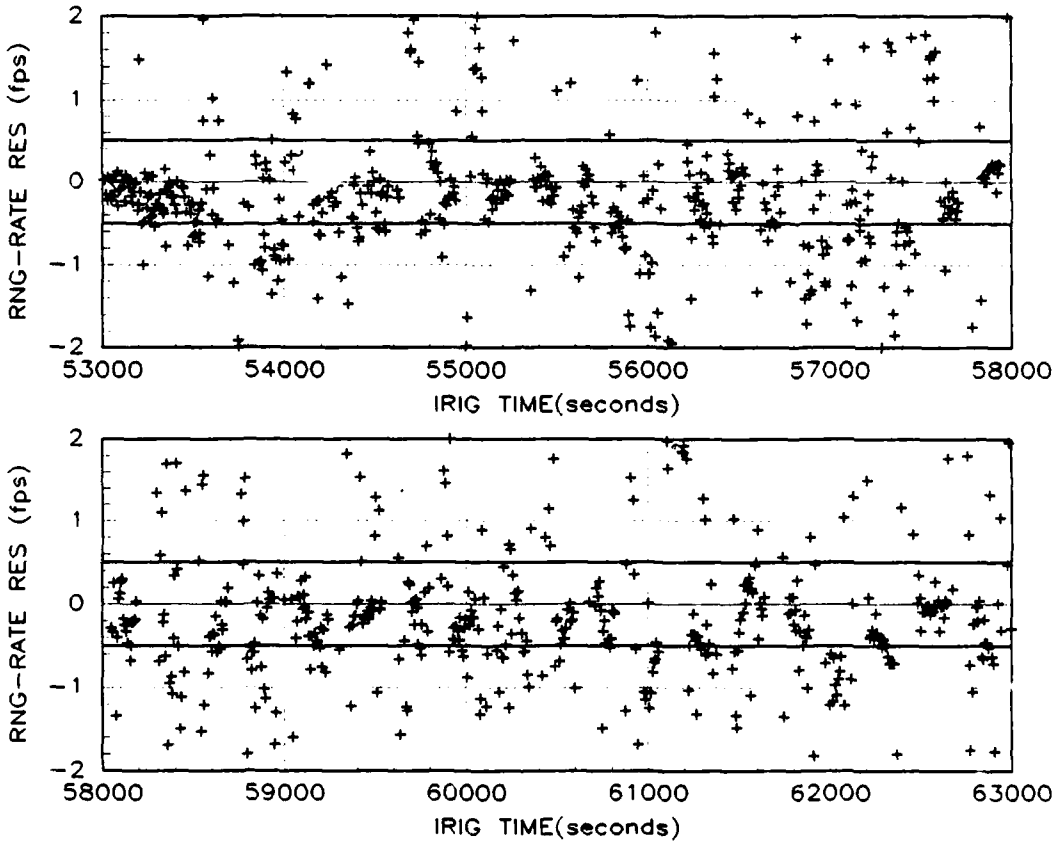

Figure 5.12. Trans. 160 Range–Rate Meas. Residuals, Yuma Flight, Adv. CIRIS

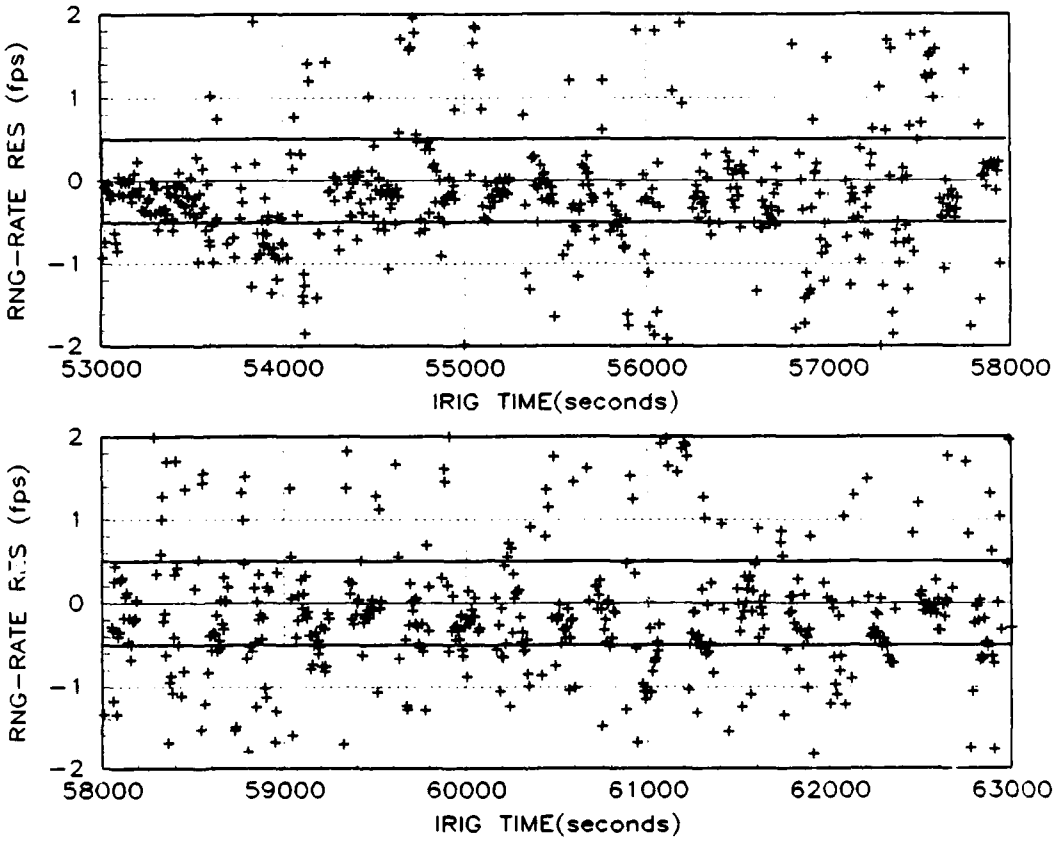

Figure 5.13. Trans. 163 Range-Rate Meas. Residuals, Yuma Flight, Adv. CIRIS

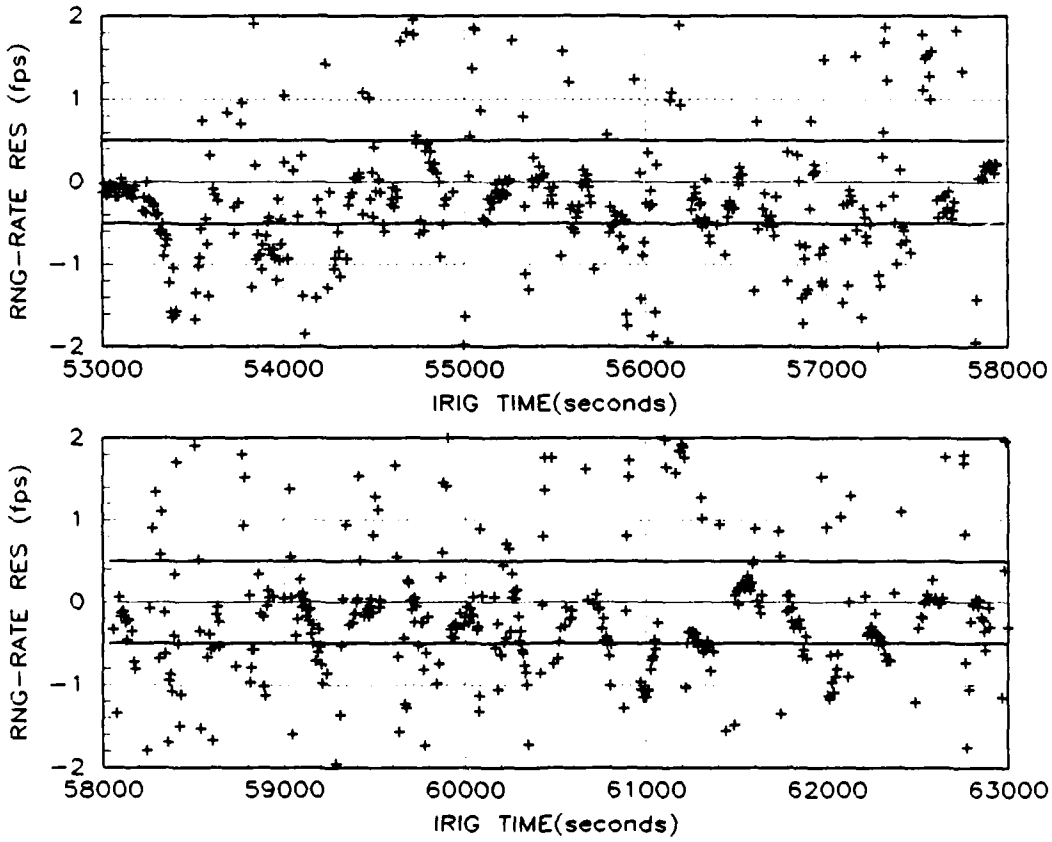

Figure 5.14. Trans. 226 Range–Rate Meas. Residuals, Yuma Flight, Adv. CIRIS

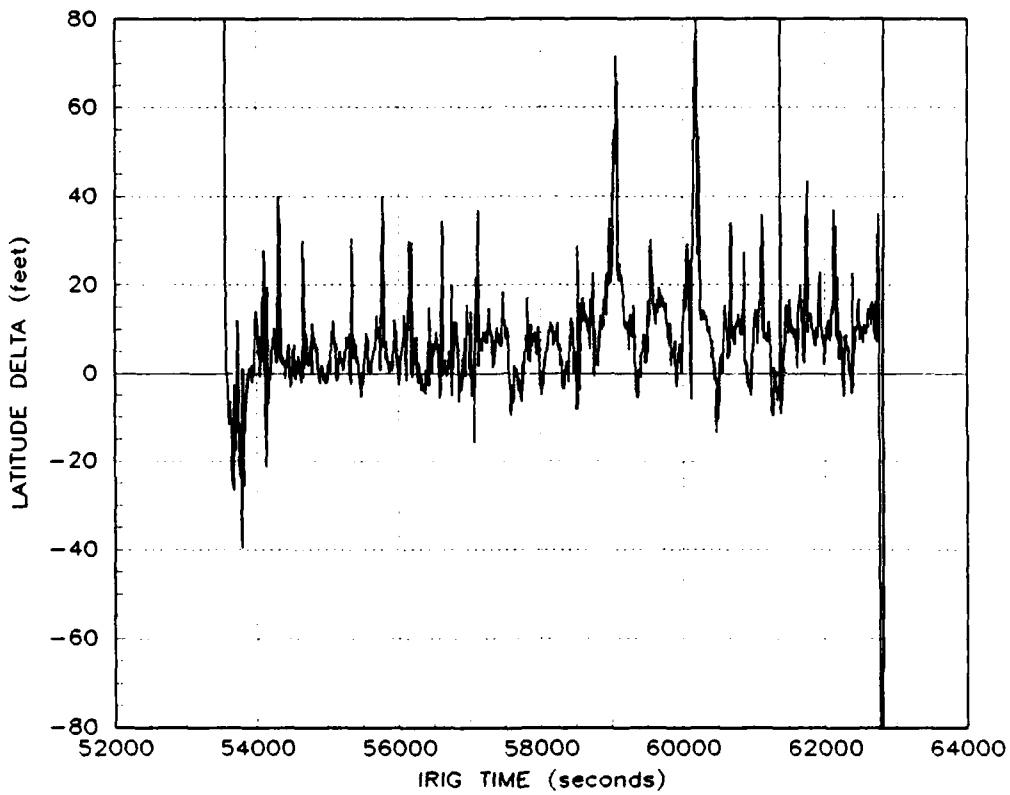

Figure 5.15. Latitude Difference, Yuma Flight, CIRIS II

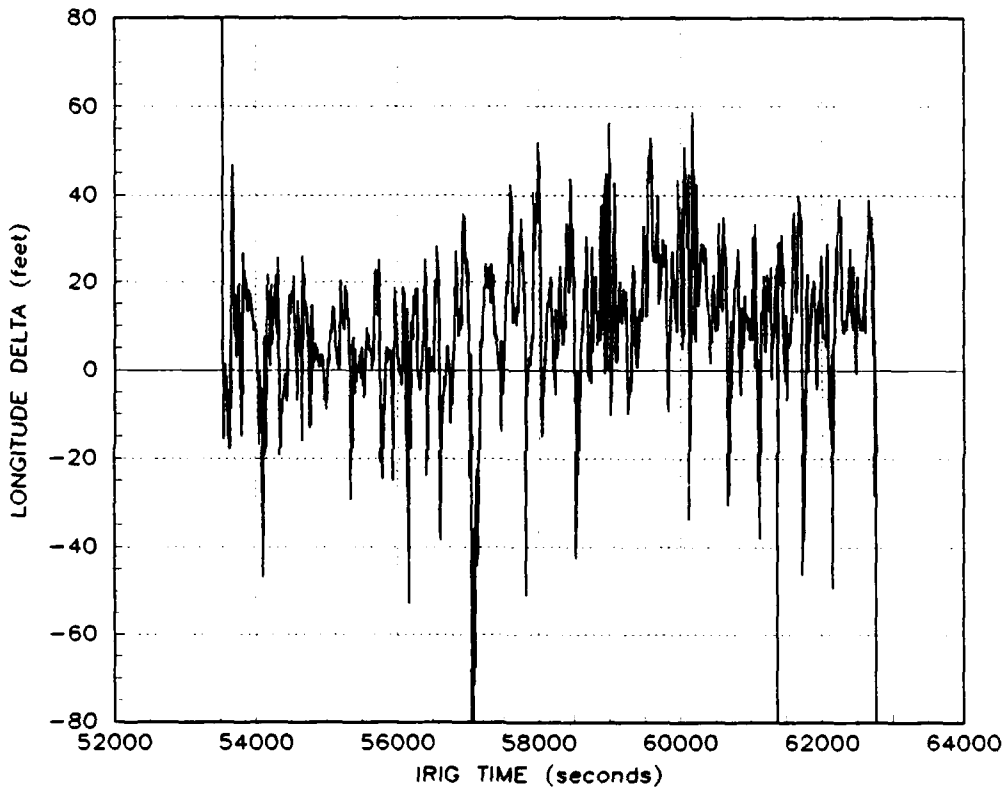

Figure 5.16. Longitude Difference, Yuma Flight, CIRIS II

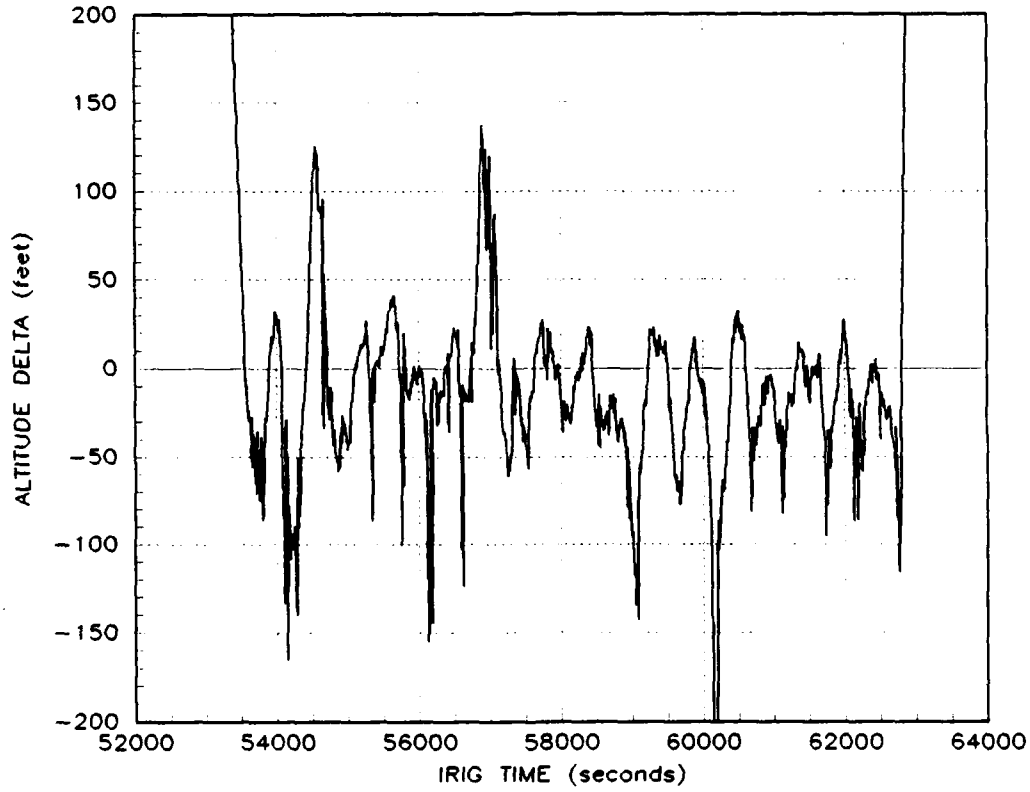

Figure 5.17. Altitude Difference, Yuma Flight, CIRIS II

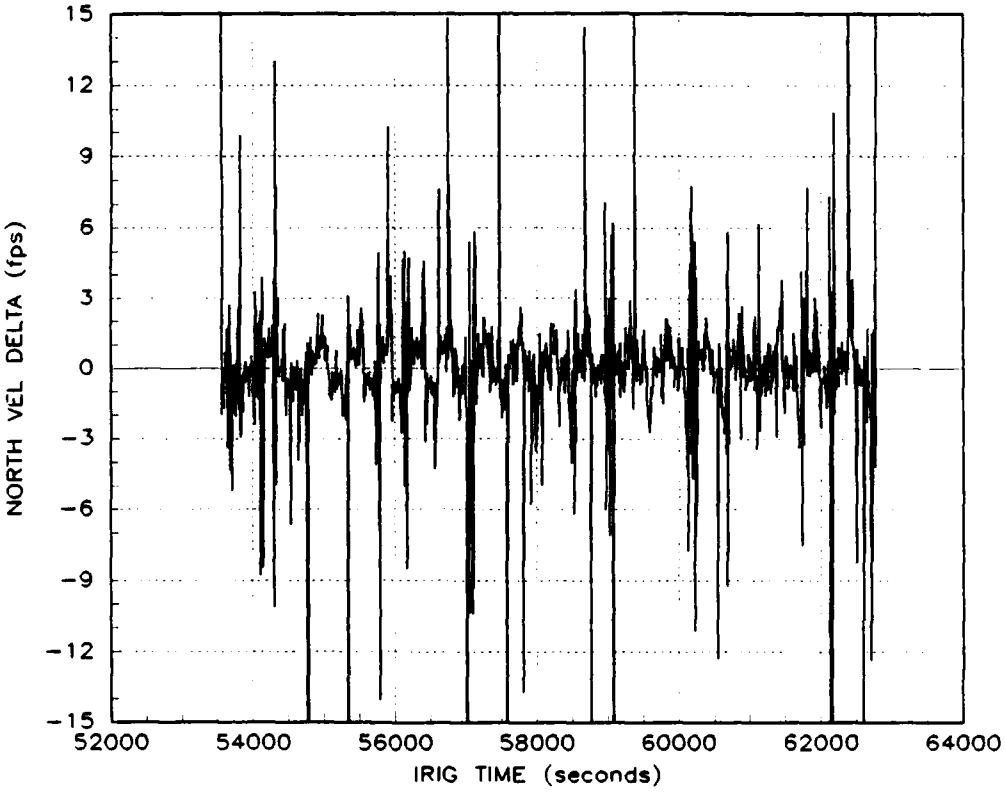

Figure 5.18. North Velocity Difference, Yuma Flight, CIRIS II

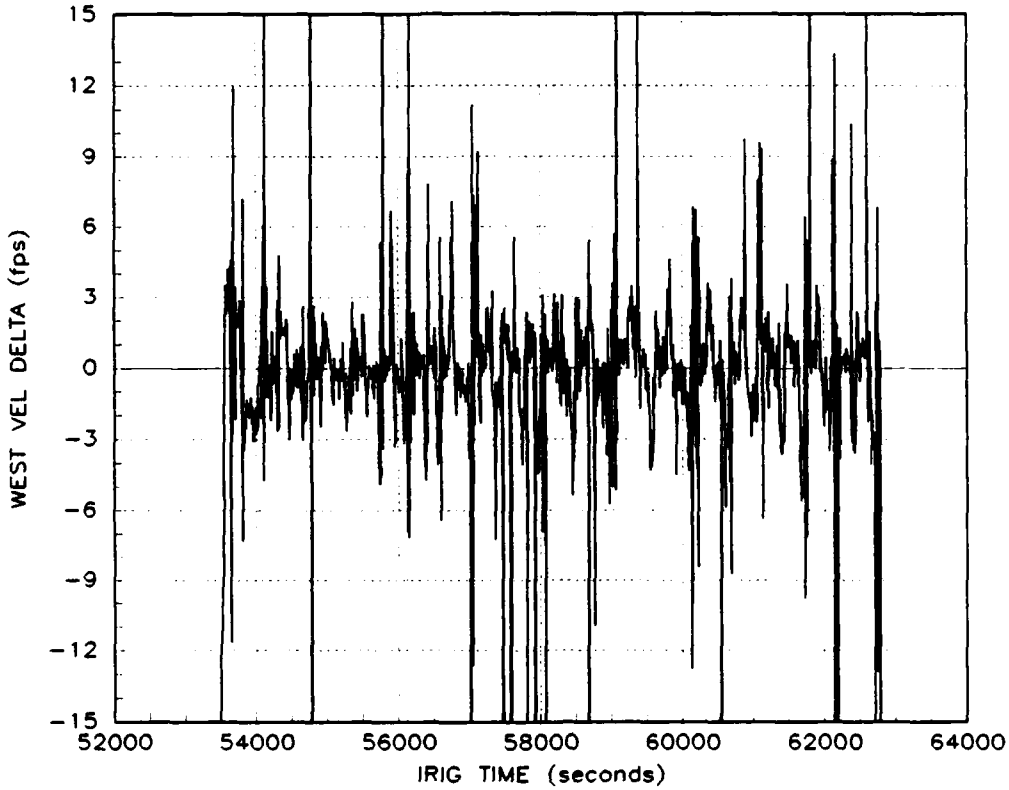

Figure 5.19. West Velocity Difference, Yuma Flight, CIRIS II

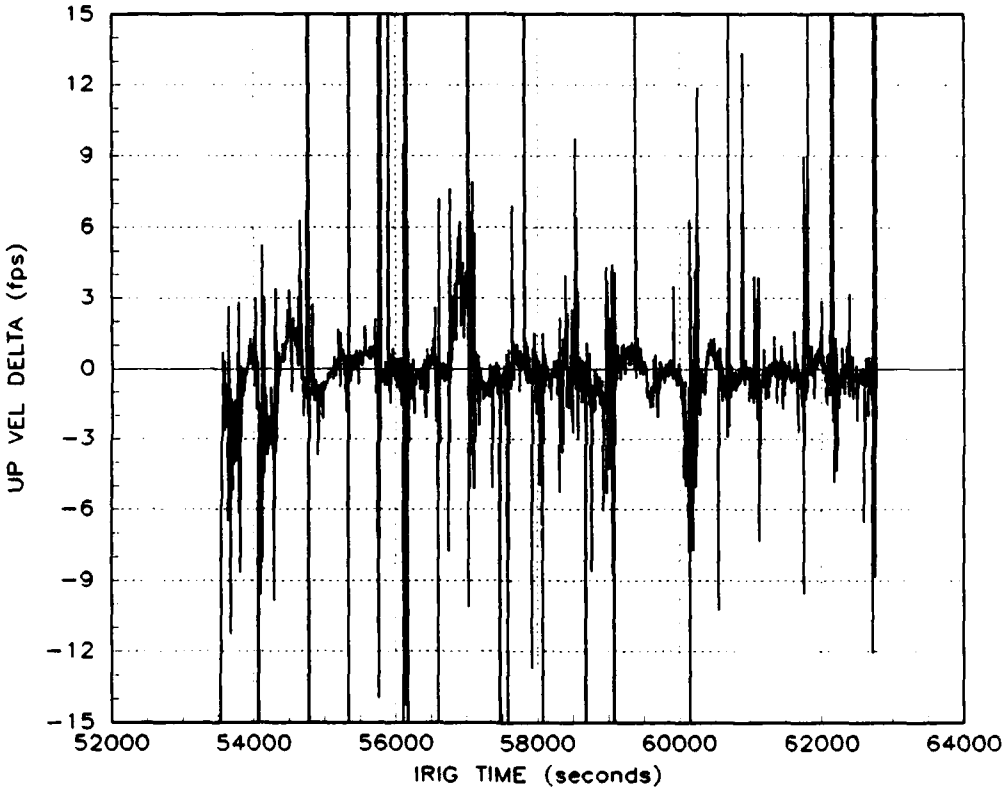

Figure 5.20. Up Velocity Difference, Yuma Flight, CIRIS II

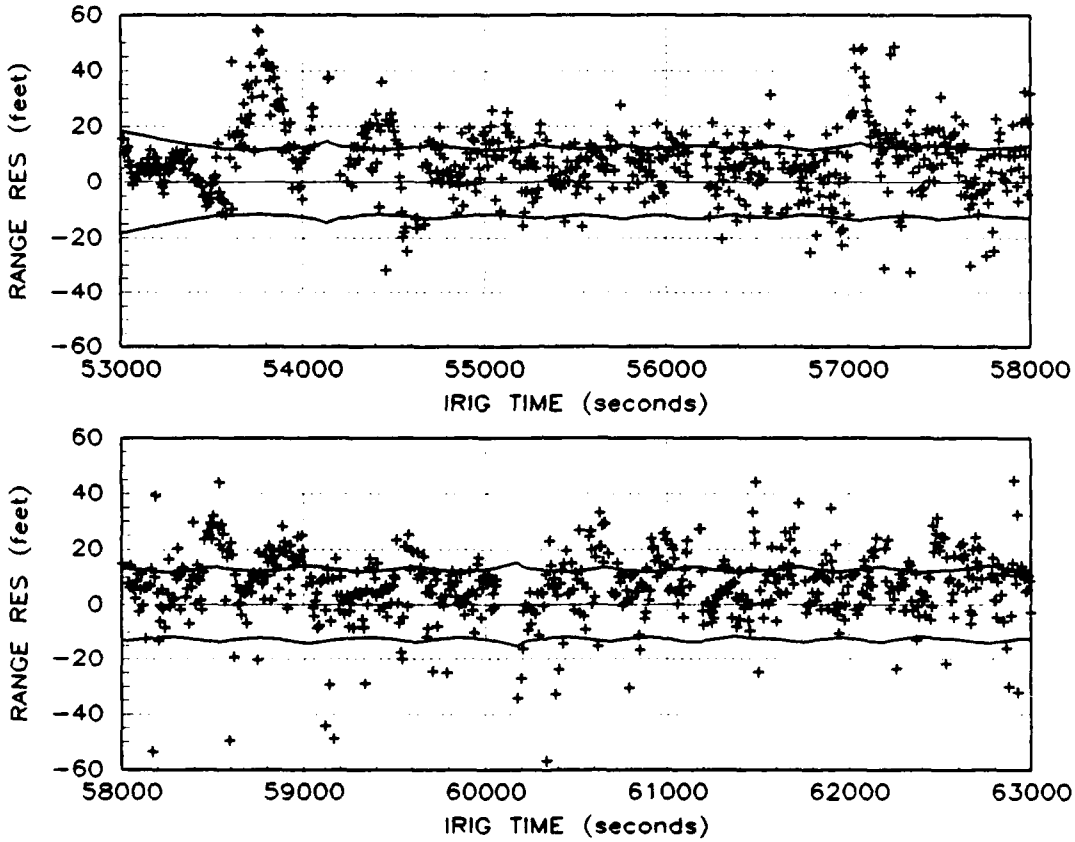

Figure 5.21. Transponder 160 Range Measurement Residuals, CIRIS II

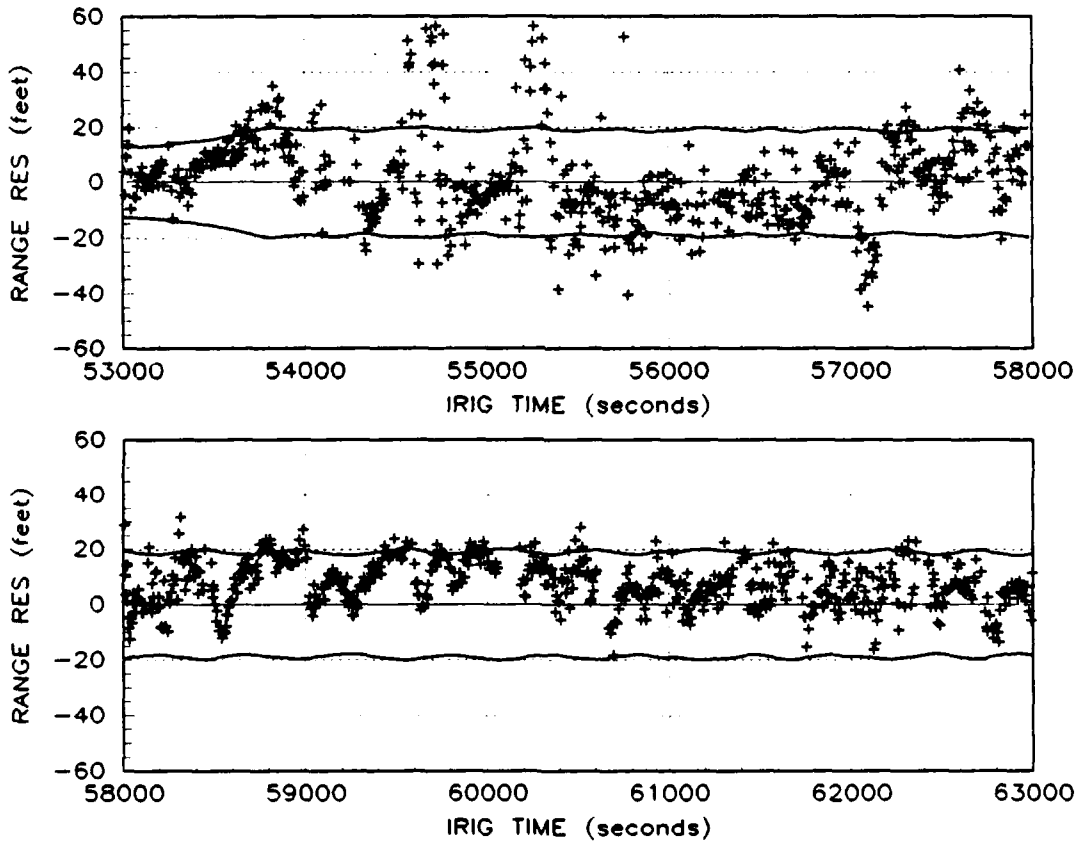

Figure 5.22. Transponder 163 Range Measurement Residuals, CIRIS II

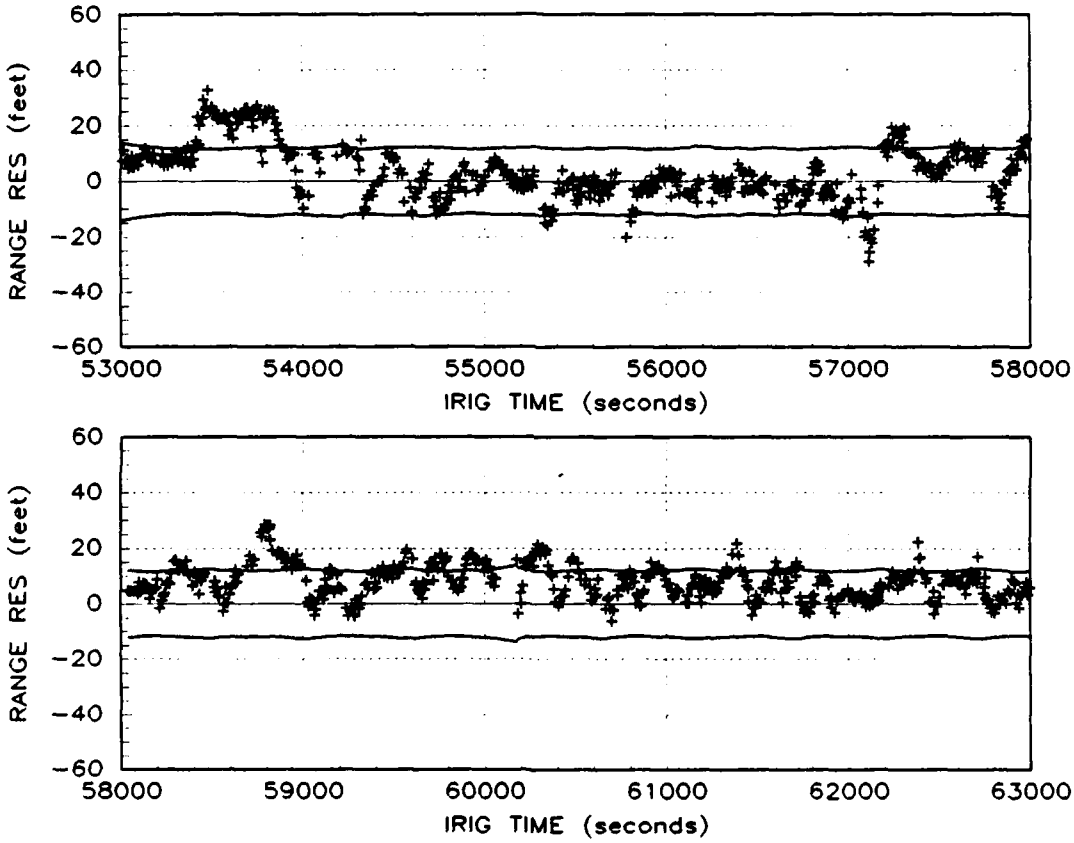

Figure 5.23. Transponder 226 Range Meas. Residuals, CIRIS II

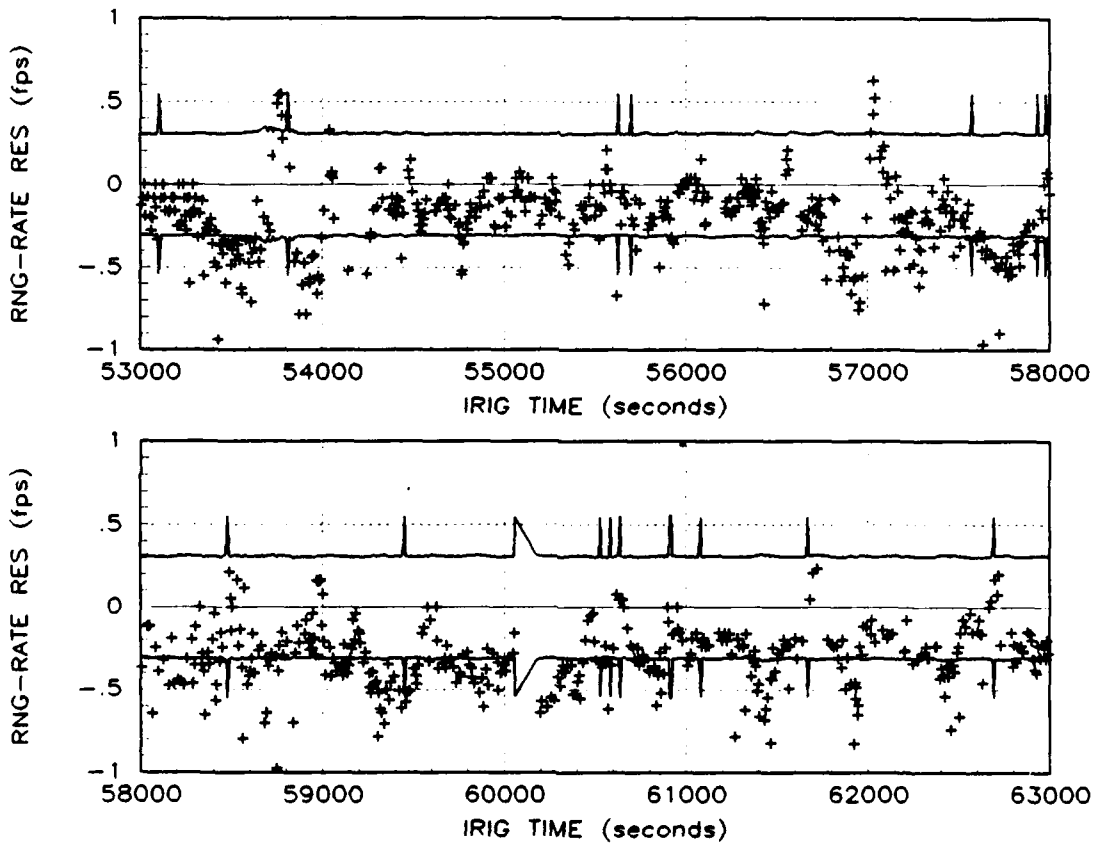

Figure 5.24. Transponder 160 Range–Rate Meas. Residuals, CIRIS II

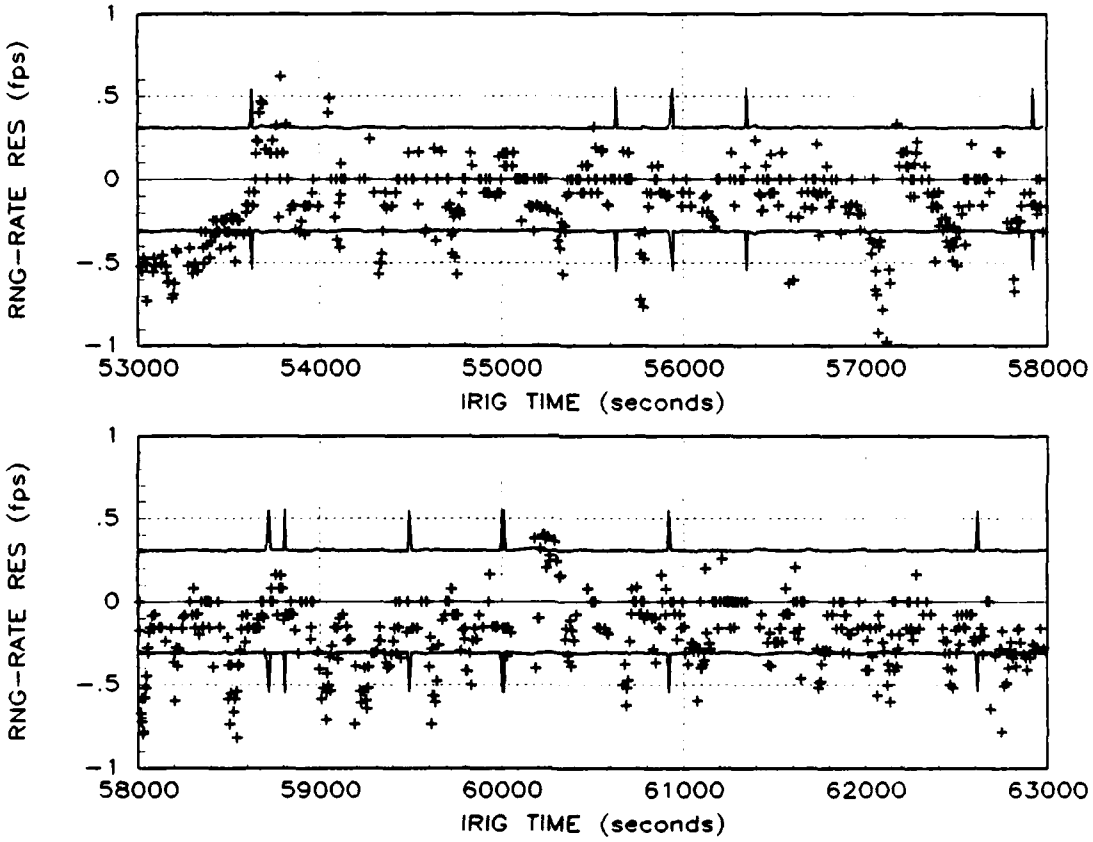

Figure 5.25. Transponder 163 Range–Rate Meas. Residuals, CIRIS II

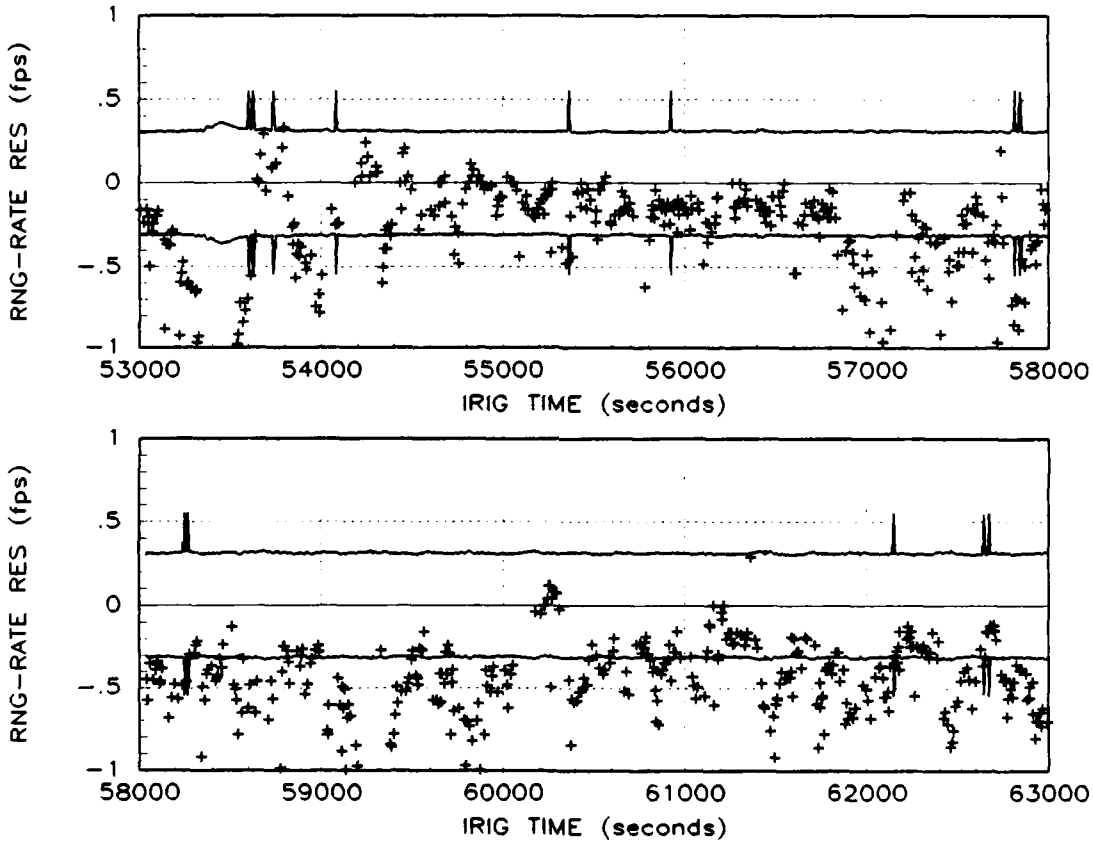

Figure 5.26. Transponder 226 Range–Rate Meas. Residuals, CIRIS II

5.4 *Summary*

This chapter presents the results of using the Advanced CIRIS filter to process real CIRIS data recorded during a C–141 aircraft flight over the Yuma Test Range. During flight, the aircraft was tracked by an independent laser ranging system (LRS) whose measurements are known to be roughly twice as accurate, on average, as CIRIS I filter estimates. Use of this data provides additional filter model validity information through analysis of residual characteristics. In general, the Advanced CIRIS filter's measurement residuals appear reasonably white and zero–mean. The actual variance of the baro–altimeter measurement residuals increases significantly during aircraft altitude changes. The actual variance of the range–rate measurement residuals appears correlated with aircraft maneuvers; the large residual magnitudes during turning maneuvers result in an excessive proportion of the range–rate measurements being rejected by the filter. By comparison, the CIRIS II range measurement residuals exhibit a significantly larger true variance than those of Advanced CIRIS, and they also exhibit long duration biases. However the CIRIS II range–rate measurement residuals, while also biased, have an obviously smaller actual variance than those of Advanced CIRIS.

The availability of CIRIS II filter estimates for this same flight permits an estimation accuracy comparison between Advanced CIRIS and CIRIS II, both relative to the LRS measurements. On average, the relative errors in the Advanced CIRIS position and velocity estimates are smaller than those of CIRIS II. The advantage of Advanced CIRIS is most noticeable in the altitude error plots.

VI. *Proposed Fixed-Interval Smoother*

This chapter describes a fixed-interval smoother algorithm whose simple structure makes it a good companion program for the current MSOFE-based Advanced CIRIS filter software. The smoother software was not implemented in this thesis effort due to lack of time and concern over data storage requirements.

6.1 Fixed-Interval Smoothing

The term *smoother* is used to describe a type of estimator that makes use of some or all measurements taken after the time of interest as well as all of the measurements preceeding that time [9]. This characteristic prevents the real-time computation of the smoothed estimates, but it provides the potential for more accurate estimates. Given a time interval of interest, $[t_o, t_f]$ and a time t_i in this interval, a Kalman filter propagates the conditional probability density function shown in Equation (2.24) to yield the expectation of $\mathbf{x}(t_i)$ conditioned on $\mathbf{Z}_i$, the measurement history through time t_i. This is expressed as

$$\hat{\mathbf{x}}(t_i^+) = E\{\mathbf{x}(t_i) \mid \mathbf{Z}(t_i, \omega_k) = \mathbf{Z}_i\} \tag{6.1}$$

$$\hat{\mathbf{x}}(t_i^-) = E\{\mathbf{x}(t_i) \mid \mathbf{Z}(t_{i-1}, \omega_k) = \mathbf{Z}_{i-1}\} \tag{6.2}$$

In contrast, the smoothed estimate at time t_i is conditioned on the measurement history through time t_j, where $t_j > t_i$. This is written as

$$\hat{\mathbf{x}}(t_i/t_j) = E\{\mathbf{x}(t_i) \mid \mathbf{Z}(t_j, \omega_k) = \mathbf{Z}_j\}, \qquad j > i \tag{6.3}$$

A *fixed-interval* smoother uses all measurements through the final time. In other words, $t_j \equiv t_f$. The other types of smoothers are *fixed-point* and *fixed-lag*. This chapter is not intended to present the analytic development of smoother equations. For those details, the reader should consult references [9,10].

A fixed-interval smoothing algorithm may be implemented as a two-pass Kalman filtering procedure: a standard (or extended) Kalman filter for the forward pass and an inverse-covariance (or extended inverse-covariance) Kalman filter for the backward pass. A smoothing algorithm may be further characterized as discrete-time or continuous-time,

depending on the underlying state dynamics propagation model (state transition matrix or matrix differential equation, respectively). The MSOFE–based Advanced CIRIS Kalman filter uses a continuous time model so, ideally, a companion smoothing program should use a continuous–time smoothing algorithm. However, the continuous–time smoother equations are quite complicated and difficult to implement [10]. For this reason, the simple formulation for a discrete–time fixed–interval smoother developed by Meditch [10] is adapted for use with the Advanced CIRIS Kalman filter. This algorithm is also described in reference [9:14–15].

The smoothing procedure is as follows. During the forward filter pass, the quantities $\hat{\mathbf{x}}(t_i^-)$, $\mathbf{P}(t_i^-)$, $\hat{\mathbf{x}}(t_i^+)$, and $\mathbf{P}(t_i^+)$ are saved for all measurement times in the interval $[t_o, t_f]$. The dynamics matrix $\mathbf{F}[\hat{\mathbf{x}}(t_i^+)]$ must also be saved at these times for use in computing the state transition matrix. Starting from the boundary condition

$$\hat{\mathbf{x}}(t_f/t_f) = \hat{\mathbf{x}}(t_f^+) \tag{6.4}$$

the smoothed estimate is generated backward in time using

$$\hat{\mathbf{x}}(t_i/t_f) = \hat{\mathbf{x}}(t_i^+) + \mathbf{A}(t_i)\left[\hat{\mathbf{x}}(t_{i+1}/t_f) - \hat{\mathbf{x}}(t_{i+1}^-)\right] \tag{6.5}$$

where the "smoothing estimator gain matrix" $\mathbf{A}(t_i)$ is given by

$$\mathbf{A}(t_i) = \mathbf{P}(t_i^+)\,\boldsymbol{\Phi}^T(t_{i+1}, t_i)\,\mathbf{P}^{-1}(t_{i+1}^-) \tag{6.6}$$

The state transition matrix $\boldsymbol{\Phi}(t_{i+1}, t_i)$, whose transpose is required in Equation (6.6), is the solution to the differential equation

$$\dot{\boldsymbol{\Phi}}(t, t_{i-1}) = \mathbf{F}[\hat{\mathbf{x}}(t/t_{i-1})]\,\boldsymbol{\Phi}(t, t_{i-1}), \qquad t \in [t_{i-1}, t_i) \tag{6.7}$$

If the time interval $[t_{i-1}, t_i]$ is sufficiently small, so that $\mathbf{F}[\hat{\mathbf{x}}(t/t_{i-1})]$ is essentially constant over the interval, then $\boldsymbol{\Phi}(t_{i+1}, t_i)$ may be calculated using

$$\boldsymbol{\Phi}(t_{i+1}, t_i) = \exp\left\{\mathbf{F}[\hat{\mathbf{x}}(t_{i+1}^+)]\,(t_{i+1} - t_i)\right\} \tag{6.8}$$

Analogous to the forward–pass filter covariance matrix, the covariance matrix for the smoothed estimates is $\mathbf{P}(t_i/t_f)$. This smoother covariance matrix retains the interpretation as the covariance of the zero–mean Gaussian estimation error $[\hat{\mathbf{x}}(t_i/t_f) - \mathbf{x}(t_i)]$. The

smoother covariance is generated backwards starting from the boundary condition

$$\mathbf{P}(t_i/t_f) = \mathbf{P}(t_f^+) \tag{6.9}$$

using the recursion

$$\mathbf{P}(t_i/t_f) = \mathbf{P}(t_i^+) + \mathbf{A}(t_i)\left[\mathbf{P}(t_{i+1}/t_f) - \mathbf{P}(t_{i+1}^-)\right]\mathbf{A}^T(t_i) \tag{6.10}$$

6.2 Application to the Advanced CIRIS Filter

The smoothing procedure described in the previous section may require large amounts of disk space, depending on the state vector length and the number of measurement times in the fixed–interval. Consider a one hour interval with a measurement vector processed every second; the interval contains 3600 measurement times. The quantities $\hat{\mathbf{x}}(t_i^-)$, $\mathbf{P}(t_i^-)$, $\hat{\mathbf{x}}(t_i^+)$, $\mathbf{P}(t_i^+)$ and $\mathbf{F}[\mathbf{x}(t_i^+)]$ must be saved at each measurement time. Because the $\mathbf{P}$ matrix is symmetric, only the upper triangular part need be stored. For a state vector length of 70, $\hat{\mathbf{x}}(t_i^-)$ and $\hat{\mathbf{x}}(t_i^+)$ each require 70 64–bit data words, the upper triangles of $\mathbf{P}(t_i^-)$ and $\mathbf{P}(t_i^+)$ each require 2,485 64–bit data words, and $\mathbf{F}[\mathbf{x}(t_i^+)]$ requires 4,900 64–bit data words. The result is 10,010 data words (80,080 bytes) requiring storage at each measurement time. *The total (unformatted) disk storage required for the one hour interval is over 288 megabytes.* Storage of time–tag information requires another 28,800 bytes. While this amount of disk space may be available on a dedicated computer, such resources are not yet generally available.

Storage requirements can be significantly reduced by taking advantage of the special structure of the $\mathbf{F}[\mathbf{x}(t_i^+)]$ matrix in the Advanced CIRIS filter. As indicated in Appendix A, Tables A.7 through A.9, the the majority of the $\mathbf{F}$ matrix elements are constant, most of them zero. Since all of the time–varying elements are contained in the upper left 28–by–28 submatrix, only this submatrix should be stored at each measurement time.[1] The remaining 42, constant, non–zero, diagonal elements need be saved only once. This alternative procedure reduces the required $\mathbf{F}$ matrix storage at each measurement time to 784 64–bit data words and reduces the total (unformatted) storage requirement for the one hour interval to 170 megabytes.

[1]For even greater reductions, *only* the time varying elements should be stored. This would require a slight increase in the complexity of the storage procedure.

The other costly aspect of the proposed smoother algorithm is computation time. In addition to the normal matrix arithmetic, the procedure requires a matrix inversion and a matrix exponential for each measurement time. A search of available references did not reveal any special procedures for finding the symmetric inverse of a symmetric matrix using only the upper triangle of the matrix. Numerical procedures exist for computing matrix exponentials [5], but they must be carefully implemented to ensure accurate results. In the case of Advanced CIRIS, the block diagonal structure of the **F** matrix simplifies calculation of the state transition matrix. Because the lower right 42–by–42 submatrix is constant and diagonal, the exponential of this submatrix is simply another constant, diagonal, submatrix formed by exponentiating each of the original diagonal elements. The exponential of the upper left 28–by–28 submatrix may be calculated using the algorithm described in reference [5:396–400]. The remaining (upper right and lower left) submatrices are identically zero so their exponentials are also zero. Care must be taken to ensure numerically accurate results at each step in the backward recursion. Since the non–recursive calculation of the *smoothing estimator gain matrix depends only on the previously recorded data* for each measurement time, this calculation is not subject to the cumulative effects of round–off error. However, the recursive calculations of the smoothed state estimates and smoothed covariance matrices are subject to such cumulative effects.

The adaptation of a discrete–time smoothing algorithm to a continuous–time problem contains the implicit assumption that the dynamic matrix **F** is relatively constant over the time interval between measurements. If this assumption is not true, then the state transition matrix calculated at each measurement time will fail to represent the actual state dynamics between measurement times. With typical CIRIS data, the measurements occur about one second apart, but there is no absolute upper bound on this. Since the time varying eigenvalues of the Advanced CIRIS dynamics matrix all have time constants greater than about 42 minutes (half the Schuler period), and the rate of change of these eigenvalues is relatively slow for cargo type aircraft [7], the assumption that **F** is essentially constant seems resonable. Another area of concern is whether or not the proposed fixed–interval smoothing algorithm is compatible with the ad hoc procedure described in Chapter III for the time–sharing of transponder error states. It is not readily apparent that the backward

recursion can proceed correctly when the forward pass covariance matrix is discontinuous at times t_i^-. Until this is resolved, the smoothing algorithm should not be used in conjunction with time–shared transponder error states.

6.3 Summary

This chapter introduces the concept of a *fixed–interval smoother* as an optimal estimator based on a separate forward–pass and backward–pass filters. An adaptation of simple discrete–time dynamics formulation for the backward–pass filter is proposed for use with the continuous–time dynamics model in the forward–pass Advanced CIRIS filter. The reason for this is to avoid the computational complexity of a true continuous–time dynamics backward–pass filter.[2] Because the backward pass requires use of large amounts of data stored during the forward pass, use of the smoother for very long data sets may not be practical due to disk storage limitations. The proposed smoother was not implemented in this thesis effort due to lack of time, but it holds promise as a means of achieving additional estimation accuracy beyond that of the Advanced CIRIS filter alone.

[2]MSOFE itself does not provide the subroutines necessary to implement backward pass filters.

VII. Conclusions and Recommendations

This chapter restates the major goals of this thesis effort, evaluates progress made towards these goals, and provides recommendations for further research regarding the Advanced CIRIS filter.

7.1 Conclusions

The first goal is to improve the structure and utility of the MSOFE–based software which implements the filter described in this thesis. Although the preceding chapters do not specifically address the filter software in detail, it is the software which consumed the majority of the effort required for this research. The software developed by Solomon [13] was procedurally correct but contained numerous embedded constants unique to the CIRIS data set used in his research. This software was completely rewritten to eliminate most embedded constants, allow tuning parameters to be changed without recompiling, increase modularity, and greatly simplify control structures.

The second and primary goal is to evaluate, using real CIRIS data, the performance of a refined version of the 70–state filter developed by Solomon. Refinements to the filter include modeling the range measurement errors due to atmospheric propagation delays as being range dependent, modeling the cross–correlation of the atmospheric error driving noises for different transponders, and using barometric–altitude measurements. The development of the range and range–rate measurement error models is reaccomplished to illustrate the procedure for compensating for the offset between the interrogator antenna and the INS. The filter performance was evaluated using two separate data sets.

The first data set came from a series of slow speed ground tests. The reason for using this data is the availability of independent position and velocity measurements provided by the track data acquisition system (TDAS). In addition to evaluating model validity by analysis of residual characteristics, these independent measurements are considered accurate enough to justify the adjustment of filter tuning parameters in order to minimize the differences between the filter position/velocity estimates and the TDAS measurements. However, the poor geometry of the usable transponders relative to the vehicle trajectory

limited the observability of most filter error states. This was apparent by the filter-calculated error state variances remaining relatively large throughout the test. Use of this data did indicate that modeling the baro-altitude error with three separate states, as is suggested in the Litton LN-39 Systems Engineering Report, is overly complex for nearly constant altitude trajectories. For the particular track run discussed in Chapter IV, the peak position estimation errors, relative to the track measurements, were 12 feet in latitude, 17 feet in longitude, and 29 feet in altitude. In retrospect, the time spent trying to tune the filter using this data set was excessive considering the observability problems. However, use of this data did provide insights regarding the validity of the error model on which the filter is based.

The second data set came from a C-141 flight. This flight involved many maneuvers at different altitudes so, except for certain transponder position errors, there are no observability problems inherent in the recorded measurements. The reason for using this data is the availability of independent position and velocity measurements provided by a laser ranging system (LRS). The results from this data set more are difficult to interpret. For the Advanced CIRIS filter, the baro-altimeter and transponder range measurement residuals appear "white," zero-mean, with true variance near the filter-predicted variance. The transponder range-rate measurement residuals are near zero-mean, but they exhibit some time correlation and their actual variance is larger than the filter-predicted variance. The large residuals are likely correlated with aircraft turns, but more analysis is needed to prove this. The most likely explanation is that the range-rate measurements are not made instantaneously; they represent an average range-rate over a short (1 second or less) time interval. However, the "Advanced" CIRIS filter models them as instantaneous.

The comparison of the Advanced CIRIS filter position and velocity estimates to the LRS measurements provides encouraging results but also raises questions about the comparison process. The filter latitude estimate, though biased, differs from the laser data less than 15 feet during most of the flight. The filter longitude estimate, also biased and quite noisy, differs from the laser data less than 20 feet during most of the flight. The filter altitude estimate, again biased and noisy, differs from the laser data less than 35 feet during most of the flight. The filter north, west, and up velocity estimation errors

are all near zero–mean with most errors in the range +3 to −3 *fps*. However all six plots, especially the velocity difference plots, exhibit large spikes.

The laser measurement data file provides latitude, longitude, altitude, and the three velocities at each laser measurement time. The measurements at each time are provided by the *single* laser instrument closest to the aircraft [7]. The LRS data file is thus a sequence of groups of position and velocity measurements provided by different laser instruments. Since there is no averaging or filtering of the LRS data, the position and velocity measurements may change by relatively large amounts when the laser instrument is changed. In order to make the position and velocity comparisons, the laser measurements must be interpolated at the filter measurement times. The use of cubic splines to interpolate discontinuous data frequently results in erroneous cubic (polynomial) oscillations at the points of discontinuity. If the interpolated data is resampled at an oscillation point, the result is erroneous. This is a possible cause of the spikes apparent in the difference plots.

The CIRIS II filter position estimates, velocity estimates, and transponder measurement residuals were available for this flight. This CIRIS II data was compared to the LRS measurements to gain insight into the relative performance of CIRIS II and Advanced CIRIS. The CIRIS II range residuals exhibit constant biases and significantly *larger* variance than those of the Advanced CIRIS filter. The CIRIS II range–rate residuals exhibit constant biases but they have a much *smaller* variance than those of the Advanced CIRIS filter. The presence of the transponder position error states in the Advanced CIRIS filter is the probable reason for the absence of biases in its residuals. The problem with the large variance of the Advanced CIRIS range–rate measurement residuals appears to be a modeling problem rather than a parameter tuning problem.

The comparison of the CIRIS II position and velocity estimates to the LRS measurements shows the CIRIS II position errors to be larger than those of Advanced CIRIS while the velocity errors appear very similar. The CIRIS II/LRS difference plots exhibit spikes similar to the ones in the Advanced CIRIS/LRS difference plots.

In general, the performance of the Advanced CIRIS filter is better than that of the current CIRIS II filter. The exception is in the range–rate measurement processing. The

Advanced CIRIS filter range–rate measurement residuals are unacceptably large during aircraft maneuvers, resulting in an excessive percentage of range–rate measurements being rejected by the filter.

The third goal was the development of a fixed–interval smoothing procedure compatible with the MSOFE–based Advanced CIRIS filter. The description of such a procedure is given in Chapter VI, but it was not implemented and tested due to a shortage of time to work on it. The implementation of this procedure will be significantly more difficult than simply proposing it. The primary obstacles are the large amounts of disk storage required and the need to ensure compatability with the state switching routine implemented in the Advanced CIRIS filter.

7.2 Recommendations

The following recommendations are divided into three categories: software development, the need for additional data, and directions for future research.

7.2.1 Software Development The research described in this thesis required the development of a significant amount of software. In addition to the MSOFE user–subroutines which implement the Advanced CIRIS filter, there are several small utility programs needed for data file manipulation, $MATRIX_X$ programs for making plots, and operating system command files for running batch jobs and recompiling the filter subroutines. Yet, the development of software is not the main focus of the research. The main focus is the function and performance of the software: the Kalman filter. However, it is the author's firm opinion that software functionality and performance cannot be truly achieved in the absence of thoughtful design, implementation, and maintenance of the software. The recommendation is that future student researchers be encouraged and given credit for devoting a larger portion of their efforts to developing software that is robust, documented, and easily modified.

7.2.2 Data Problems The use of empirical data in this research, though necessary to validate the correctness of the filter model, presented many problems and required the use

of certain approximations. The data tapes (CIRIS, laser, track) contained a small number of data dropouts, duplicate records, and obviously erroneous data values. The presence of these occasional bad records cannot always be ignored; they must be located and either "patched" or skipped. Given the huge size of the data files, this is a time–consuming task.

Even more troublesome than bad data records, certain information required by the analytic description of the filter model is simply unavailable on the data tapes. The three items in this category are the raw INS accelerometer outputs, barometric altitude rate, and aircraft attitude rates. The accelerometer outputs are available from the INS computer and attempts have been made to record them, but the great majority of the recorded acceleration values are *zero* [11]. This is possibly due to a timing problem in the recording process. In the absence of this information, platform frame accelerations must be "reverse engineered" (synthesized) from the recorded INS velocities and other recorded information. The result is acceleration data that is representative of the true *average* acceleration between sampling times. Since this acceleration information is used only in defining the INS error state dynamics matrix for propagation of the INS error state estimates, and is not a direct measurement to the filter, the use of consistent, synthesized accelerations should have a negligible impact on filter performance. The recommendation is to investigate why the raw accelerometer outputs cannot be reliably recorded and correct the problem.

The barometric altitude rate ($\dot{h}_b$) is needed only for filter emulation of the internal INS calculation of the vertical channel aiding gains, as described in Chapter III. However, this rate data is not recorded (it may not be directly available from the CADC) so it must be synthesized by differencing consecutive barometric altitude measurements and dividing by the measurement interval. This explains the appearance of the baro–altitude rate plot in Figure B.6. The recommendation is to continue this procedure at a higher sampling rate (ideally, the same sampling rate used by the INS) or, if available, directly record the aiding gain values as calculated by the INS.

The aircraft attitude rates ($\dot{\psi}$, $\dot{\theta}$, $\dot{\phi}$) are needed to calculate the transformation matrices for use in the lever–arm compensation procedures for the range–rate measurements. These three quantities are not available on the data tape, so they must be synthesized by

differencing consecutive attitude angles and dividing by the sampling interval. The recommendation is to continue this procedure at a higher sampling rate or to directly record the attitude rates if they are available from the INS.

7.2.3 Future Research For reasons discussed in the preface, the scope of this research overlapped that of Solomon [13] to a great extent. Differences include the analytic development of the lever arm compensation procedure, the analytic description of the filter measurement model using extended Kalman filter notation, modification of the atmospheric propagation delay error model, and the use of two additional real data sets, with independent position/velocity measurements, to evaluate filter performance. As a result of this additional work, the concept of the Advanced CIRIS filter has been more completely characterized and tested, and so it has greater potential for "operational" use, should CIGTF desire to use it. The filter software is now structured well enough to be a good starting point for continued research at both CIGTF and AFIT.

Qualitatively, the performance of the Advanced CIRIS filter is sufficiently greater than that of the CIRIS II filter to warrant further development. This improvement is primarily due to the filter structure (additional observable states, more accurate propagation and update algorithms) since the filter initial covariance values and atmospheric error model parameters are not yet particularly well tuned. The effort to tune filter parameters precisely and quantify filter estimation accuracy should be continued at CIGTF instead of at AFIT because of the availability of additional data sets and other necessary resources. As an aid in this tuning process, it would be useful to collect additional CIRIS data from tests designed to achieve high observability of specific error states. The key to correctly modeling the atmospheric delay errors is availability of power spectral density (and cross spectral density) information. Such information is most easily collected from a long duration static test involving several carefully placed transponders sampled at a high (0.1—1.0 Hz), uniform sampling rate.

Further research at AFIT should focus on two areas: use of Global Positioning System (GPS) data and implementation of a fixed-interval smoother. The incorporation of GPS, particularly differential GPS, measurements into the Advanced CIRIS filter should

be pursued first. The development of a complete, correct error model for differential GPS measurements promises to be the single most effective way to increase the estimation accuracy of the filter. The Advanced CIRIS/GPS filter should have the capacity to process GPS range and range–rate measurements from at least four different satellites, but preferably from all satellites whose measurements are recorded. One of the great advantages of an MSOFE based filter is the ability to quickly reconfigure the filter dimension (state vector length) to provide exactly the right number of error states required for the number of transponders or satellites used in a particular data set.[1] The development of the Advanced CIRIS/GPS filter should conclude with a performance evaluation using real data. However, much of the initial development could be accomplished using MSOFE's Monte Carlo simulation mode. Initial development using Monte Carlo simulation would avoid the previously mentioned pitfalls associated with empirical data.

The implementation of a fixed–interval smoother, either the one described in Chapter VI or one based on an extensively modified version of MSOFE, should be undertaken to determine the potential increase in estimation accuracy over the stand–alone, forward–pass filter. In either case, *initial* development should use Monte Carlo simulation to permit a precise, quantitative assessment on the accuracy of the smoothed estimates versus the forward–pass estimates. The development of a fixed–interval smoothing capability for MSOFE would be an extremely useful achievement, but this is a topic worthy of an independent thesis effort. If attempted, it should be done in close cooperation with the authors of MSOFE.

[1]This is the optimal alternative to the ad hoc state sharing procedure currently used with the transponders, but it may result in a large state vector length.

Appendix A. *Initial Covariance Values and Filter Matrix Definitions*

Table A.1. Non–Zero Elements of $\mathbf{P}_0$

Element	State	Definition	Value (1σ)
1,1	$\delta\Theta_X$	Magnitude of error between the true frame's X axis and the computer frame's X axis.	50 *arcsecs*
2,2	$\delta\Theta_Y$	Magnitude of error between the true frame's Y axis and the computer frame's Y axis.	50 *arcsecs*
3,3	$\delta\Theta_Z$	Magnitude of error between the true frame's Z axis and the computer frame's Z axis.	50 *arcsecs*
4,4	ϕ_X	Magnitude of error between the true frame's X axis and the platform frame's X axis.	100 *arcsecs*
5,5	ϕ_Y	Magnitude of error between the true frame's Y axis and the platform frame's Y axis.	100 *arcsecs*
6,6	ϕ_Z	Magnitude of error between the true frame's Z axis and the platform frame's Z axis.	180 *arcmins*
7,7	δV_X	Magnitude of error between the true frame X velocity and the computer frame X velocity.	1.0 ft/sec
8,8	δV_Y	Magnitude of error between the true frame Y velocity and the computer frame Y velocity.	1.0 ft/sec
9,9	δV_Z	Magnitude of error between the true frame Z velocity and the computer frame Z velocity.	1.0 ft/sec
10,10	δh	Magnitude of error between the true altitude and the computer altitude.	100 ft
11,11	δh_l	Magnitude of error between the true altitude and the computer altitude (1 sec delay).	100 ft
12,12	δS_3	Magnitude of vertical channel aiding state.	1 ft
13,13	δS_4	Magnitude of vertical channel aiding state.	1 ft/sec^2
All other elements are zero.			

Table A.2. Non–Zero Elements of $\mathbf{P}_0$, Continued

Element	State	Definition	Value (1σ)
14,14	B_{X_c}	Magnitude of gyro correlated drift rate along X axis.	0.002 deg/hr
15,15	B_{Y_c}	Magnitude of gyro correlated drift rate along Y axis.	0.002 deg/hr
16,16	B_{Z_c}	Magnitude of gyro correlated drift rate along Z axis.	0.005 deg/hr
17,17	∇_{X_c}	Magnitude of accelerometer and velocity quantizer correlated noise along X axis.	3 μg
18,18	∇_{Y_c}	Magnitude of accelerometer and velocity quantizer correlated noise along Y axis.	3 μg
19,19	∇_{Z_c}	Magnitude of accelerometer and velocity quantizer correlated noise along Z axis.	3 μg
20,20	δG_X	Magnitude of gravity vector error along X axis.	35 μg
21,21	δG_Y	Magnitude of gravity vector error along Y axis.	35 μg
22,22	δG_Z	Magnitude of gravity vector error along Z axis.	35 μg
23,23	B_X	Magnitude of gyro drift rate bias repeatability along X axis.	0.0045 deg/hr
24,24	B_Y	Magnitude of gyro drift rate bias repeatability along Y axis.	0.0045 deg/hr
25,25	B_Z	Magnitude of gyro drift rate bias repeatability along Z axis.	0.01 deg/hr
All other elements are zero.			

Table A.3. Non–Zero Elements of $\mathbf{P}_0$, Continued

Element	State	Definition	Value (1σ)
26,26	δh_{b1}	Magnitude of baro–altimeter correlated bias noise.	100 ft
27,27	δh_{b2}	Magnitude of baro–altimeter constant bias error.	100 ft
28,28	δh_{b3}	Magnitude of baro–altimeter scale factor error.	4 %
All other elements are zero.			

Table A.4. Non-Zero Elements of $\mathbf{P}_0$, Continued

Element	State	Definition	Value (1σ)
29,29	δE_{rc}	Magnitude of the transponder interogator range measurement calibration error.	1 ft
30,30	$\delta E_{\dot{r}c}$	Magnitude of the transponder interogator range-rate measurement calibration error.	0.01 ft/sec
31,31	δX_{T_1}	Magnitude of transponder 1 position error (X^E axis).	5 ft
32,32	δY_{T_1}	Magnitude of transponder 1 position error (Y^E axis).	5 ft
33,33	δZ_{T_1}	Magnitude of transponder 1 position error (Z^E axis).	5 ft
34,34	δA_{T_1}	Magnitude of transponder 1 atmospheric scale factor error (line-of-sight).	10 ppm
35,35	δX_{T_2}	Magnitude of transponder 2 position error (X^E axis).	5 ft
36,36	δY_{T_2}	Magnitude of transponder 2 position error (Y^E axis).	5 ft
37,37	δZ_{T_2}	Magnitude of transponder 2 position error (Z^E axis).	5 ft
38,38	δA_{T_2}	Magnitude of transponder 2 atmospheric scale factor error (line-of-sight).	10 ppm
39,39	δX_{T_3}	Magnitude of transponder 3 position error (X^E axis).	5 ft
40,40	δY_{T_3}	Magnitude of transponder 3 position error (Y^E axis).	5 ft
41,41	δZ_{T_3}	Magnitude of transponder 3 position error (Z^E axis).	5 ft
42,42	δA_{T_3}	Magnitude of transponder 3 atmospheric scale factor error (line-of-sight).	10 ppm

Table A.5. Non–Zero Elements of $\mathbf{P}_0$, Continued

Element	State	Definition	Value (1σ)
43,43	δX_{T_4}	Magnitude of transponder 4 position error (X^E axis).	5 ft
44,44	δY_{T_4}	Magnitude of transponder 4 position error (Y^E axis).	5 ft
45,45	δZ_{T_4}	Magnitude of transponder 4 position error (Z^E axis).	5 ft
46,46	δA_{T_4}	Magnitude of transponder 4 atmospheric scale factor error (line–of–sight).	10 ppm
47,47	δX_{T_5}	Magnitude of transponder 5 position error (X^E axis).	5 ft
48,48	δY_{T_5}	Magnitude of transponder 5 position error (Y^E axis).	5 ft
49,49	δZ_{T_5}	Magnitude of transponder 5 position error (Z^E axis).	5 ft
50,50	δA_{T_5}	Magnitude of transponder 5 atmospheric scale factor error (line–of–sight).	10 ppm
51,51	δX_{T_6}	Magnitude of transponder 6 position error (X^E axis).	5 ft
52,52	δY_{T_6}	Magnitude of transponder 6 position error (Y^E axis).	5 ft
53,53	δZ_{T_6}	Magnitude of transponder 6 position error (Z^E axis).	5 ft
54,54	δA_{T_6}	Magnitude of transponder 6 atmospheric scale factor error (line–of–sight).	10 ppm
55,55	δX_{T_7}	Magnitude of transponder 7 position error (X^E axis).	5 ft
56,56	δY_{T_7}	Magnitude of transponder 7 position error (Y^E axis).	5 ft
57,57	δZ_{T_7}	Magnitude of transponder 7 position error (Z^E axis).	5 ft
58,58	δA_{T_7}	Magnitude of transponder 7 atmospheric scale factor error (line–of–sight).	10 ppm

Table A.6. Non–Zero Elements of $\mathbf{P}_0$, Continued

Element	State	Definition	Value (1σ)
59,59	δX_{T_8}	Magnitude of transponder 8 position error (X^E axis).	5 *ft*
60,60	δY_{T_8}	Magnitude of transponder 8 position error (Y^E axis).	5 *ft*
61,61	δZ_{T_8}	Magnitude of transponder 8 position error (Z^E axis).	5 *ft*
62,62	δA_{T_8}	Magnitude of transponder 8 atmospheric scale factor error (line–of–sight).	10 *ppm*
63,63	δX_{T_9}	Magnitude of transponder 9 position error (X^E axis).	5 *ft*
64,64	δY_{T_9}	Magnitude of transponder 9 position error (Y^E axis).	5 *ft*
65,65	δZ_{T_9}	Magnitude of transponder 9 position error (Z^E axis).	5 *ft*
66,66	δA_{T_9}	Magnitude of transponder 9 atmospheric scale factor error (line–of–sight).	10 *ppm*
67,67	$\delta X_{T_{10}}$	Magnitude of transponder 10 position error (X^E axis).	5 *ft*
68,68	$\delta Y_{T_{10}}$	Magnitude of transponder 10 position error (Y^E axis).	5 *ft*
69,69	$\delta Z_{T_{10}}$	Magnitude of transponder 10 position error (Z^E axis).	5 *ft*
70,70	$\delta A_{T_{10}}$	Magnitude of transponder 10 atmospheric scale factor error (line–of–sight).	10 *ppm*
All other elements are zero.			

Table A.7. Non-Zero Elements of **F**

Element	Symbol or Formula	Value
1,3	$-\omega_{EPY}$	†
1,8	$-C_{RY}$	†
2,3	ω_{EPX}	†
2,7	C_{RX}	†
3,1	ω_{EPY}	†
3,2	$-\omega_{EPX}$	†
4,2	$-\omega_{IEZ}$	†
4,3	ω_{IEY}	†
4,5	ω_{IPZ}	†
4,6	$-\omega_{IPY}$	†
4,8	$-C_{RY}$	†
4,14	1.0	1.0
4,24	1.0	1.0
5,1	ω_{IEZ}	†
5,3	$-\omega_{IEX}$	†
5,4	ω_{IPZ}	†
5,6	$-\omega_{IPY}$	†
5,7	C_{RX}	†
5,15	1.0	1.0
5,25	1.0	1.0
6,1	$-\omega_{IEY}$	†
6,2	ω_{IEX}	†
6,4	ω_{IPY}	†
6,5	$-\omega_{IPX}$	†
6,16	1.0	1.0
6,26	1.0	1.0
7,1	$-2(V_Y\,\omega_{IEY} + V_Z\,\omega_{IEZ})$	†
7,2	$2(V_Y\,\omega_{IEX})$	†
7,3	$2(V_Z\,\omega_{IEX})$	†
7,5	$-A_Z$	†
7,6	A_Y	†
7,7	$-V_Z C_{RX}$	†
7,8	$2\,\omega_{IEZ}$	†
7,9	$-(\omega_{EPY} + 2\,\omega_{IEY})$	†
7,17	1.0	1.0
7,20	1.0	1.0
† time and/or trajectory dependent		

Table A.8. Non–Zero Elements of **F**, Continued

Element	Symbol or Formula	Value
8,1	$2\,V_X\,\omega_{IEY}$	†
8,2	$-2(\,V_X\,\omega_{IEX} + V_Z\,\omega_{IEZ})$	†
8,3	$2\,V_Z\,\omega_{IEY}$	†
8,4	A_Z	†
8,6	$-A_X$	†
8,7	$-2\,\omega_{IEZ}$	†
8,8	$-V_Z\,C_{RY}$	†
8,9	$\omega_{EPX} + 2\,\omega_{IEX}$	†
9,1	$2\,V_X\,\omega_{IEZ}$	†
9,2	$2\,V_Y\,\omega_{IEZ}$	†
9,3	$-2(\,V_Y\,\omega_{IEY} + V_X\,\omega_{IEX})$	†
9,4	$-A_Y$	†
9,5	A_X	†
9,7	$\omega_{EPY} + 2\,\omega_{IEY} + V_X\,C_{RX}$	†
9,8	$-\omega_{EPX} - 2\,\omega_{IEY} + V_Y\,C_{RY}$	†
9,10	$2\,G_0/A$	†
9,11	$-K_2$	†
9,12	-1.0	†
9,13	K_2	†
9,19	1.0	1.0
9,22	1.0	1.0
9,23	K_2	†
9,27	K_2	†
9,28	$h\,K_2$	†
10,9	1.0	1.0
10,11	$-K_1$	†
10,13	$K_1 - 1.0$	†
10,23	K_1	†
10,27	K_1	†
10,28	$h\,K_1$	†
11,10	1.0	1.0
11,11	-1.0	-1.0
12,11	K_3	†
12,13	$-K_3$	†
12,23	$-K_3$	†
12,27	$-K_3$	†
12,28	$-h\,K_3$	†
† time and/or trajectory dependent		

Table A.9. Non-Zero Elements of **F**, Continued

Element	Symbol or Formula	Value
13,10	K_4	†
13,11	$-K_4$	†
13,13	$K_4 - 1.0$	†
13,23	$K_4 \beta_{\delta h_c}$	†
13,28	$-K_4 V_Z$	†
14,14	$-\beta_{B_{X_c}}$	-1/300 (s^{-1})
15,15	$-\beta_{B_{Y_c}}$	-1/300 (s^{-1})
16,16	$-\beta_{B_{Z_c}}$	-1/300 (s^{-1})
17,17	$-\beta_{\nabla_{X_c}}$	-1/600 (s^{-1})
18,18	$-\beta_{\nabla_{Y_c}}$	-1/600 (s^{-1})
19,19	$-\beta_{\nabla_{Z_c}}$	-1/600 (s^{-1})
20,20	$-\beta_{\delta G_X}$	†
21,21	$-\beta_{\delta G_Y}$	†
22,22	$-\beta_{\delta G_Z}$	†
23,23	$-\beta_{\delta h_c}$	-1/600 (s^{-1})
34,34	$-1/\tau_{a1}$	-1/300 (s^{-1})
38,38	$-1/\tau_{a2}$	-1/300 (s^{-1})
42,42	$-1/\tau_{a3}$	-1/300 (s^{-1})
46,46	$-1/\tau_{a4}$	-1/300 (s^{-1})
50,50	$-1/\tau_{a5}$	-1/300 (s^{-1})
54,54	$-1/\tau_{a6}$	-1/300 (s^{-1})
58,58	$-1/\tau_{a7}$	-1/300 (s^{-1})
62,62	$-1/\tau_{a8}$	-1/300 (s^{-1})
66,66	$-1/\tau_{a9}$	-1/300 (s^{-1})
70,70	$-1/\tau_{a10}$	-1/300 (s^{-1})
† time and/or trajectory dependent		

Table A.10. Non–Zero Elements of **Q**

Element	Symbol or Formula	Value
4,4	$\sigma^2_{\eta_{Bx}}$	$9.4 \cdot 10^{-17}\ (s^{-1})$
5,5	$\sigma^2_{\eta_{By}}$	$9.4 \cdot 10^{-17}\ (s^{-1})$
6,6	$\sigma^2_{\eta_{Bz}}$	$9.4 \cdot 10^{-17}\ (s^{-1})$
7,7	$\sigma^2_{\eta_{Ax}}$	$9.3 \cdot 10^{-9}\ (f^2/s^3)$
8,8	$\sigma^2_{\eta_{Ax}}$	$9.3 \cdot 10^{-9}\ (f^2/s^3)$
9,9	$\sigma^2_{\eta_{Ax}}$	$9.3 \cdot 10^{-9}\ (f^2/s^3)$
13,13	$2K_4^2\beta_{\delta h_c}\sigma^2_{\delta h_c}$	† (f^2/s^5)
14,14	$2\beta_{B_{Xc}}\sigma^2_{B_{Xc}}$	$4.2 \cdot 10^{-21}\ (s^{-3})$
15,15	$2\beta_{B_{Yc}}\sigma^2_{B_{Yc}}$	$4.2 \cdot 10^{-21}\ (s^{-3})$
16,16	$2\beta_{B_{Zc}}\sigma^2_{B_{Zc}}$	$2.6 \cdot 10^{-20}\ (s^{-3})$
17,17	$2\beta_{\nabla_{Xc}}\sigma^2_{\nabla_{Xc}}$	† (f^2/s^5)
18,18	$2\beta_{\nabla_{Yc}}\sigma^2_{\nabla_{Yc}}$	† (f^2/s^5)
19,19	$2\beta_{\nabla_{Zc}}\sigma^2_{\nabla_{Zc}}$	† (f^2/s^5)
20,20	$2\beta_{\delta G_X}\sigma^2_{\delta G_X}$	† (f^2/s^5)
21,21	$2\beta_{\delta G_Y}\sigma^2_{\delta G_Y}$	† (f^2/s^5)
22,22	$2\beta_{\delta G_Z}\sigma^2_{\delta G_Z}$	† (f^2/s^5)
23,23	$2\beta_{\delta h_c}\sigma^2_{\delta h_c}$	$33.3\ (f^2/s)$
34,34	$2\sigma^2_{a1}/\tau_{a1}$	$2 \cdot 10^{-10}/300\ (s^{-1})$
38,38	$2\sigma^2_{a2}/\tau_{a2}$	$2 \cdot 10^{-10}/300\ (s^{-1})$
42,42	$2\sigma^2_{a3}/\tau_{a3}$	$2 \cdot 10^{-10}/300\ (s^{-1})$
46,46	$2\sigma^2_{a4}/\tau_{a4}$	$2 \cdot 10^{-10}/300\ (s^{-1})$
50,50	$2\sigma^2_{a5}/\tau_{a5}$	$2 \cdot 10^{-10}/300\ (s^{-1})$
54,54	$2\sigma^2_{a6}/\tau_{a6}$	$2 \cdot 10^{-10}/300\ (s^{-1})$
58,58	$2\sigma^2_{a7}/\tau_{a7}$	$2 \cdot 10^{-10}/300\ (s^{-1})$
62,62	$2\sigma^2_{a8}/\tau_{a8}$	$2 \cdot 10^{-10}/300\ (s^{-1})$
66,66	$2\sigma^2_{a9}/\tau_{a9}$	$2 \cdot 10^{-10}/300\ (s^{-1})$
70,70	$2\sigma^2_{a10}/\tau_{a10}$	$2 \cdot 10^{-10}/300\ (s^{-1})$

† time and/or trajectory dependent

The *off-diagonal* elements indexed by all possible pairs of the form (i, j), $i \neq j$, selected from {34, 38, 42, 46, 50, 54, 58, 62, 66, 70} are calculated as

$$Q_{i,j} = \frac{2\rho\, \sigma_{ai}\sigma_{aj}}{\sqrt{\tau_{ai}\tau_{aj}}}$$

where ρ is the correlation coefficient. The value used for ρ is 0.8.

Table A.11. Non-Zero Elements of $\mathbf{H}_r$

Element	State	Formula
1,1	$\delta\Theta_X$	H'_1
1,2	$\delta\Theta_Y$	H'_2
1,10	δh	H'_3
1,29	δE_{rc}	1.0
$1,\#X_{T_j}$	δX_{T_j}	$+\frac{\widehat{X}_{T_j}-\widehat{X}_A}{\widehat{R}_j}$
$1,\#Y_{T_j}$	δY_{T_j}	$+\frac{\widehat{Y}_{T_j}-\widehat{Y}_A}{\widehat{R}_j}$
$1,\#Z_{T_j}$	δZ_{T_j}	$+\frac{\widehat{Z}_{T_j}-\widehat{Z}_A}{\widehat{R}_j}$
$1,\#A_{T_j}$	δA_{T_j}	$\widehat{R}_j$
All other elements are zero.		

NOTE 1: The $\mathbf{H}'$ transformation projects the INS position errors, as defined in the state vector, into the E-frame. This transformation is required because the range measurements are defined in terms of E-frame coordinates. The elements of $\mathbf{H}'$ are calculated as

$$\begin{bmatrix} \mathrm{H}'_1 & \mathrm{H}'_2 & \mathrm{H}'_3 \end{bmatrix} = \begin{bmatrix} -\frac{\widehat{X}_{T_j}-\widehat{X}_A}{\widehat{R}_j} & -\frac{\widehat{Y}_{T_j}-\widehat{Y}_A}{\widehat{R}_j} & -\frac{\widehat{Z}_{T_j}-\widehat{Z}_A}{\widehat{R}_j} \end{bmatrix} C_N^E \, T_X^N$$

where C_N^E is defined in Equation (2.10) and T_X^N is defined in Equation (3.5).

NOTE 2: The # symbol represents the number of the corresponding state in the 10 transponder window for the transponder being sampled at the applicable measurement update time.

Table A.12. Non-Zero Elements of $\mathbf{H}_{\dot{r}}$

Element	State	Formula
1,1	$\delta\Theta_X$	H''_1
1,2	$\delta\Theta_Y$	H''_2
1,10	δh	H''_3
1,7	δV_X	H''_4
1,8	δV_Y	H''_5
1,9	δV_Z	H''_6
1,30	$\delta E_{\dot{r}c}$	1.0
All other elements are zero.		

NOTE 1: The $\mathbf{H}''$ transformation projects the INS position and velocity errors, as defined in the state vector, into the E-frame. This transformation is required because the range-rate measurements are defined in terms of E-frame coordinates. The elements of $\mathbf{H}''$ are calculated as

$$\begin{bmatrix} \mathrm{H}''_1 & \mathrm{H}''_2 & \mathrm{H}''_3 \end{bmatrix} =$$

$$\Bigg[-\frac{(\hat{X}_{T_j}-\hat{X}_A)^2\hat{\dot{X}}_A + (\hat{X}_{T_j}-\hat{X}_A)(\hat{Y}_{T_j}-\hat{Y}_A)\hat{\dot{Y}}_A + (\hat{X}_{T_j}-\hat{X}_A)(\hat{Z}_{T_j}-\hat{Z}_A)\hat{\dot{Z}}_A - \hat{R}^2_{T_j}\hat{\dot{X}}_A}{\hat{R}^3_{T_j}},$$

$$-\frac{(\hat{Y}_{T_j}-\hat{Y}_A)(\hat{X}_{T_j}-\hat{X}_A)\hat{\dot{X}}_A + (\hat{Y}_{T_j}-\hat{Y}_A)^2\hat{\dot{Y}}_A + (\hat{Y}_{T_j}-\hat{Y}_A)(\hat{Z}_{T_j}-\hat{Z}_A)\hat{\dot{Z}}_A - \hat{R}^2_{T_j}\hat{\dot{Y}}_A}{\hat{R}^3_{T_j}},$$

$$-\frac{(\hat{Z}_{T_j}-\hat{Z}_A)(\hat{X}_{T_j}-\hat{X}_A)\hat{\dot{X}}_A + (\hat{Z}_{T_j}-\hat{Z}_A)(\hat{Y}_{T_j}-\hat{Y}_A)\hat{\dot{Y}}_A + (\hat{Z}_{T_j}-\hat{Z}_A)^2\hat{\dot{Z}}_A - \hat{R}^2_{T_j}\hat{\dot{Z}}_A}{\hat{R}^3_{T_j}} \Bigg] \boldsymbol{C}^E_N \boldsymbol{T}^N_X$$

and

$$\begin{bmatrix} \mathrm{H}''_4 & \mathrm{H}''_5 & \mathrm{H}''_6 \end{bmatrix} = \begin{bmatrix} -\frac{\hat{X}_{T_j}-\hat{X}_A}{\hat{R}_j} & -\frac{\hat{Y}_{T_j}-\hat{Y}_A}{\hat{R}_j} & -\frac{\hat{Z}_{T_j}-\hat{Z}_A}{\hat{R}_j} \end{bmatrix} \boldsymbol{C}^E_P$$

where $\boldsymbol{C}^E_N$ is defined in Equation (2.10), $\boldsymbol{T}^N_X$ is defined in Equation (3.5), and $\boldsymbol{C}^E_P$ is defined in Equation (2.11)

Table A.13. Non–Zero Elements of $\mathbf{H}_{h_b}$

Element	State	Formula
1,10	δh	-1.0
1,26	δh_{b1}	1.0
1,27	δh_{b2}	1.0
1,28	δh_{b3}	$\widehat{h}$
All other elements are zero.		

Table A.14. Non-Zero Elements of **R**

Element	Symbol or Formula	Value
1,1	σ_r^2	9.0 (f^2)
2,2	$\sigma_{\dot{r}}^2$	0.25 (f^2/s^2)
3,3	$\sigma_{h_b}^2$	9.0 (f^2)

In the MSOFE-based filter, R never appears as a 3-by-3 matrix. MSOFE's scalar update procedure sequentially uses the diagonal elements of the 3-by-3 **R** as three separate 1-by-1 **R** matrices.

Appendix B. *Recorded Data for Track Run E*

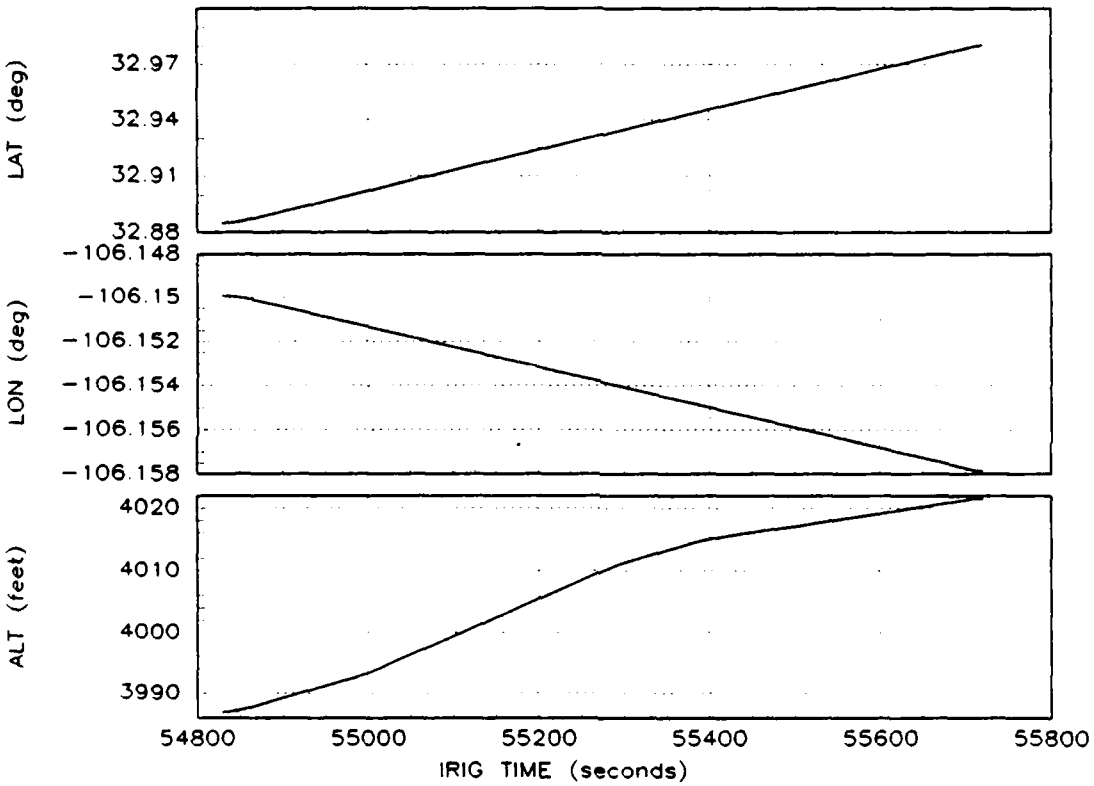

Figure B.1. TDAS Position, Track Run E

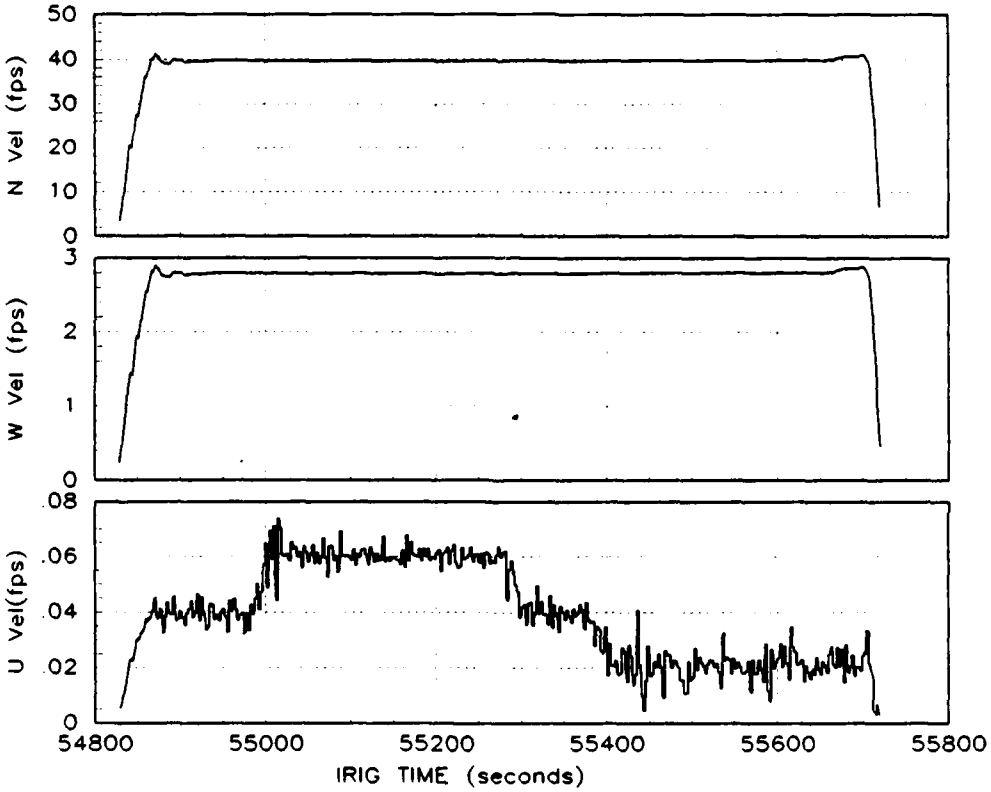

Figure B.2. TDAS Velocity, Track Run E

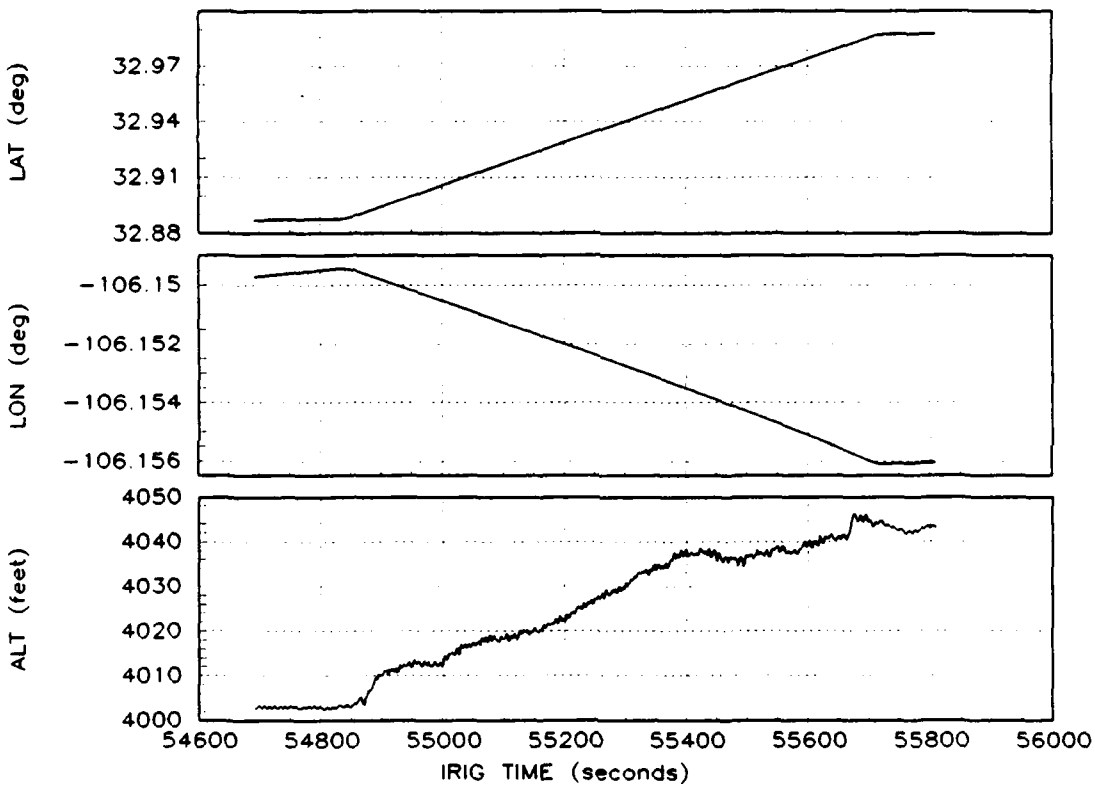

Figure B.3. INS Indicated Position, Track Run E

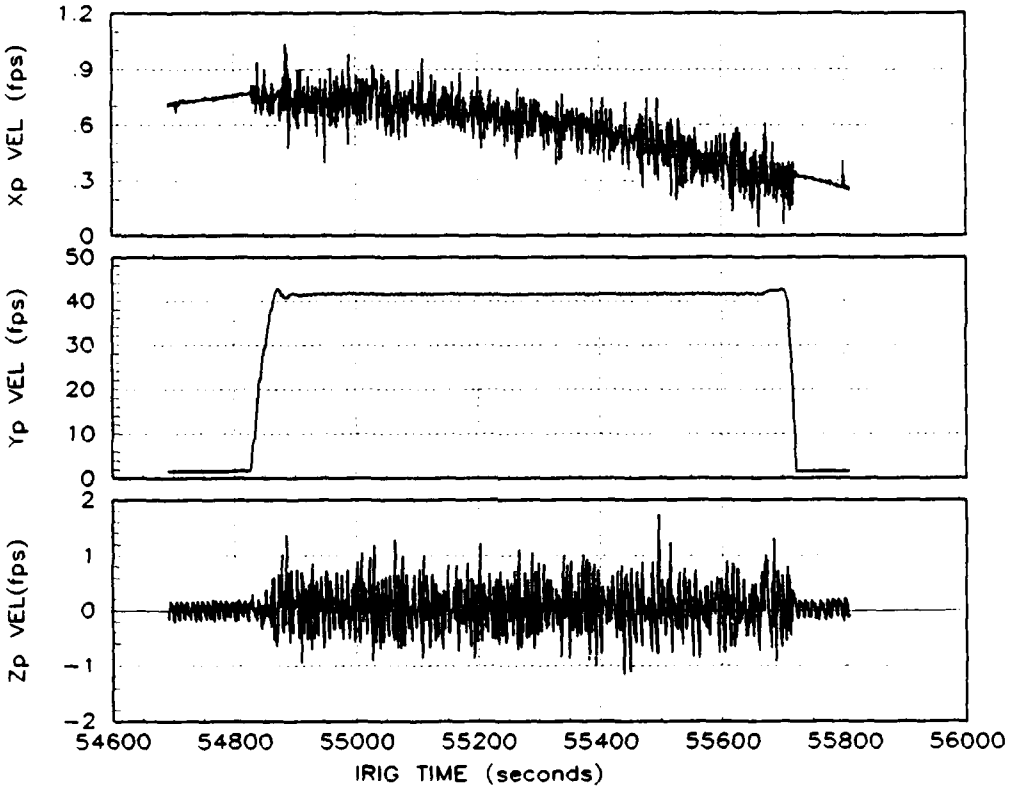

Figure B.4. INS Indicated Velocity, Track Run E

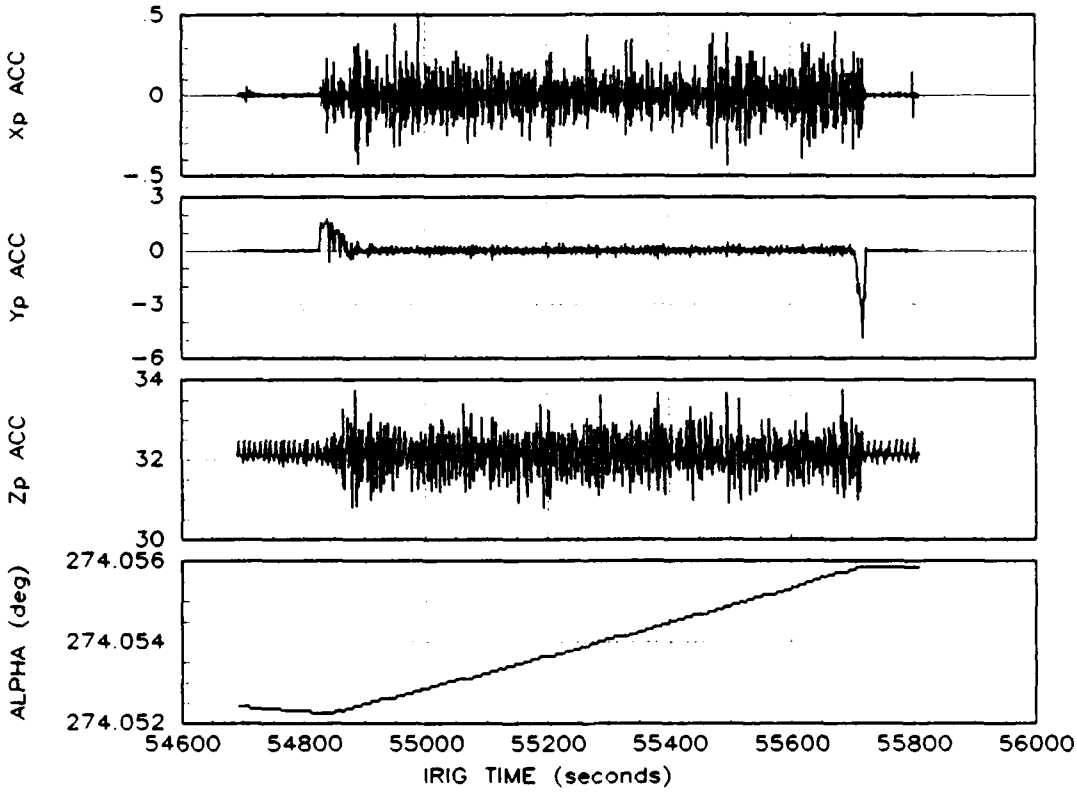

Figure B.5. INS Indicated Acceleration and Wander Angle, Track Run E

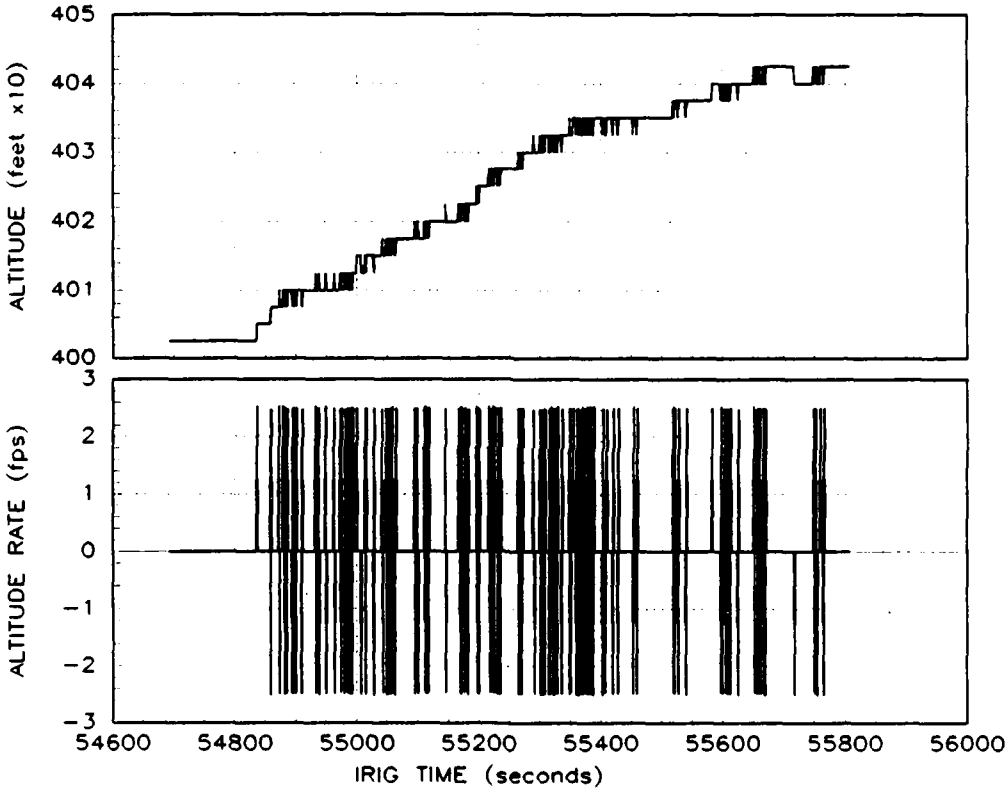

Figure B.6. Baro–altimeter Altitude and Altitude Rate, Track Run E

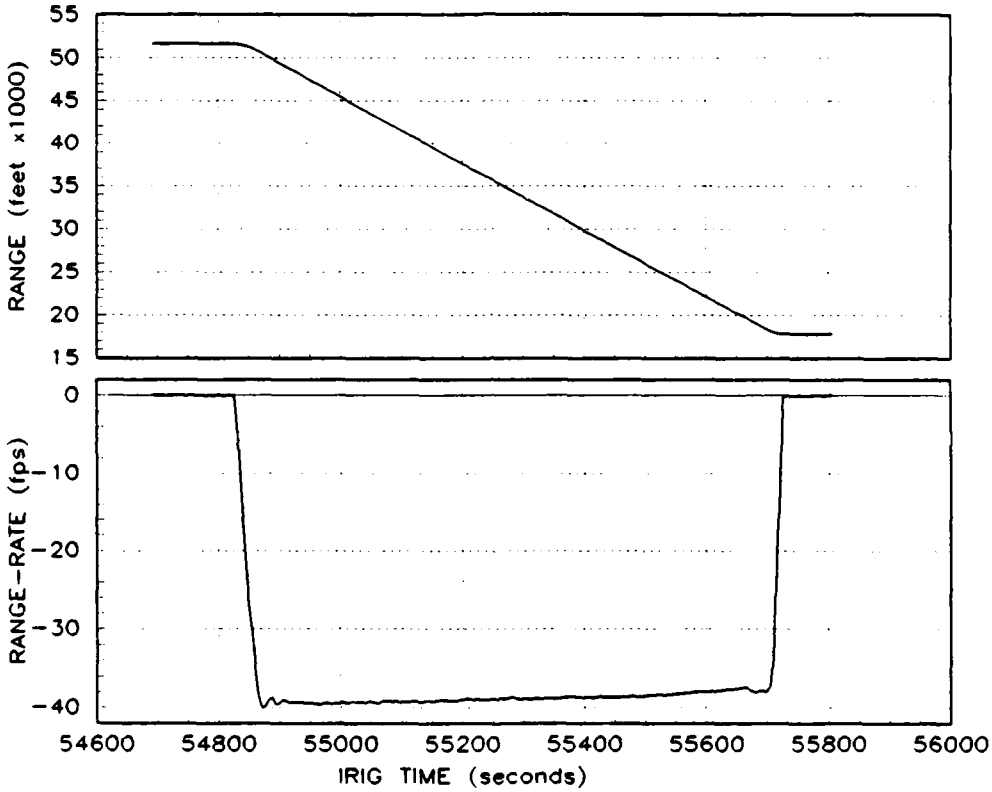

Figure B.7. Transponder 005 Range and Range–Rate, Track Run E

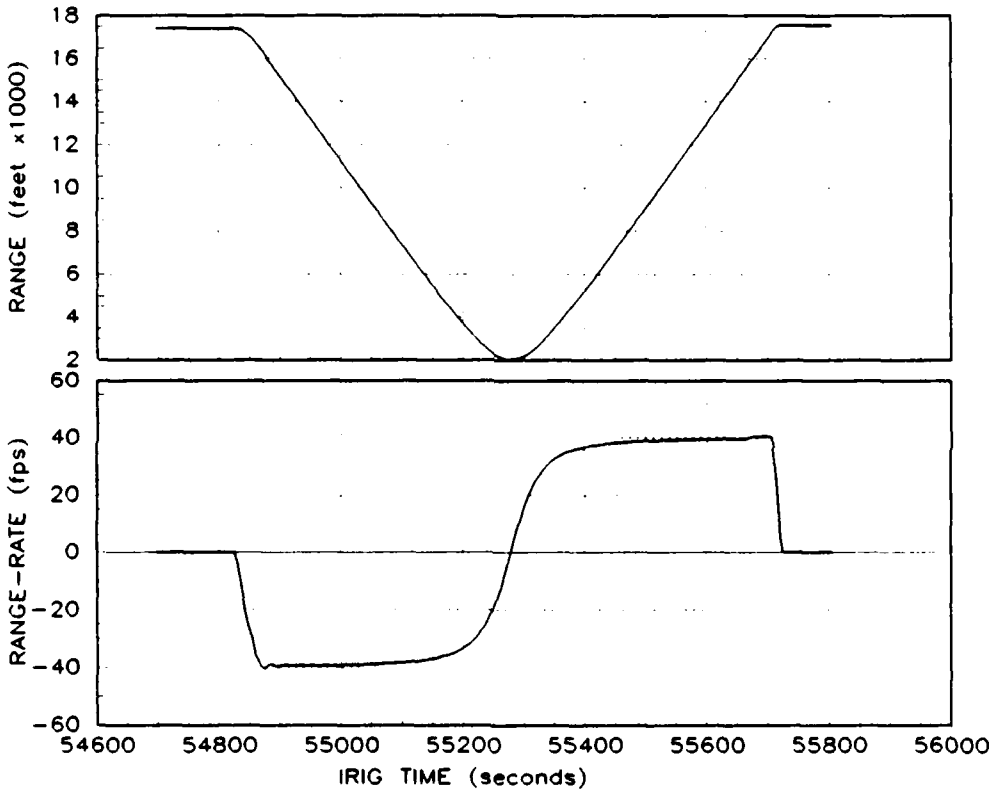

Figure B.8. Transponder 102 Range and Range-Rate, Track Run E

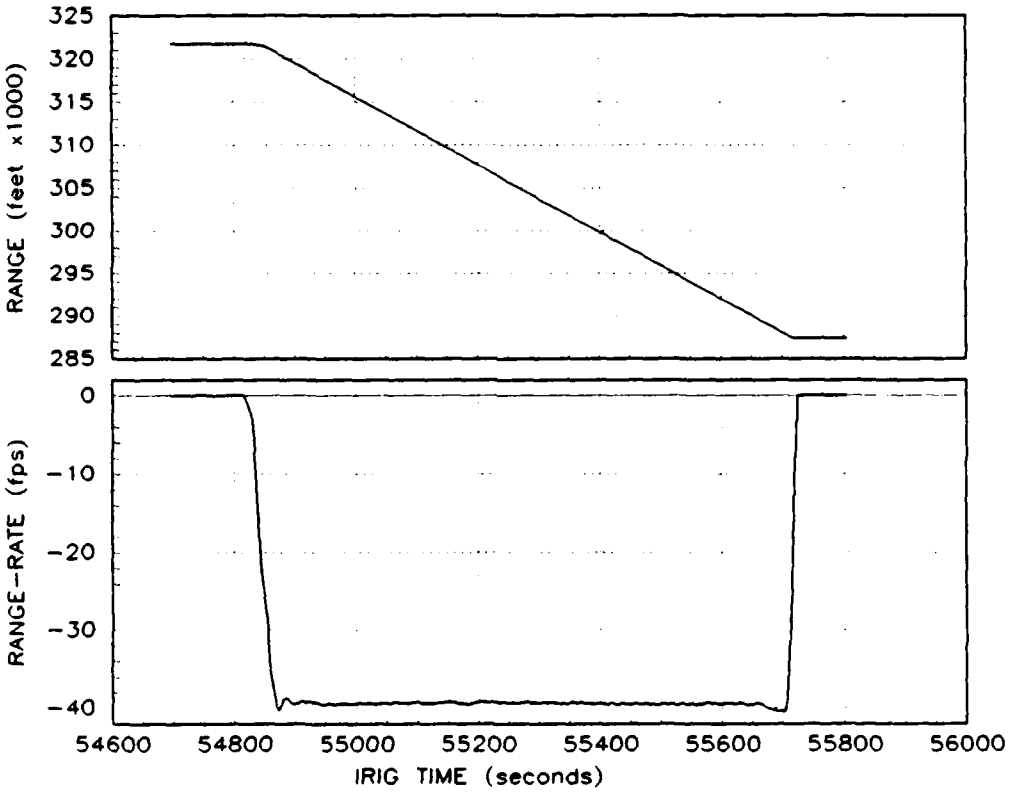

Figure B.9. Transponder 181 Range and Range–Rate, Track Run E

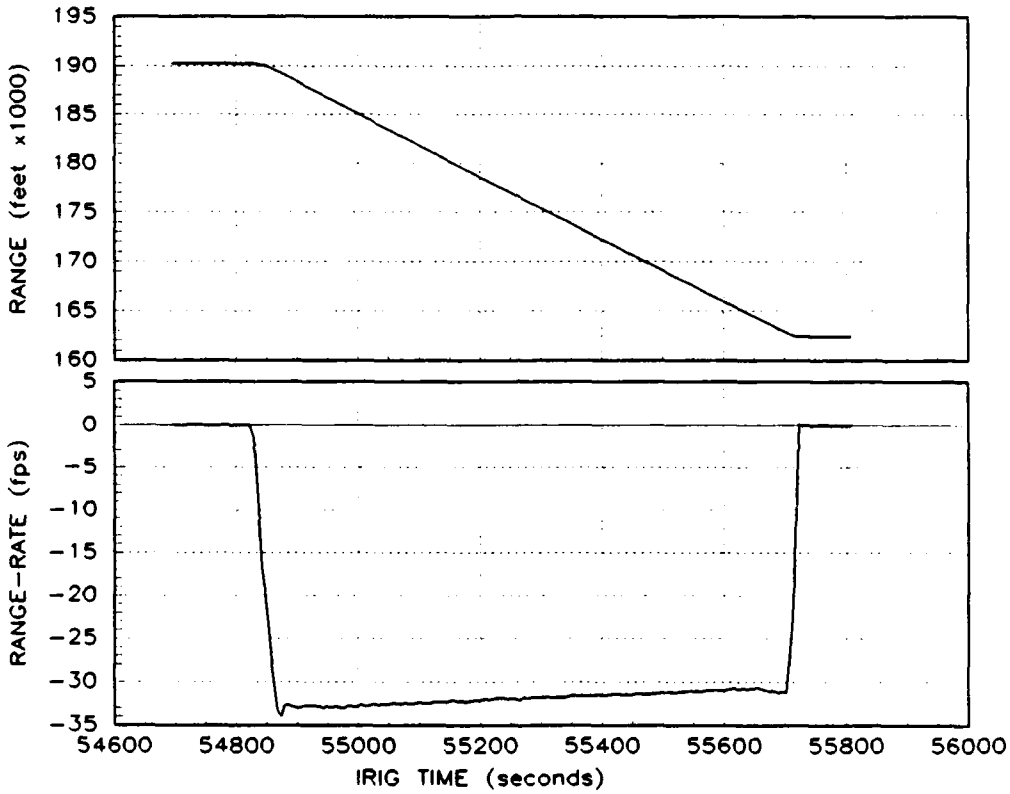

Figure B.10. Transponder 211 Range and Range-Rate, Track Run E

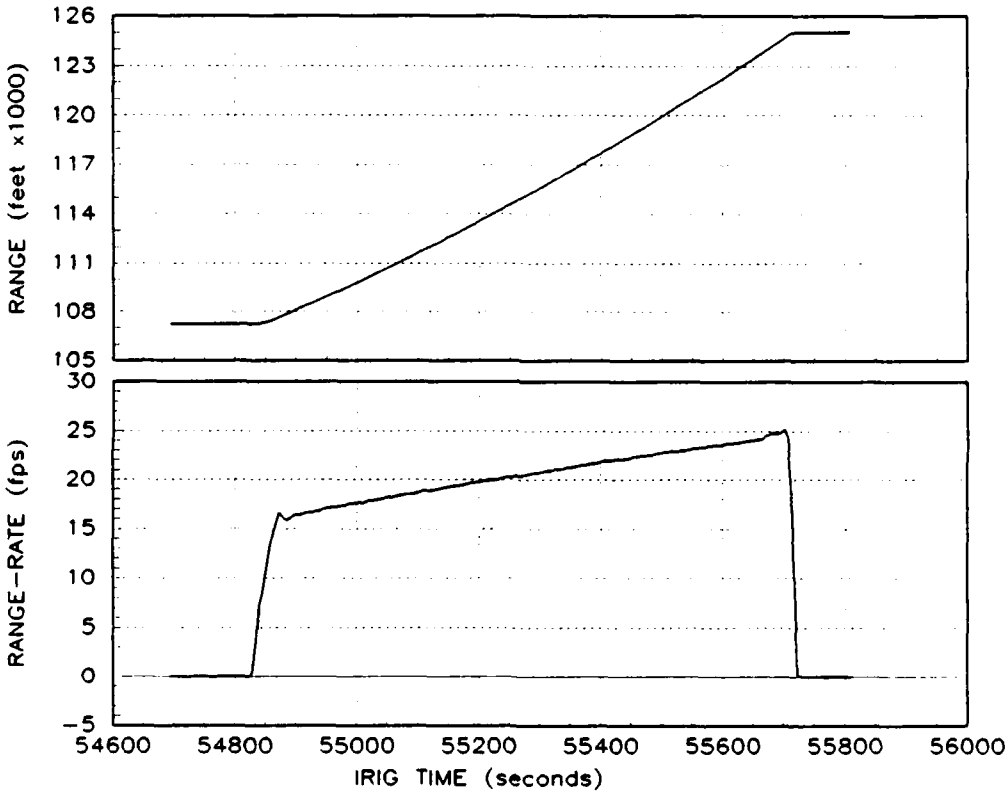

Figure B.11. Transponder 212 Range and Range–Rate, Track Run E

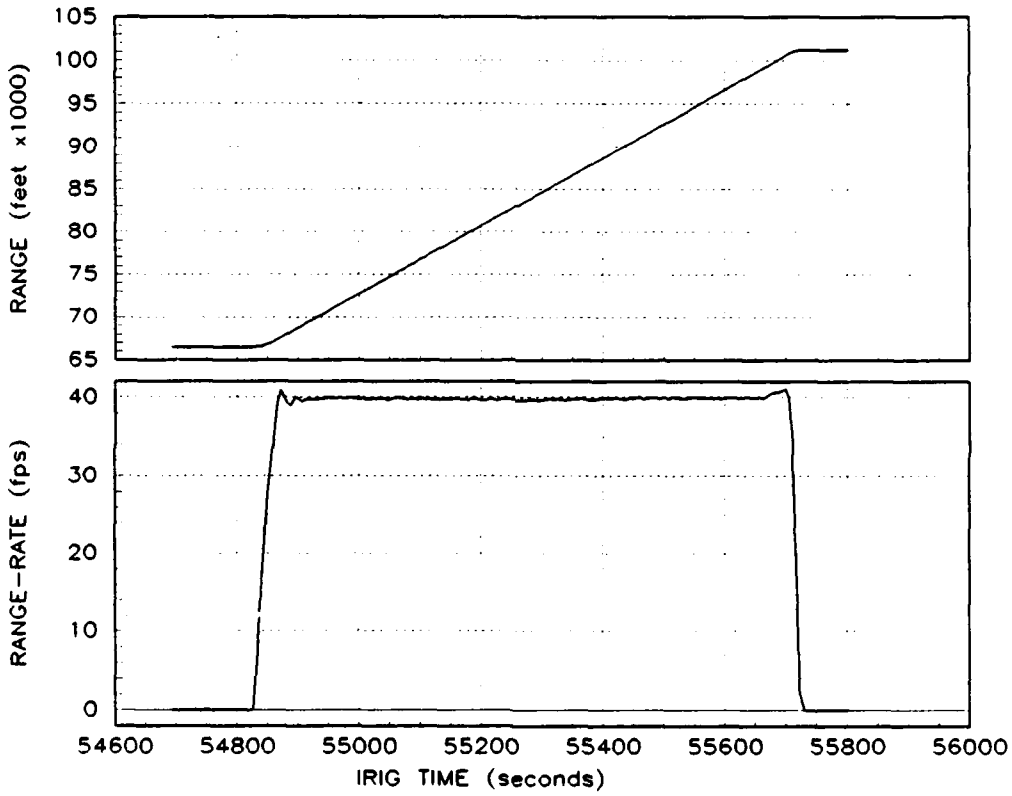

Figure B.12. Transponder 216 Range and Range–Rate, Track Run E

Appendix C. *Recorded Trajectory Data, Yuma Flight*

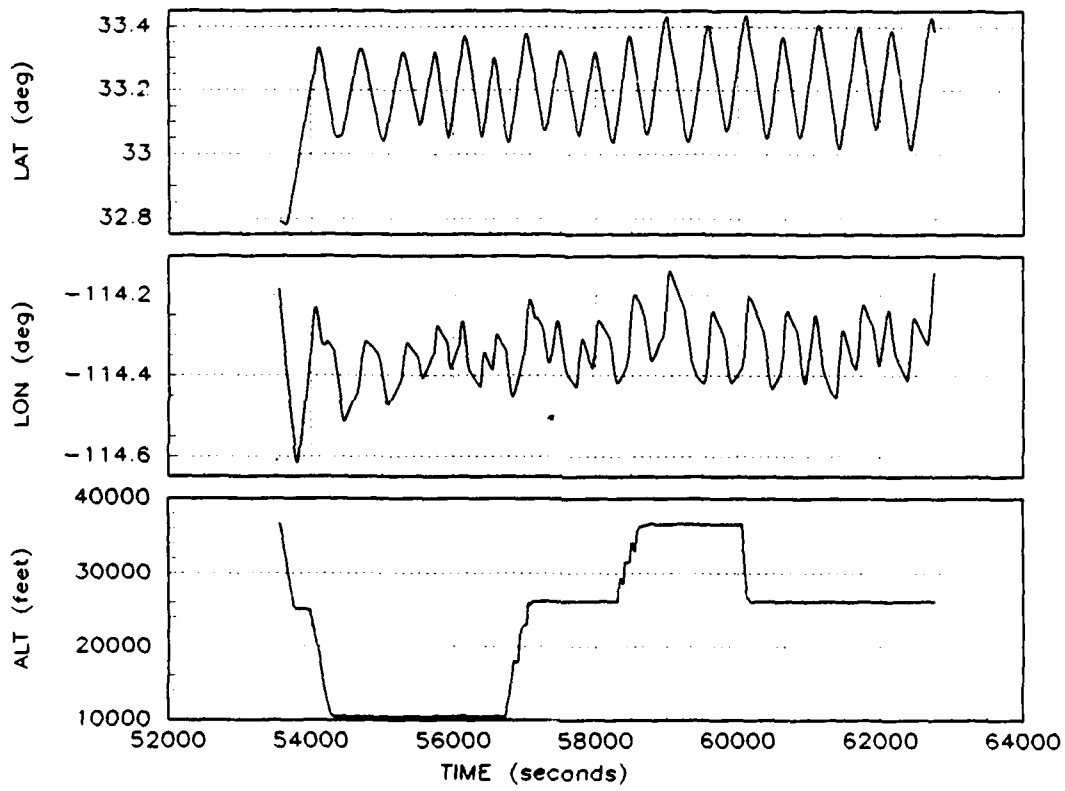

Figure C.1. Laser Ranging System Indicated Position, Yuma Flight

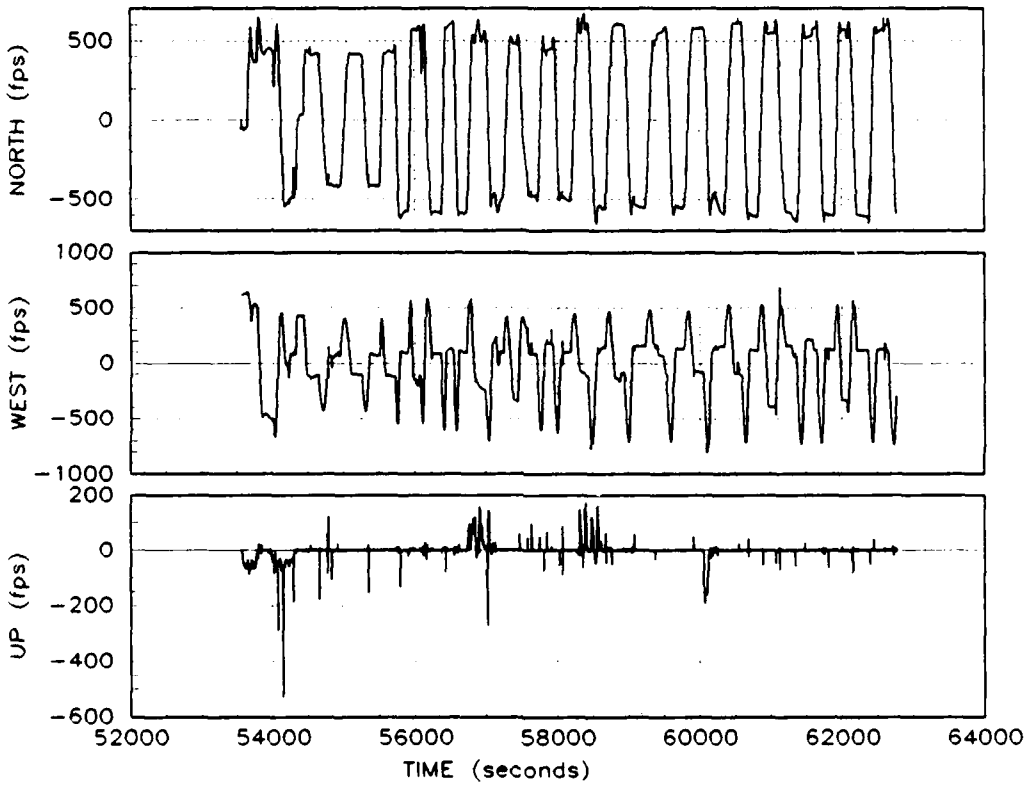

Figure C.2. Laser Ranging System Indicated Velocity, Yuma Flight

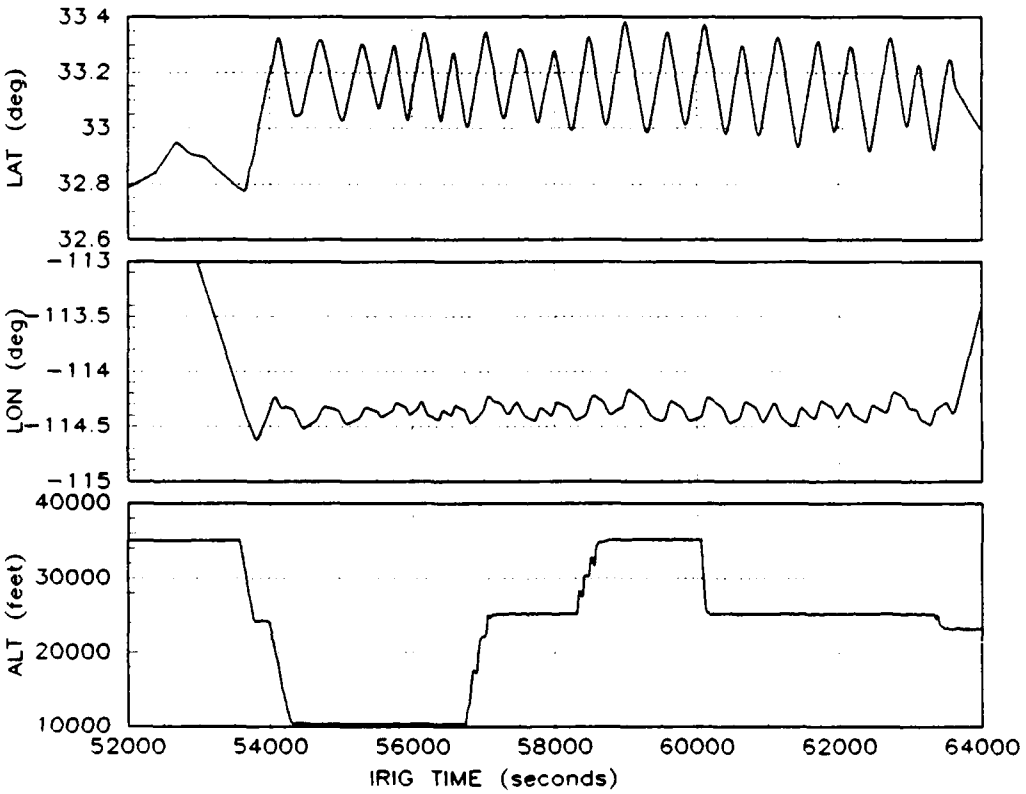

Figure C.3. LN-39 INS Indicated Position, Yuma Flight

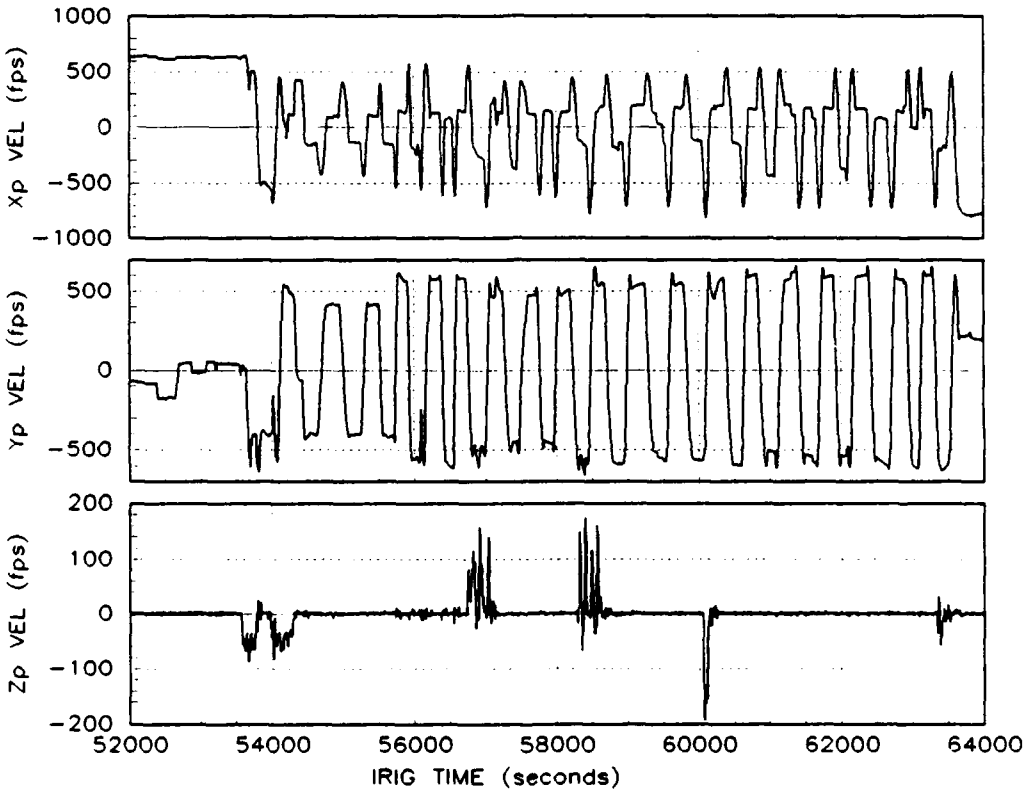

Figure C.4. LN-39 INS Indicated Velocity, Yuma Flight

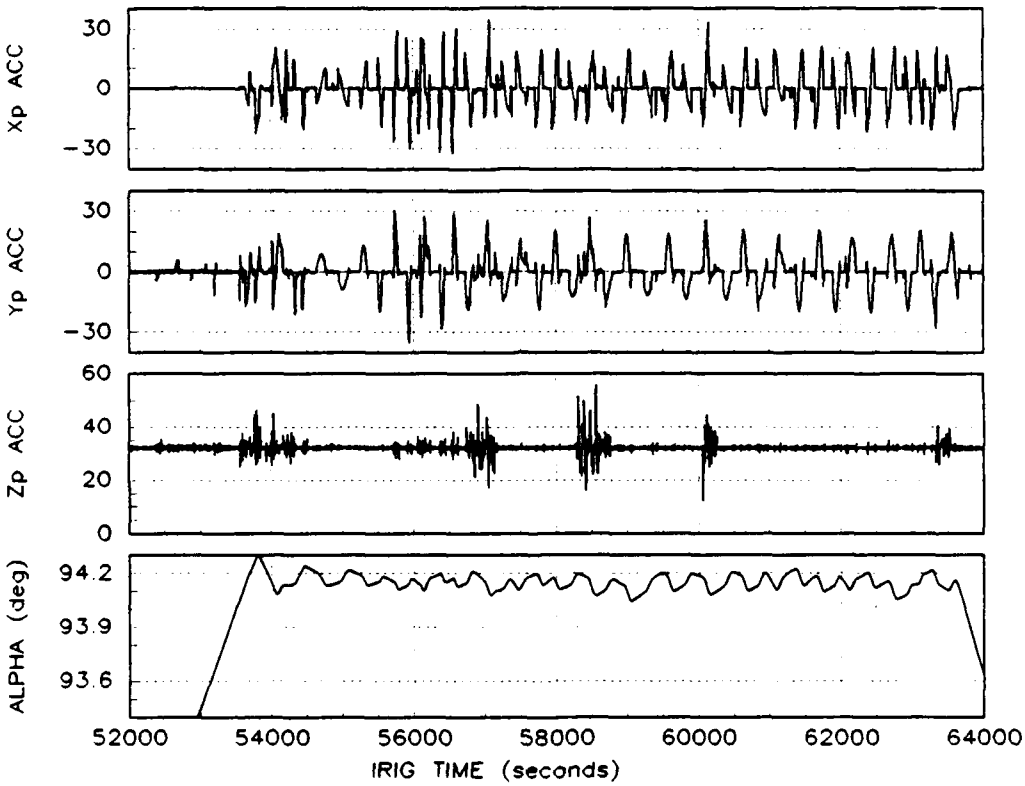

Figure C.5. INS Indicated Acceleration and Wander Angle, Yuma Flight

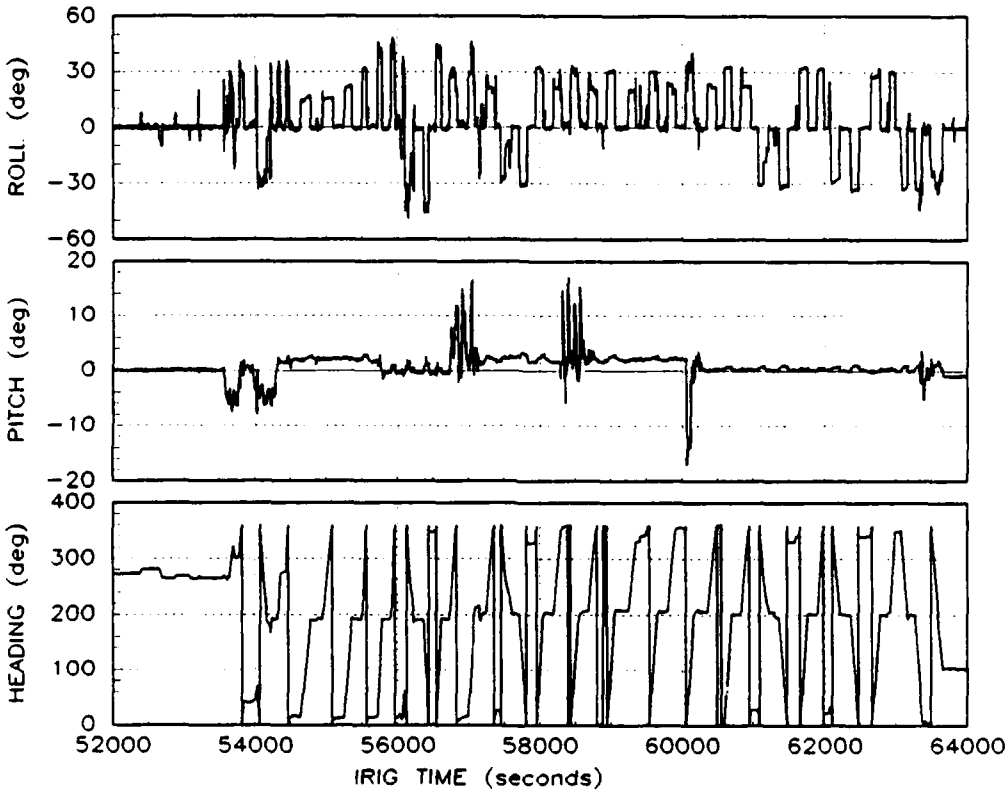

Figure C.6. LN-39 INS Indicated Aircraft Attitude, Yuma Flight

Bibliography

1. Carlson, Neal A. and Stanton H. Musick. *User's Manual for a Multimode Simulation for Optimal Filter Evaluation (MSOFE)*, Draft Copy, July 1989. AFWAL TR-88-1138, Avionics Lab, AFWAL/AAAN-2, Wright-Patterson AFB, OH.
2. Cubic Corporation. *Range/Range-Rate Subsystem (RRS) for the Completely Integrated Reference System (CIRIS)*, AFSWC TR-7321, Cubic Corporation, 9233 Balboa Avenue, San Diego, CA, August 1973.
3. Defense Mapping Agency. *Department of Defense World Geodetic System 1984*. Defense Mapping Agency Technical Report, No. DMA TR 8350.2. Washington, D.C., 30 September 1987.
4. Guidance Test Division "The Completely Instrumented Reference Instrumentation System (CIRIS)," Unpublished Contractor Informational Pamphlet, CIGTF, 6585th Test Group, Holloman AFB, NM.
5. Golub, Gene H. and Charles F. Van Loan. *MATRIX COMPUTATIONS*, Baltimore: The John Hopkins University Press, 1983.
6. Integrated Systems Inc. *$MATRIX_X$ User's Guide*, Version 6.0, and Release Notes, Version 7.0; Palo Alto, CA: 1986, 1988
7. Lewantowicz, Lt Col Zdzislaw H., Deputy Department Head, Department of Electrical Engineering, Personal Interviews, Air Force Institute of Technology, Wright-Patterson AFB, OH, June 1989 through February 1990.
8. Maybeck, Peter S. *Stochastic Models, Estimation, and Control*, Volume I, New York: Academic Press, 1979.
9. Maybeck, Peter S. *Stochastic Models, Estimation, and Control*, Volume II, New York: Academic Press, 1982.
10. Meditch, J.S., *Stochastic Optimal Linear Estimation and Control.* New York: McGraw-Hill, 1969.
11. Simkin, Gordon. CIRIS Engineer, Telephone Conversations, Guidance Test Division, 6585th Test Group, Holloman AFB, NM, Commercial: 505-679-2993, July 1989 through January 1990.
12. Solomon, Joseph K. "CIRIS Special Study," Final Report, EENG 699, Air Force Institute of Technology, Wright-Patterson AFB, OH, March 1989.
13. Solomon, Joseph K. *Development of the Extended Kalman Filter for the Advanced Completely Integrated Reference Instrumentation System (CIRIS).* MS thesis, AFIT/GE/89 M-8. School of Engineering, Air Force Institute of Technology (AU), Wright-Patterson AFB OH, March 1989.
14. Speiser, M. "Systems Engineering Analysis Report for the F-16 Standard Inertial Navigation Unit," Litton Guidance and Control Systems, Woodland Hills, CA, Revision B, March 1985.

15. Yiu, Kai P., Richard Crawford, and Ralph Eschenbach. " A Low-Cost GPS Receiver for Land Navigation," *GLOBAL POSITIONING SYSTEM: Papers Published in NAVIGATION*, Volume II. Washington D.C.: The Institute of Navigation, 1984.

Vita

Captain Faron Britt Snodgrass [redacted] He grew up near Racine, West Virginia and attended Sherman High School. He was graduated from the West Virginia Institute of Technology in December 1981, receiving the degree of Bachelor of Science in mathematics. Following graduation, he attended the USAF Officer Training School (OTS) and received his commission in the U.S. Air Force. After OTS, he attended the University of Missouri–Columbia under the sponsorship of the AFIT Undergraduate Engineering Conversion Program. He received the degree of Bachelor of Science in Electrical Engineering in December, 1983. His next assignment was to the Peacekeeper Site Activation Task Force (SATAF) at F. E. Warren AFB, Wyoming. There he worked in the engineering division of Detachment 1, Ballistic Missile Office, from January 1984 through May 1988. His primary duties were engineering management tasks required for the operational deployment of the Peacekeeper intercontinental ballistic missile weapon system in modified Minuteman III silos. He completed the USAF Squadron Officer School in December, 1986. He entered the School of Engineering, Air Force Institute of Technology in May, 1988.

[redacted]

UNCLASSIFIED
SECURITY CLASSIFICATION OF THIS PAGE

REPORT DOCUMENTATION PAGE

Form Approved
OMB No. 0704-0188

1a. REPORT SECURITY CLASSIFICATION	1b. RESTRICTIVE MARKINGS
2a. SECURITY CLASSIFICATION AUTHORITY	3. DISTRIBUTION/AVAILABILITY OF REPORT
2b. DECLASSIFICATION/DOWNGRADING SCHEDULE	Approved for Public Release; Distribution Unlimited
4. PERFORMING ORGANIZATION REPORT NUMBER(S) AFIT/GE/ENG/90M-5	5. MONITORING ORGANIZATION REPORT NUMBER(S)
6a. NAME OF PERFORMING ORGANIZATION: School of Engineering; 6b. OFFICE SYMBOL (If applicable): AFIT/ENG	7a. NAME OF MONITORING ORGANIZATION
6c. ADDRESS (City, State, and ZIP Code): Air Force Institute of Technology, Wright-Patterson AFB, OH 45433-6583	7b. ADDRESS (City, State, and ZIP Code)
8a. NAME OF FUNDING/SPONSORING ORGANIZATION: 6585th Test Group; 8b. OFFICE SYMBOL (If applicable): GD	9. PROCUREMENT INSTRUMENT IDENTIFICATION NUMBER
8c. ADDRESS (City, State, and ZIP Code): Holloman AFB, NM 88230-5000	10. SOURCE OF FUNDING NUMBERS: PROGRAM ELEMENT NO. / PROJECT NO. / TASK NO. / WORK UNIT ACCESSION NO.

11. TITLE (Include Security Classification): See Block 19

12. PERSONAL AUTHOR(S): Faron Britt Snodgrass, Capt, USAF

13a. TYPE OF REPORT	13b. TIME COVERED	14. DATE OF REPORT (Year, Month, Day)	15. PAGE COUNT
MS Thesis	FROM ____ TO ____	1990, March	174

16. SUPPLEMENTARY NOTATION

17. COSATI CODES			18. SUBJECT TERMS (Continue on reverse if necessary and identify by block number)
FIELD	GROUP	SUB-GROUP	INERTIAL NAVIGATION SYSTEM, KALMAN FILTER, CIRIS, MSOFE
17	07	03	

19. ABSTRACT (Continue on reverse if necessary and identify by block number)

Title: Continued Development and Analysis of a New Extended Kalman Filter for the Completely Integrated Reference Instrumentation System (CIRIS)

Thesis Chairman: Lt Col Z. H. Lewantowicz

(Abstract on Back)

20. DISTRIBUTION/AVAILABILITY OF ABSTRACT: ☐ UNCLASSIFIED/UNLIMITED ☐ SAME AS RPT ☐ DTIC USERS	21. ABSTRACT SECURITY CLASSIFICATION: UNCLASSIFIED
22a. NAME OF RESPONSIBLE INDIVIDUAL: Lt Col Z. H. Lewantowicz	22b. TELEPHONE (Include Area Code): 513-255-2024; 22c. OFFICE SYMBOL: AFIT/ENG

DD Form 1473, JUN 86 — Previous editions are obsolete. SECURITY CLASSIFICATION OF THIS PAGE

UNCLASSIFIED

BLOCK 19 (Continued):

Abstract

The Completely Integrated Reference Instrumentation System (CIRIS) is operated by the Central Inertial Guidance Test Facility (CIGTF), at Holloman AFB, New Mexico. CIRIS functions as a reference navigation system used for evaluating the accuracy of other types of navigations systems. As a reference standard, the root–mean–square errors in CIRIS estimates of aircraft trajectory variables must be maintained an order of magnitude smaller than the corresponding errors of the navigation system under test. The primary hardware components of CIRIS are a reference inertial navigation system (INS), a baro–altimeter, an array of ground–based transponders, a transponder interrogator, and data recording equipment. The transponder equipment provides transponder–to–aircraft range and range–rate measurements during test flights. The primary software component of CIRIS is a Kalman filter program which processes the recorded measurements and estimates the true position and velocity of the aircraft throughout the test flight.

The estimation accuracy of CIRIS must be increased so that CIRIS can serve as a benchmark for measuring the accuracy of Global Positioning System (GPS) aided inertial navigation systems. This thesis documents the continuation of research to develop completely new Kalman filter software for CIRIS. A 70–state filter, based on the Multimode Simulation for Optimal Filter Evaluation (MSOFE) program, developed in previous research is the starting point. This 70–state filter models error dynamics associated with the CIRIS Litton LN–39 INS, baro–altimeter, and transponder equipment. In this thesis, the model for atmospheric effects on transponder range measurements is refined and the filter is modified to process barometric altitude measurements in addition to the transponder measurements. The performance of the resulting filter is evaluated using real CIRIS data recorded during a slow speed ground test and an aircraft flight test. The filter position and velocity estimates are compared to independent measurements of the same quantities. The structure for a companion fixed–interval smoother program is proposed and discussed, but not implemented. Future research is expected to extend the filter to process differential mode GPS measurements.